Università degli Studi del Piemonte Orientale

“Amedeo Avogadro”

Dipartimento di Scienze del Farmaco

Dottorato di Ricerca in Biotecnologie Farmaceutiche ed Alimentari

XXVI ciclo a.a. 2010-2013

BIFUNCTIONAL CHELATING AGENTS: CHEMOENZYMATIC APPROACH AND APPLICATION TO DCE-MRI

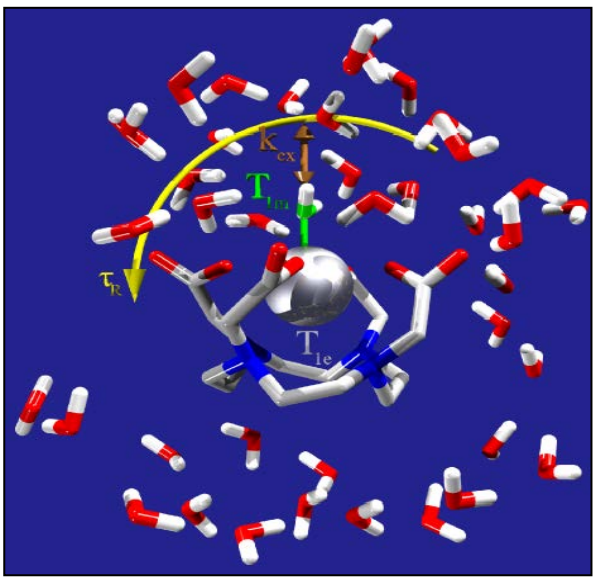

Paolo Minazzi

Università degli Studi del Piemonte Orientale

“Amedeo Avogadro”

Dipartimento di Scienze del Farmaco

Dottorato di Ricerca in Biotecnologie Farmaceutiche ed Alimentari

XXVI ciclo a.a. 2010-2013

BIFUNCTIONAL CHELATING AGENTS: CHEMOENZYMATIC APPROACH AND APPLICATION TO DCE-MRI

Paolo Minazzi

Supervised by Prof. Giovanni B. Giovenzana

PhD program co-ordinator Prof. Menico Rizzi

Contents

1.1.1 Introduction

Magnetic Resonance Imaging is one of the most used imaging techniques in structural anatomic clinical diagnostics.

In 1946, Bloch and Purcell (Nobel Prizes 1952) independently discovered that the nuclei of different atoms absorbed electromagnetic radiation in the radiowaves frequency range; this phenomenon was named nuclear magnetic resonance (NMR). In 1970 Raymond Damadian discovered that the distribution of water in the human body is the key to obtain information about living organism, indeed he showed that NMR signals of tumours differed from those of normal tissues. In 1972 Lauterbur and Mansfield (Nobel Prizes in 2003) showed that NMR signals could be used to create two-dimensional maps of the density of nuclear spins in a medium, paving the way for imaging applications, immediately employed for anatomic and diagnostic purposes. This idea was further developed by Ernst (Nobel Prize in 1991): in 1975 he proposed to encode spatial information through the use of magnetic field gradients and decode them using the Fourier transform of the recorded signal. In the same year Mansfield produced the first human NMR image.

The current state of the art technology uses field gradients to create sub-millimeter-thick slices, allowing the detailed acquisition of high resolution 2D and 3D images. With the fundamental technology based on NMR, MRI uses radiofrequencies as the source of excitation and magnetic fields; both of them have been shown to have no detrimental effects on patients. As a noninvasive imaging tool MRI has the potential to be less harmful compared to other imaging modalities employed to acquire diagnostic images, such as computer tomography (CT), using X-rays as well as positron emission tomography (PET) and single-photon emission computed tomography (SPECT) relying on radioactive sources. Hence, MRI analysis can be reiterated on the same patient, with insignificant side effects in contrast to other imaging modalities whose reiteration is restricted by radiation-dose safety limitations.

1.1.2 Basic Principles of NMR[1,2,3.]

Atomic nuclei are positively charged masses composed of protons and neutrons. They are characterized by a magnetic angular momentum, or spin. As electric charges in motion are associated with a magnetic field, the rotating atomic nucleus can be treated as a magnetic dipole. When these nuclei are placed in a magnetic field of high intensity (B_0), they align along the direction of the lines of force of the field, *i.e.*: parallel (*up* - lower energy level) or antiparallel (*down* - higher energy level). There is a constant dynamic difference between the number of nuclei oriented up and down, which depends on the intensity of B_0. The distribution of nuclei on the different energy levels is described by the Boltzmann equation:

$$\frac{N_1}{N_u} = \exp^{\Delta E / \kappa_B T}$$

Equation 1

Nu number of nuclei at higher energy level; N_1 number of nuclei at lower energy level; ΔE energy difference between the two levels; K_B Bolzmann constant; T absolute temperature.

In equilibrium conditions the lower energy level is slightly more populated and the sum of the overall magnetic moments give rise to a single resultant magnetic moment, the macroscopic magnetization (M_0).

The nuclei do not actually align directly with the direction of the magnetic field, but rather rotate around the axis of the magnetic field with a precession motion. The precession rate is indicated as Larmor frequency and represents the electromagnetic radiation frequency allowing the nucleus to absorb energy. The absorption of energy will cause the proton to alter its alignment. The precession

frequency is linearly dependent on the magnetic field intensity as described by the following equation:

$$W_0 = \gamma \times B_0$$

Equation 2

W_0 is the precession frequency, γ is the gyromagnetic ratio of the nucleus and B_0 is the strength of the magnetic field.

The gyromagnetic ratio defines the ratio between the magnetic moment and the intrinsic spin angular momentum, characteristic of each nuclear species. This means that, for a given magnetic field intensity, different nuclei can be distinguished on the basis of their different resonance frequencies. If hydrogen atoms are then placed into a magnetic field (B_0) the angular momentum splits in two possible orientations, either aligned with (+ ½) or against the magnetic field (- ½). This can be calculated from Equation 3:

$$m = (2I+1)$$

Equation 3

Where *m* is the magnetic quantum number, I = ½ for ^{1}H nuclei. Additional nuclei used in MRI diagnostic applications include ^{13}C, ^{19}F and ^{23}Na, all of them having I = ½.

The distribution of the two energy states (±½) is defined by a Boltzmann distribution, with a larger population being aligned with the magnetic field, or in a lower energy state. The difference in energy state population is defined as a vector with the macroscopic magnetization defined as M_0 along the (vertical) *z* axis, conventionally chosen as the magnetic field direction. Irradiation at the Larmor frequency using a radiofrequency (RF) pulse will reduce the numerical difference

between the two populations of spin and causes the decrease of the resulting macroscopic magnetization along the *z* axis. M_0 experience a deflection from the *z* axis towards the *x* or *y* axis of an angle ("pulse angle"), where the receiver is located to measure the energy released during the following relaxation process and recorded in terms of signal intensity as a function of time (FID, free induction decay).

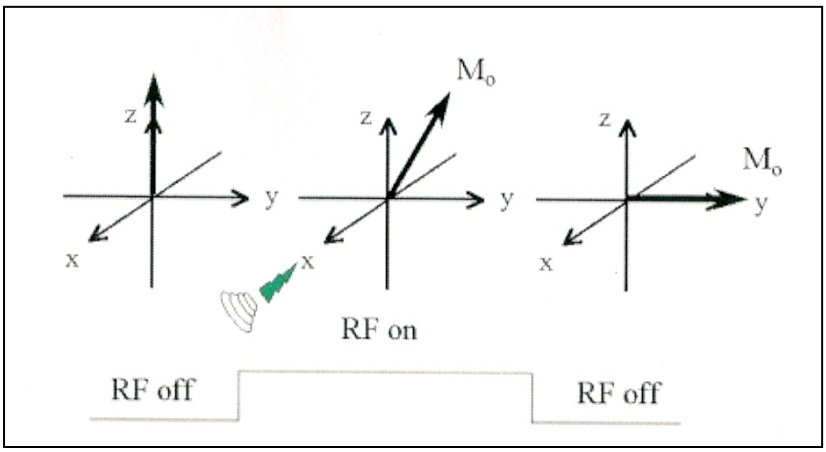

Figure 1: Effect of a 90° pulse on M_0

The mathematical analysis of the FID by Fourier transform allows to pass from the time domain to the frequency domain, obtaining the NMR spectrum as it is normally known (signal intensity as a function of frequency).

Relaxation occurs after the RF pulse is turned off. At this point the net magnetization has been flipped onto the *x* or *y* axis now starts to relax back to the resting state. Relaxation occurs through two mechanisms:

- Relaxation leading to recovery of the longitudinal magnetization
- Relaxation leading to the decay of transverse magnetization

T_1 or longitudinal relaxation time, is the time required for the macroscopic magnetization along the *z* axis to reach 63% of its equilibrium value, immediately after the cessation of the pulse. This occurs through the interaction of the excited ^1H nucleus with its surroundings to release energy. T_1 changes with the intensity of B_0.

The second mechanism is spin-spin relaxation or transverse relaxation. After the RF pulse has aligned the M_0 vector onto the *x* or *y*-axis the signals are bunched together in a coherent ensemble (phase coherence). The protons start to process and interact with other protons, leading to an overall phase decoherence that reduces the transverse magnetization. The parameter T_2 is a measurement of how quickly the in-phase signals become out-of-phase. T_2 is independent by B_0.

1.1.3 Magnetic Resonance Imaging (MRI)[1,2,3.]

MRI is a diagnostic scanning technique based on principles of NMR. It measures the signal from the hydrogen nuclei of water, which is modified by the chemical environment. NMR spectroscopy measures the characteristics of any hydrogen nuclei depending on their position in the molecule. Instead of obtaining information about chemical shifts and coupling constants, MRI gives spatial distribution of the intensity of the water proton signal in the volume of the body. This signal intensity depends essentially on three factors: the density of proton spins in a given volume, the longitudinal and transverse relaxation times T_1 and T_2 of these spins. Using different RF pulse sequences, image intensity can be weighted with respect to T_1 or T_2.

The data to create an MR image is obtained in a series of steps. First, the tissue magnetization is excited using an RF pulse in the presence of a slice select gradient. The other two essential elements of the sequence are phase encoding and frequency encoding/read out, which are required to spatially localize the protons in the other two dimensions. Finally, after the data has been collected, the process is repeated for a series of phase encoding steps.

The gradient echo sequence is the simplest type of MRI sequence. It consists of a series of excitation pulses, each separated by a repetition time TR. Data is

acquired at some characteristic time after the application of the excitation pulses and this is defined as the echo time TE.

The spin echo sequence is made up of a series of events : 90° pulse – 180° rephasing pulse. Following a 90° RF pulse, the magnetization vector lies in the transverse plane. Due to dephasing phenomena, some spins slow down and others speed up. A 180° pulse is then applied to 'flip' the spin vectors so that the previously slower vectors are effectively precessing ahead of the previously faster ones. After a further time delay (equal to TE/2), a spin echo is formed.

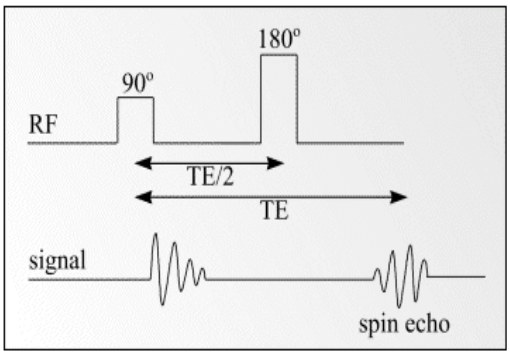

Figure 2: The spin-echo pulse sequence

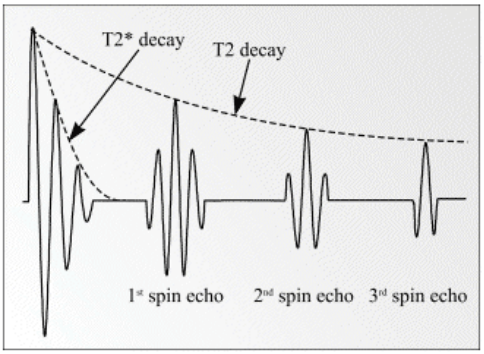

Figure 3: Signal decay in a spin-echo sequence

If a further 180 degree pulse is applied at time TE/2 after the peak signal of the first spin echo, then a second spin echo signal will form at time TE after the first spin echo. The peak signal amplitude of each spin echo is reduced from its previous

peak amplitude due to T_2 dephasing which cannot be rephased by the 180 degree pulses.

The signal intensity SI depends not only from T_2, but also from the spin-lattice relaxation time T_1 and the proton density ρ. In clinical diagnosis is very important to obtain images which one of these contributes is prevalent, and this can be done acting on TR and TE. According to Equations 4:

$$SI = \kappa \cdot \rho \cdot \left[1 - \exp\left(- \frac{TR - TE}{T_1} \right) \cdot \exp\left(- \frac{TE}{T_2} \right) \right]$$

Equation 4

With a low ratio (TR-TE) in the equation, the image is weighted on the T_1, while TE and TR long increase the weight of T_2. The combination of TR long and TE short emphasizes the importance of ρ (Image proton-density).

In the scale of the contrast, by convention, the areas that generate a stronger is assigned to a light color, while lower intensity corresponds to a darker color. Accordingly areas of the sample with longer T_1 are darker, while a transverse relaxation time longer leads to a lighter color.

The spatial position of the nucleus is fundamental to generate an image of a patient. A magnetic field gradient is a variation in the magnetic field with respect to position. Therefore, the Larmor frequency of the protons will be different and will then determine a difference in chemical shift of the signals in the NMR spectrum.

This difference in chemical shift depends on their physical separation and the strength of the field gradient, thus provides information on the spatial arrangement in the sample. If a single gradient is applied along the x axis are not obtained enough information to deduce the position in space of the nuclei, but if we rotate the gradient in three directions (x, y, z) we can locate in the three dimensions of space.

$$B_{tot} = B_0 + G(x,y,z) \quad \textit{Equation 5}$$

Accordingly, a large number of spectra of the sample are registered, by varying the direction of the gradients, thus obtaining various projections of the object under examination. The projections obtained, are encoded in images through a technique known as “zeugmatography”.

The tomographic imaging, producing NMR images of a slice of the human body. The slice is composed of several three-dimensional elements, *volume element or voxels*. While MR image are composed by bidimensional elements called *picture elements or pixels*. The intensity of the NMR signal of the corresponding voxel is displayed in pixels using a gray scale. The different shades of gray of a pixel can be expressed with a number and the numerical difference between two different signals defines quantitatively the contrast. The contrast between two pixels is determinate by the follow equation:

$$C = \frac{I_a - I_b}{I_a + I_b}$$

Equation 6

Where I_a and I_b are the intensity of two adjacent pixels.

The contrast is the ability to discriminate two adjacent structures with different structural characteristics. Many pathological events determine an appreciable variation of these parameters, among which the longitudinal (T_1) and transverse (T_2) relaxation times of the water protons, thus allowing to recognize affected areas. Nevertheless, the difference arising from these variations may be too small and leading to a negligible contrast. To this purpose, the addition of a suitable “contrast agents” to the system analyzed is often useful to obtain an appreciable contrast.

However sometimes insufficient contrast is observed, and, thus the use of contrast agents (CAs) is of great assistance in many applications. Unlike the

contrast agent used in other clinical imaging studies as PET or SPECT, these are not themselves directly imaged but rather enhance contrast indirectly by affecting the nuclear magnetic relaxation times of the water protons in surrounding tissues. Contrast agents are currently used in diagnostics to enhance the image contrast and roughly 30% of all MR images employ some form of CA administered intravenously to the patient.

1.1.4 Contrast Agents (CAs)[3,4]

CAs can be classified in different ways, according to their various features, such as:

1. effect on images
2. magnetic properties
3. biodistribution.

1. Magnetic resonance CAs work by reducing the T_1 and T_2 relaxation times of nuclei in the target tissue, and are thus described as either T_1 agents or T_2 agents depending on whether the relative reduction in relaxation times caused by the CA is greater for T_1 or T_2. According to the effect on T_1 agents or T_2 CAs can be divided on:
    - Positive (predominant effect of T_1 shortening)
    - Negative (predominant effect of T_2 shortening)

    Positive CAs have a similar effect on the T_1 and T_2 but, since the T_1 of the tissue has a higher value of T_2, at low doses the predominant effect is the decrease of the T_1. Globally, CAs positive results in a better signal / noise ratio and a higher intensity of the signal.

Negative CAs act preferentially by shortening T_2 and T_2* (effective transverse relaxation time). T_2-Weighted images give negative contrast, due to the predominant effect of T_2 shortening.

The classification of MR CAs as either T_1 agents or T_2 agents is not always accurate, since any CA that reduces T_1 also reduces T_2. However, any agent that reduces T_2 does not necessarily reduce T_1, at least at MRI field strengths. Whether the CA functions as a 'T_1 agent' or 'T_2 agent' depends on the imaging sequence used, the magnetic field strength, the size of the CA, and how the CA is compartimentalized in the tissue.

2. CAs can also be classified according to their magnetic properties as paramagnetic or superparamagnetic agents.
   - Metal ions with one or more unpaired electrons are paramagnetic, and therefore possess a permanent magnetic moment. Molecular motions cause random fluctuations in this dipolar magnetic interaction, reducing both the longitudinal T_1 and the transverse T_2 relaxation times of the water protons. However T_2 in some tissues are relatively short, this effect can be almost irrelevant. Gadolinium (Gd(III)) and manganese (Mn(II)) are examples of paramagnetic ions which are used as MR CAs, because their physical properties are suitable for efficiently reducing the T_1 and T_2 proton relaxation times.
   - Supermagnetic agents consist of materials, such as iron oxides, in the form of colloids made up of nanoparticles (5-10 nm in diameter) in suspension, which are composed of very small crystallites containing several thousand magnetic ions. The superparamagnetic materials behaves similarly to paramagnetism, except that, instead of each individual atom being independently influenced by an external magnetic field, that the magnetic moment of the entire crystallite tends to align with that magnetic field. Thus, the magnetic moments of the individual

ions do not cancel out but are mutually aligned, and the crystallites have a permanent magnetic moment, which is very large in the presence of a magnetic field, much larger than that of a single paramagnetic ion. Superparamagnetic agents were initially developed as T_2-agents, producing a dark area on MRI images resulting from their negative contrast effect. However, a new generation of these agents has also been reported to have excellent T_1-enhancing properties.

3. According to their biodistribution CAs can be divided as nonspecific agents and specific or target agents.
    - Non specific agents are those that do not interact with any type of cells. Those agents can be extracellular fluid (ECF) agents, low molecular weight extracellular complexes that equilibrate rapidly between intravascular and interstitial space and then are mainly excreted by the kidneys. After being intravenously injected, these agents leak rapidly from the blood pool into the interstitium with a distribution half-life of about 5 minutes and are cleared mainly by the kidneys with an elimination time of about 80 minutes. ECF agents are extensively used in body imaging applications. They provide increased enhacement and visualization of lesions, such tumors. They also shown great utility in MR angiography and are used for detection of many brain pathologies. High molecular weight blood pool agents (BPA), such as high generation dendrimers, which reside within the intravascular space and are slowly excreted via the kidneys and/or the liver, can be considered as non specific agents. BPA or intravascular agents are significantly larger in size than ECF and have higher r_1 relaxivities. Their high molecular weight (>20 kDa) prevents leakage into the interstitium and they remain in the intravascular system for a prolonged time compared with conventional ECF agents. The concentration of the CA in the plasma

remains stable over one hour, as its mainly renal elimination requires the previous degradation of the macromolecule. This extends the imaging window from about 1 minute to about 1 hour. The blood pool CAs can be divided into several classes, according to their mechanism of action: 1) the noncovalent binding of low molecular weight $Gd(III)^{-}$ based complexes to human serum albumin (HAS), which is the most abundant plasma protein, prevents immediate leakage into the interstitial space; 2) systems based on polymers or liposomes, based on an increase in the size of CA molecule, which slows down leakage through endothelial pores; and 3) systems based on particles involving a change in the route of elimination.

- The specific or target agents can be considered in two groups: those that are passively directed to a particular type of cell, and those are actively target to a molecularly specific site target with an appropriate ligand. The first group includes organ-specific agents for liver (hepatobiliary), spleen, lymph nodes, bone marrow or brain, mainly on the basis of agent size and chemical structure. The second group includes agents witch target pathological processes or state, such as inflammation, atherosclerosis, angiogenesis, apoptosis and tumors. They are cell labeling CAs, as they work through recognition of specific molecular markers of those processes at the cell surface, such as cell-specific receptor or transport proteins, accumulate at those molecular sites, usually in the intracellular space and can be used in molecular imaging application of MRI.

1.1.5 Complexes of paramagnetic ions [3,5,6,7,8].

First of all, it is important introducing some fundamental parameters to better understand how a paramagnetic ion behaves as a contrast agent.

The efficacy of the CA measured as the ability of its 1 mM solution to increase the relaxation rate of water protons is called relaxivity and indicate as $r_{1,2}$.

Paramagnetic CA's increase the signal intensity of the tissue containing them by increasing the longitudinal and/or transverse relaxation rates ($1/T_1$ or $1/T_2$) using their unpaired electrons to facilitate spin transfer. The diamagnetic ($1/T_{1,2d}$) and paramagnetic ($1/T_{1,2p}$) contributions to the relaxation rates of such solutions are additive:

$$1/T_{1,2obs.} = 1/T_{1,2d} + 1/T_{1,2p}$$

Equation 7

Where $(1/T_{1,2})_{obs}$ is the observed solvent relaxation rate and the subscripts "*d*" and "*p*" refer to diamagnetic and paramagnetic, respectively.

The paramagnetic contribution to the relaxation rate is linearly proportional to the concentration of the paramagnetic species:

$$1/T_{1,2obs.} = 1/T_{1,2d} + r_{1,2}\,[M]$$

Equation 8

Where M = paramagnetic substance, $r_{1,2}$ = proton relaxivity ($s^{-1}mM^{-1}$). Relaxivity ($r_{1,2}$) is then defined as the concentration-dependent increase in relaxation rate of the paramagnetic agent, or the slope of a plot of $(1/T_{1,2})_{obs}$ versus concentration.

The overall relaxivity can be correlated with a set of physico-chemical parameters, which characterize the complex structure and dynamics in solution, they are:

- the number of inner-sphere water molecules directly coordinated to the paramagnetic centre *q*,
- the residence time of the coordinated water molecule τ_M,
- the rotational correlation time representing the molecular tumbling time of a complex τ_R,
- the distance between the metal ion and the proton *r*,
- electronic relaxation time T_{1e}

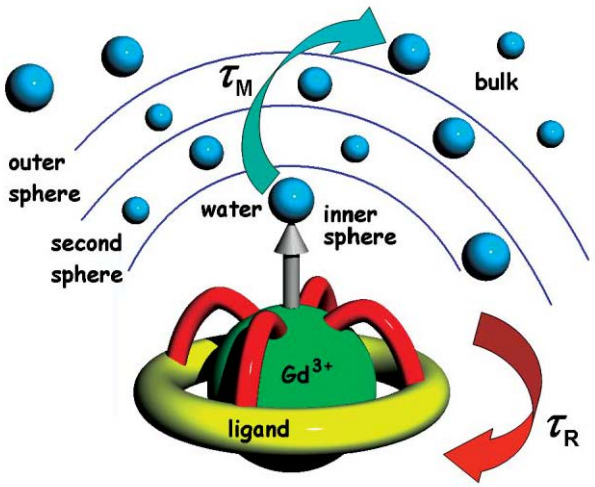

Figure 4

Model of Gd(III)-based contrast agent in solution.

The relaxivity enhancement of water protons in aqueous solutions of paramagnetic complexes arises from time fluctuation of the dipolar coupling between the electron magnetic moment of the metal ion and the nuclear magnetic moment of the solvent nuclei. This magnetic field around the paramagnetic center vanishes rapidly with distance. Therefore, specific chemical interactions that bring the water protons into the immediate proximity of the metal ion play an important role in transmitting the paramagnetic effect towards the bulk solvent. This interaction is expressed with a model that considers two contributions: *inner sphere* (*IS*), due to water molecules present in number *q* in the coordination sites of the

ion, and *outer sphere* (*OS*), which involves all the solvent molecules diffusing by the complex:

$$R_1^{obs} = R_{1p}^{IS} + R_{1p}^{OS} + R_1^{W}$$

Equation 9

Where R_1^{obs} is the measured relaxation rate relaxation and R_1^{W} the rate of the solvent without the paramagnetic complex.

The inner-sphere water protons then exchange with bulk solvent protons and this way the paramagnetic influence is propagated to the bulk. This mechanism is depicted as the inner-sphere contribution to the overall proton relaxivity. Solvent molecules of the bulk also experience the paramagnetic effect when they diffuse in the surroundings of the paramagnetic center. The effect of the random diffusion is defined as outher-sphere relaxation.

For certain agents, solvent molecules that are not directly bound in the first coordination sphere may also remain in the proximity of the paramagnetic metal for a relatively long time, this relaxivity contribution originating from these interactions is called second-sphere relaxivity.

Inner-sphere contribution

The inner-sphere contribution to the overall proton relaxation rate enhancement result from chemical exchange of the coordinated water protons with the bulk, the latter being much more populated. The observed signal correspond to that of the free water.

The relaxation of the bound water protons is governed by the dipole-dipole (DD) and scalar (SC), or contact, mechanism, where both are dependent on the magnetic field. The dipole-dipole part of the interaction is modulated by the

reorientation of the nuclear spin-electron spin vector, by changes in the orientation of the electron spin (electron spin relaxation) and by water (proton) exchange.

The relaxation rates of water protons related $T_{i,M}$ are generally expressed by the modified Solomon-Bløembergen equations:

$$\frac{1}{T_{1M}^{DD}} = \frac{2}{15}\frac{\gamma_I^2 g^2 \mu_B^2 S(S+1)}{r^6}\left[\frac{3\tau_{c1}}{(1+\omega_I^2\tau_{C1}^2)} + \frac{7\tau_{c2}}{(1+\omega_S^2\tau_{c2}^2)}\right]$$

Equation 10

$$\frac{1}{T_{2M}^{DD}} = \frac{1}{15}\frac{\gamma_I^2 g^2 \mu_B^2 S(S+1)}{r^6}\left[\frac{3\tau_{c1}}{(1+\omega_I^2\tau_{c1}^2)} + \frac{13\tau_{c2}}{(1+\omega_S^2\tau_{c2}^2)} + 4\tau_{c1}\right]$$

Equation 11

Where S is the the electronic quantic spin number (Gd= 7/2), γ_I is the nuclear giromagnetic ratio, g is the electron g-factor, μ_B is the Bohr magneton, ω_S and ω_I are the nuclear and electron Larmor frequencies, r is the distance between the electronic spin and nuclear spin, $\tau_{c,I}$ correlation time.

The scalar interaction remains unaffected by reorientation of the molecule and is only modulated by electron spin relaxation and water exchange. The contact interaction is described, as dipolar interaction, by a Solomon-Bløembergen equations:

Equation 12
$$\frac{1}{T_{1m}^{SC}} = \frac{2}{3}S(S+1)\left(\frac{A}{h}\right)^2\left(\frac{\tau_{e2}}{1+\omega_S^2\tau_{e2}^2}\right)$$

Equation 13
$$\frac{1}{T_{2M}^{SC}} = \frac{1}{3}S(S+1)\left(\frac{A}{h}\right)^2\left(\frac{\tau_{e2}}{1+\omega_S^2\tau_{e2}^2} + \tau_{e1}\right)$$

Where A / h is the hyperfine or scalar coupling constant between the electron of the paramagnetic center and the proton of the coordinated water, and τ_{ei} correlation time.

Second and outher-sphere contribution

This contribution accounts for about 40% of the relaxivity of monoaquo Gd(III) complexes and arises from the modulation of the dipolar interaction by diffusion of the solvent molecules next to the paramagnetic center.

This occurs by two mechanisms: second-sphere relaxation and outer-sphere relaxation. Second-sphere relaxation occurs when water molecules in the second coordination sphere (H-bonded to lone pairs on the carboxylate oxygen atoms), are relaxed via a dipolar mechanism. This is difficult to quantify since the number of second-sphere water molecules and the metal-H distance are unknown, and τ_m is very short and is the likely limiting parameter in determining T_{1m}.

Outer-sphere relaxation arises from the translational diffusion of water molecules close to the paramagnetic complex.

Experimental evidence for the occurrence of this solvent/metal complex interaction is difficult to obtain and, in most cases, its consideration may only represent a negligible correction to the inner- and outer-sphere relaxivities in the traditional model. However, in several cases, a careful analysis of the relaxation rate of the solvent as a function of magnetic field, pH and temperature allowed the evaluation of this contribution and the extraction of more useful and correct information from the data analysis.

Hydration number (*q*)

Inner-sphere proton relaxivity is linearly proportional to the number of water molecules directly coordinated to the paramagnetic ion.

The presence of CA influences a decrease of theoretical hydration number for the paramagnetic ion, *i.e.* Gd(III) aqua ion, there are eight inner-sphere water

molecules which would result in a proportionally high relaxation enhancement, but Gd(III) is toxic under physiological conditions and has a strong tendency to precipitate in the form of gadolinium-hydroxide. In fact, the thermodynamic and kinetic stabilities of the complex, which are guarantees of non-toxicity, can considerably decrease when more than one coordinated site is occupied by water.

The hydration number of a complex can be assessed from X-ray structure analysis; nevertheless, it also has to be determined in solution as the solid state structures do not always correspond to the species present in solution. There are several methods for determination such as NMR (Dysprosium Induced Shift, DIS) luminescence or EPR spectroscopy.

In all clinically utilized CAs, q = 1. Similarly, gadolinium(III) complexes of most octadentate DTPA and DOTA derivatives contain just one coordinated water molecule.

The distance between the metal ion and the proton (*r*)

The distance between the water proton and the unpaired electron spin, *r*, is a difficult parameter to measure and to control. According to modified Solomon-Bløembergen equations (equations 10-11) a decrease of 0.1 Å in the *r* distance corresponds to a 20% increase in inner-sphere proton relaxivity, while a decrease of 0.2 Å results in a much as 50% increase. In principle, two possibilities could be imagined to shorten the metal-H distance with the aim to increase the relaxivity.

First, higher title angles between the plane of the bound water and the metal-O bond could be induced by hydrogen bonding of the coordinated water to an appropriate side group of the chelate, which could result in a significant decrease of the metal-proton distance.

The second possibility for increasing relaxivity through changes in the metal-H distance could be the electron delocalization towards the ligand.

Nevertheless the *r* values used in relaxivity analyses of paramagnetic complexes are in most cases only estimations, because the metal-coordinated water hydrogen distance is a difficult parameter to obtain experimentally.

The residence time of the coordinated water molecule (τ_M)

The residence lifetime of protons (τ_M) plays a dual role in determining proton relaxivity. It modulates the efficiency of chemical exchange from the inner-sphere of the metal to the bulk, and also it is contributes to the overall correlation time (τ_c), that governs the dipole-dipole interaction between the electron and nuclear spin.

The exchange of coordinated water protons can occur in two ways: independently of the exchange of the entire water molecule on which it resides, or via the exchange of the water molecule itself.

Around neutral pH, the overall proton exchange rate is generally equal to the exchange rate of the entire water molecules, while, on increasing the acidity or basicity of the solution, the proton exchange may become considerably faster than the water exchange due to acid-or base-catalyzed pathways.

Generally the value of τ_M is in the order of $10^{-6} \div 10^{-9}$ s, which means conditions of rapid exchange about the time scale considered ($\tau_M << T_{1M}$), with a somewhat reduced dependence τ_M (*i.e.* it is not generally a limiting factor in the relaxation process).

The value of τ_M is very important in case of paramagnetic complexes bounded with a macromolecules, in fact this linking increase the lifetime of the coordinated water, until to obtain $\tau_M \cong T_{1M}$, and then the exchange with the bulk water is slow and bringing an decrease of the relaxivity value.

The rate of water exchange between an inner-sphere water molecule and the bulk can usually be estimated by ^{17}O NMR by measuring the transverse relaxation rate of water in the presence and absence of a paramagnetic chelate.

It was also studied the mechanism by which water exchange occurs. There are two types of mechanisms: *dissociative*, it breaks the bond between the water molecule coordinated metal and later forms the bond with the new water molecule; *associative*, it forms a new bond between the complex and the water molecule so as to have a transition state that contains both the outgoing molecule that the incoming one.

Rotational correlation time (τ_R)

A parameter which allows a considerable increase in relaxivity for the paramagnetic complexes, is the rotational correlation time; in fact the relaxivity value increases with the increase of the rotational correlation time.

The rotational correlation time describes the molecular mobility, in particular the rotational mobility of the paramagnetic complex.

Values of short τ_R are associated with small molecules and with a round shape; on the contrary a long τ_R is characteristic of molecules with an high molecular weight and with irregular shapes.

In order to obtain an increase of rotational correlation time is possible to act in two different ways: leading the complex in tissues with an high microviscosity, or linking the paramagnetic complex with a macromolecule.

Electronic relaxation time T_{1e}

The relaxivity of a paramagnetic complex depends on the electronic relaxation time, closely related to the magnetic characteristics of the metal, and at a lower rate to the structure of the ligand.

Paramagnetic metal ions show an effect which depends on the number of unpaired electrons in the ion. Paramagnetic ions of various transition metals like Fe^{3+}, Mn^{2+} and rare earth metals of the lanthanide series like Gd^{3+}, Dy^{3+} etc., have received great attention as magnetopharmaceuticals. The choice of Gd(III) would be expected, for no other ion has seven unpaired electrons. But there is a much

more subtle reason it performs so well. Two other lanthanide ions, dysprosium(III) and holmium(III), have larger magnetic moments (due to orbital contributions to electron angular momentum) than that of Gd(III), but the asymmetry of these electronic states leads to very rapid electron spin relaxation. The symmetric S-state of Gd(III) is a more hospitable environment for electron spins, leading to a much slower electronic relaxation rate.

This condition is best met in Mn^{2+}, Fe^{3+} and Gd^{3+}.

Atomic number	ion	Electronic configuaration	3d	4f	Bohr magneton
25	Mn^{2+}	$[Ar]3d^{5}4s^{0}$	↑↑↑↑↑		5.9
26	Fe^{3+}	$[Ar]3^{d}54s^{0}$	↑↑↑↑↑		5.9
64	Gd^{3+}	$[Xe]4f^{7}6s^{0}$		↑↑↑↑↑ ↑↑	7.9

Table 1: electronic configuration of some paramagnetic metals

Gadolinium(III) chelates

Gadolinium(III) chelates represent an important class of contrast agents for Magnetic Resonance Imaging (MRI). In the past two decades the use of gadolinium complexes of simple polyaminopolycarboxylic ligands as extracellular MRI contrast agents has become widespread. The main problem of the medical utilizations of heavy metal ions like the Gd(III) ion is a significant toxicity of their “free” (aqua-ion) form. Thus, for clinical use of gadolinium, it must be wrapped in a complex of high stability and, even more importantly, it must show a long-term resistance to a transmetallation/transchelation loss of the Gd(III) ion. It was proved that the endogenous metal ions Zn(II) and Ca(II) are them a in competitors and, thus, the candidate ligand has to show a higher complexation selectivity for Gd(III)

than for the two cations. The most important toxicological feature of the complex is the rate of decomplexation/transmetallation in comparison with the rate of excretion of the complex from the body. The requirements for *in vivo* stability suggest that kinetic stability, also called kinetic inertness, of the complexes could be as important as their thermodynamic stability.

From the structural point of view, two main families of organic ligands have been developed: twelve membered tetraazamacrocyclic cyclen derivatives (cyclen = 1,4,7,10-tetraazacyclododecane) and acyclic triamines (diethylenetriamine derivatives) with several chelating side arms, affording an octadentate model of the ligands.

The coordination number of the Gd(III) ion in these complexes is nine with the last coordination site occupied by a water molecule, which is crucial for the contrast enhancement mechanism.

Therefore, some important parameters to be taken in exam when designing a new Gd^{3+} contrast agent are:

- *High stability*. The injection of gram amounts of gadolinium into patients presents some potential toxicity problems which requires strong metal complexation by the parent ligand.
- *Good water solubility and low osmolality of the solutions used clinically*. Injection of relatively small volumes of a concentrated solutions of the metal complex is required.
- *High relaxivity*. The dependence of the relaxivity on structural features of the paramagnetic compounds represent an important area of research

The clinically approved Gd-based CAs are reported in Figure 5.

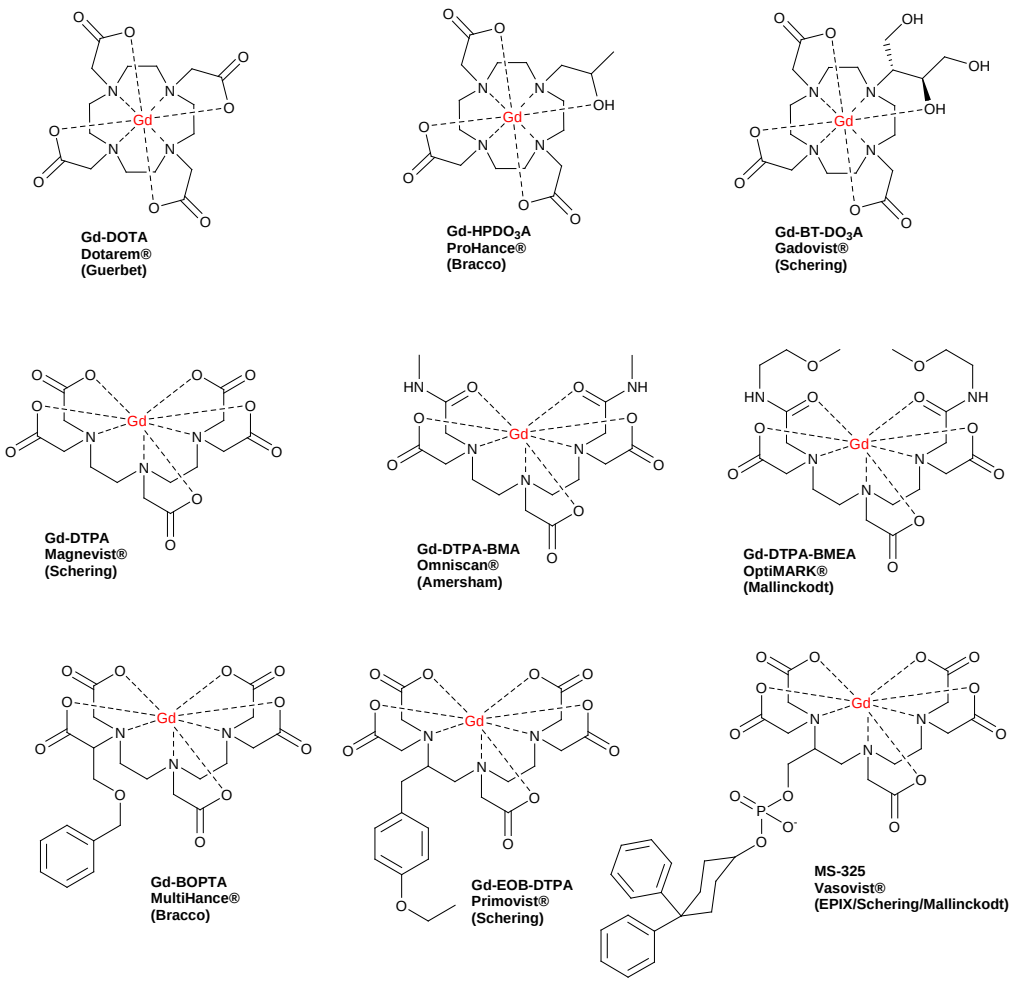

Figure 5: Clinically used gadolinium contrast agents

The first six complexes shown in Figure 5 act as nonspecific extracellular agents. Following intravascular injection, these compounds distribute rapidly between plasma and interstitial spaces and are ultimately eliminated through the renal route with half-lives of about 1.6 h. The remaining three DTPA derivatives, $[Gd(EOB\text{-}DTPA)(H_2O)]^{2-}$, MS-325, and $[Gd\text{-}(BOPTA)(H_2O)]^{2-}$, are designed specifically as targeted agents. The BOPTA comple is known to target the hepatobiliary system and acts as a liver imaging agent, while MS-325 interacts non-covalently with the abundant blood protein human serum albumin (HSA).

1.2.1 Bifunctional Chelating Agents (BFCAs)

The labelling of biomolecules with metal ions of diagnostic or therapeutic interest is an important tool in medicine.

Different metal ions are widely used in diagnostic and can be divided according to the techniques into they which are employed (Table 2).

Technique	Metal ions	Examples
MRI	Gd^{3+}, Mn^{2+}	Gd-DTPA-BMA (Omniscan®) Approved for body imaging, MR angiography, central nervous system imaging.
PET	$^{60,61,62,63,64}Cu^{2+}$, $^{66,68}Ga^{3+}$, $^{86}Y^{3+}$, $^{89}Zr^{4+}$	^{68}Ga-DOTATOC Approved for neuroendocrine tumor management.
SPECT	$^{67}Cu^{2+}$, $^{67}Ga^{3+}$, $^{90}Y^{3+}$, ^{99m}Tc, $^{111}In^{3+}$	^{99m}Tc-exametazime (Ceretec®) Approved for cerebrovascular diseases.

Table 2

Labelling of biomolecules with contrast agents is usually performed by directly linking the two moieties with a covalent linkage.

Several examples of MRI CAs directly bound to biomolecules are reported in the literature: for example a progesterone-Gd(III) chelate conjugate designed to image progesterone receptors for early detection of hormone related cancers[9], or gadolinium chelates conjugated to peptides, as in the case of an arginine octamer prepared by standard peptide synthesis techniques on solid-phase resins, coupled to a Gd(III)-DTPA and used as a transporter across cellular membranes[10]. (Figure 6)

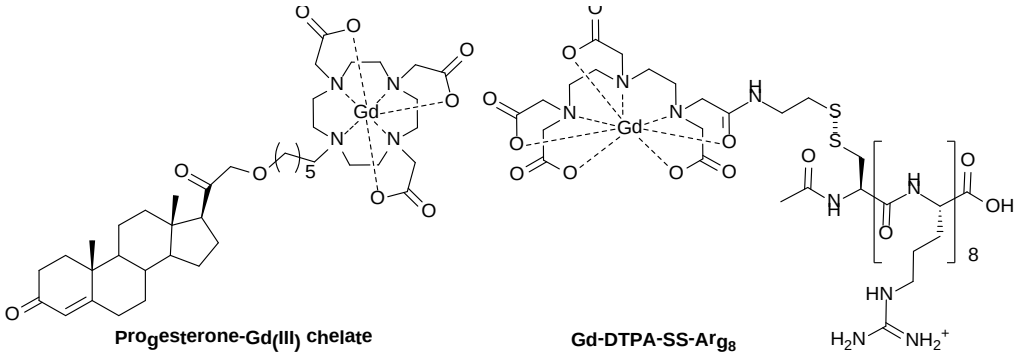

Figure 6

A different approach can be used for MRI CAs, relying on a reversible interaction of the CA with the desired biomolecule. This strategy is exemplified by MS-325 (Figure 7)[11], a Gd^{3+}-complex containing a diphenylcyclohexyl apolar residue, bound to the metal coordination cage through a phosphodiester group. The apolar residue shows a strong affinity for human serum albumin (HSA), tightly binding to one of the hydrophobic pockets of this globular transport protein. The binding to HSA allows to modify the biodistribution of the CA while the reversible nature of the interaction warrant its excretion by glomerular filtration.

A similar approach was pursued with LipoAAZTA, where an aliphatic C_{17} straight chain plays the role of a fatty acid and binds strongly but reversibly to the dedicated pockets of HSA.[12]

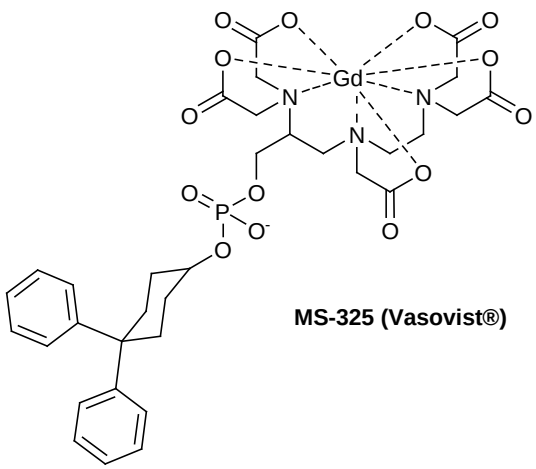

MS-325 (Vasovist®)

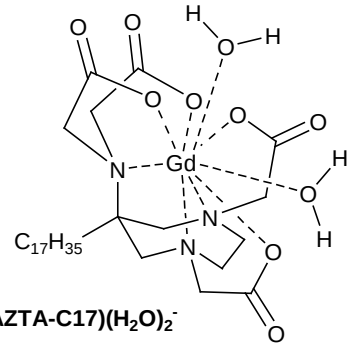

Gd(AAZTA-C17)(H_2O)$_2^-$

Figure 7

Complexes of positron ($^{64}Cu^{2+}$, $^{68}Ga^{3+}$) or gamma ($^{90}Y^{3+}$, ^{99m}Tc) emitting radionuclides are largely used in positron emission tomography (PET) or single photon emission computed tomography (SPECT) respectively, a DTPA derivative (Figura 8) linkage with an analog somatostatine peptide (OC), is a SPECT imaging agent approved for routine clinical use as a diagnostic agent for neuroendocrine cancer in the US and Europe.[13]

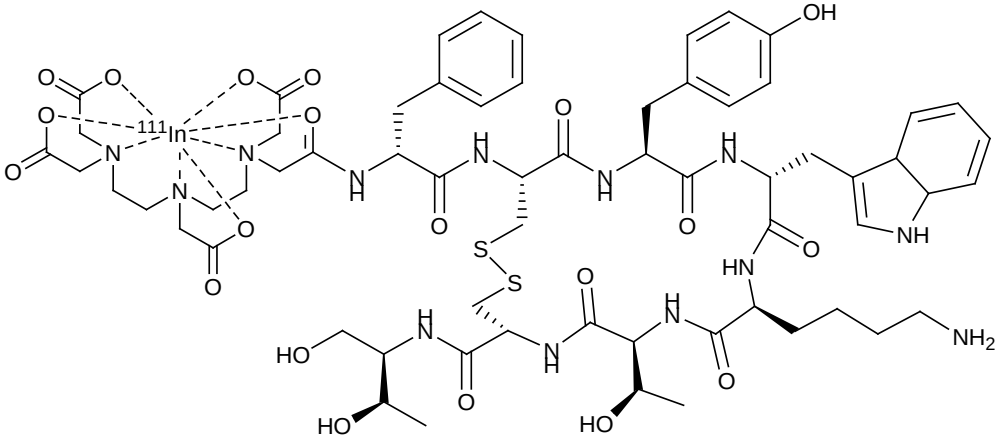

^{111}In-DTPA-OC (Octreoscan®)

Figure 8

Radionuclides are also employed in therapy, in particular in the treatment of cancer, and can be generate beta ($^{90}Y^{3+}$, $^{177}Lu^{3+}$) or alpha ($^{212}Bi^{3+}$, $^{226}Ac^{3+}$) particles[14]. Ibritumomab tiuxetan (Zevalin®) is a monoclonal antibody conjugated with the chelator tiuxetan, to which a radioactive isotope ($^{90}Y^{3+}$ or $^{111}Y^{3+}$) is added. Tiuxetan is a modified version of DTPA whose carbon backbone contains additional isothiocyanatobenzyl and methyl groups.[15]

For the most part, clinical contrast agents are not specifically targeted to a protein or receptor. The linkage between these biomolecules increases the molecular specificity and allows their delivery to particular sites of human body. The biomolecules employed, usually peptides or monoclonal antibodies, are able to target particular kinds of cells with high selectivity and affinity.

For MRI agents, the detection limit for a single Gd(III) complex is in the low micromolar range, and it is often necessary to incorporate multiple complexes to enhance molecular relaxivity. Non-covalent protein binding and oligomerization often result in increased relaxivity per Gd ion, because largest molecules increase the rotational correlation time (τ_R). The most reliable and frequently applied method of linking the metal ion (the probe) to the biomolecule (the carrier) is by means of a bifunctional chelating agent (BFCA).

Bifunctional chelating agents are defined as molecules containing two different moieties: a strong metal chelating unit and a reactive functional group (figure 9).

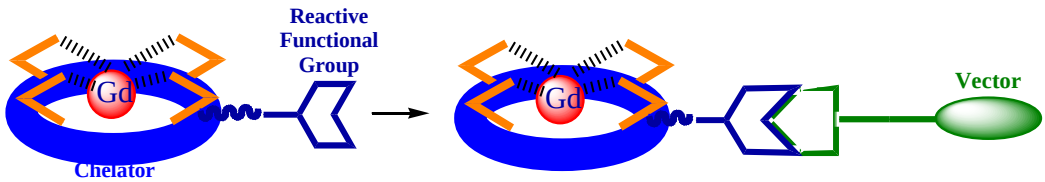

Figure 9

The chelating unit is committed to the stable coordination of the chosen metal ion. The reactive functional group is devoted to react and give a stable covalent

bond with suitable vectors, represented by biomolecules or simple organic compounds.

In recent years, a large number of BFCAs have appeared in the literature, those based on a polyamino polycarboxylic ligand are particularly efficient (figure 10). The main reason for this is that they form highly stable complexes with a wide variety of metal ions, this means that the undesired *in vivo* release of the metal ion is avoided.

BFCAs can be divided into two main categories: acyclic, such as those based on the ligands EDTA or DTPA, and macrocyclic, such as those based on the ligands DOTA or TETA. In general, the differences between these two classes are in the stability of complexes (macrocyclics are more stable than acyclics) but macrocyclic ligands are usually kinetically more inert during complexation, requiring longer reaction times and/or higher temperatures.

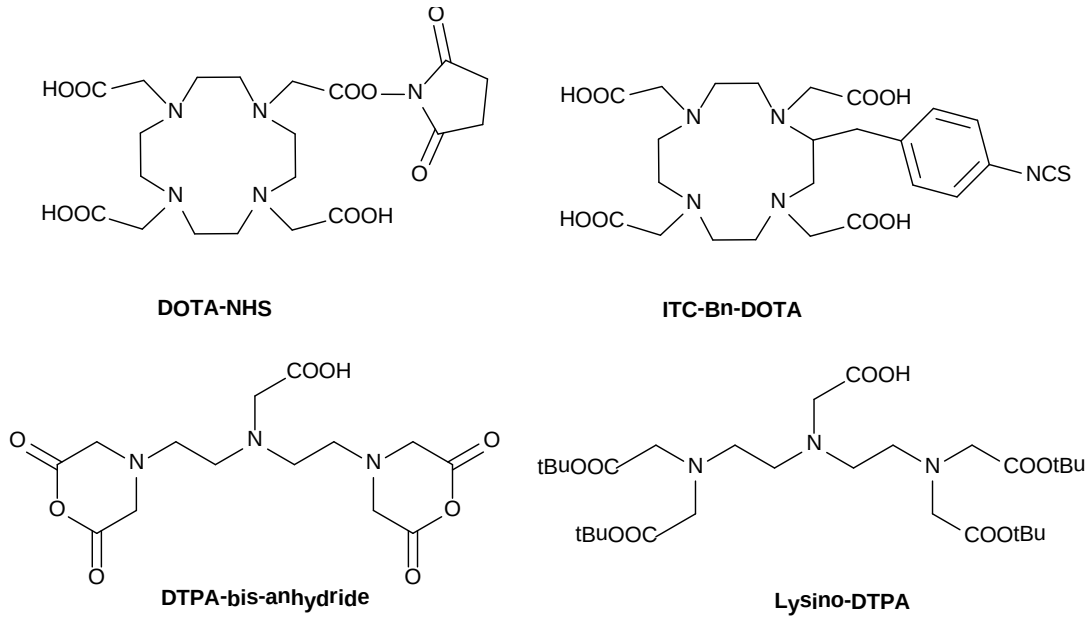

Figure 10: Some examples of BFCAs

The choice of the right ligand is a crucial point in the design of the final conjugate and depends both on the metal ion to be complexed and the biomolecule to be labeled.

The conjugation of a BFCA to the molecule of interest (the carrier) can be performed by means of the reactive functional group. The carboxylic group is the most used, since it can be easily activated to allow attack by an amino group present in antibody or in peptide. A huge number of functional groups are reported in the literature for this aims: symmetrical or mixed anhydrides and active esters (such as pentafluorophenyl, *p*-nitrophenyl and NHS-esters) isothiocyanate and maleimide are frequently used reactive groups.

Another important parameter to consider in the design of new BFCAs is the linker (or spacer, the spacing unit between the probe and the functional group). The linker can increase the water solubility of the molecule (ex. PEG chain) or increase its lipophilicity (aliphatic chains, aromatic rings), affecting the pharmacokinetics and the biodistribution of the final molecule biodegradation and elimination can be increased by linkers that can be cleaved *in vivo*, such as particular peptide sequences, ester/amide groups and disulfide bonds.

The list of bifunctional ligands reported in the scientific literature is very long as several and different chelating agents have been modified with additional reactive functional groups depending on the metal ion to be complexed and the specific application involved. The comprehensive treatment of BFCAs is beyond the scope of this thesis and may be found in dedicated reviews.[16,17]

A selection of the BFCAs employed for the preparation of Gd-complexes for MRI applications will be discussed in order to introduce the experimental work performed in the PhD period, focusing on the DO_3A platform (leading to DOTA-like and HP-DO_3A-like BFCAs) and on the original AAZTA ligand.

1.2.2 AAZTA (6-Amino-6-methylperhydro-1,4-diazepine-*N*,*N'*,*N"*,*N"*-tetracetic acid)

The structure of AAZTA embodies a seven-membered ring with two endocyclic and one exocyclic nitrogen atoms, carrying a total of four carboxymethyl side arms[18]. The corresponding Gd^{3+}-complex is satisfactorily stable, either thermodynamically ($logK_f$ = 20.5),[19] kinetically or with respect to transmetallation (table 2). The two coordinated water molecules ensure a high relaxivity (7.1 $mM^{-1}s^{-1}$), not quenched by bidentate anions such as lactate and phosphate as observed in macrocyclic complexes.

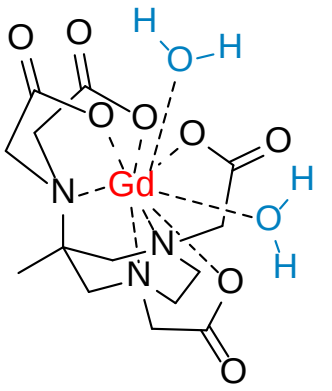

$Gd(AAZTA)(H_2O)_2^-$

r_1p = 7.1 mM-1s-1

τ_M = 90ns

Figure 11

Metal ion	AAZTA $LogK_{ML}$	DTPA $LogK_{ML}$	Metal ion	AAZTA $LogK_{ML}$	DTPA $LogK_{ML}$
K^+	1.3	---	La^{3+}	17.53	19.48
Mg^{2+}	8.31	9.27	Nd^{3+}	19.41	21.6
Ca^{2+}	12.76	10.75	Eu^{3+}	19.93	22.39
Cu^{2+}	22.27[a]	23.4[a]	Gd^{3+}	20.24	22.46
Mn^{2+}	15.44	15.2	Dy^{3+}	20.39	22.82
Ga^{3+}	22.18	24.3	Yb^{3+}	21.59	22.62
In^{3+}	29.58	29.48	Lu^{3+}	21.85	22.44

Table 2: Metal ion affinity of AAZTA and DTPA

The synthesis of AAZTA (Scheme 1) involves 4 synthetic steps with an overall 50% yield; the easy synthetic access to this ligand, combined with the interesting proprieties of its paramagnetic complexes, prompted different groups to prepare different versions of BFCA-AAZTA.

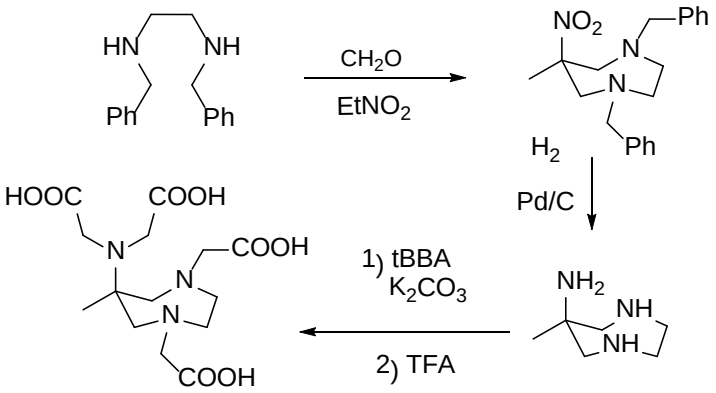

Scheme 1: Synthesis of AAZTA

The synthetic access to AAZTA allows the reactive functional group to be positioned on the ring (especially on the quaternary carbon atom bearing the iminodiacetic moiety, *i.e.*: C-6) or on one of carboxymethyl lateral arms.

The first BFCA of AAZTA was obtained introducing a functional group containing a hydroxyl group, spaced with one carbon atom from the ring [20]. In this synthesis, nitromethane was substituted with 2-nitroethanol to give as a product of double nitro-Mannich reaction a new hydroxyl functional group (scheme 2). It has been demonstrated that is possible to obtain the product forming in situ 2-nitroethanol through the Henry reaction by using nitromethane and an excess of paraformaldehyde, but the yield is reduced to about 60%.

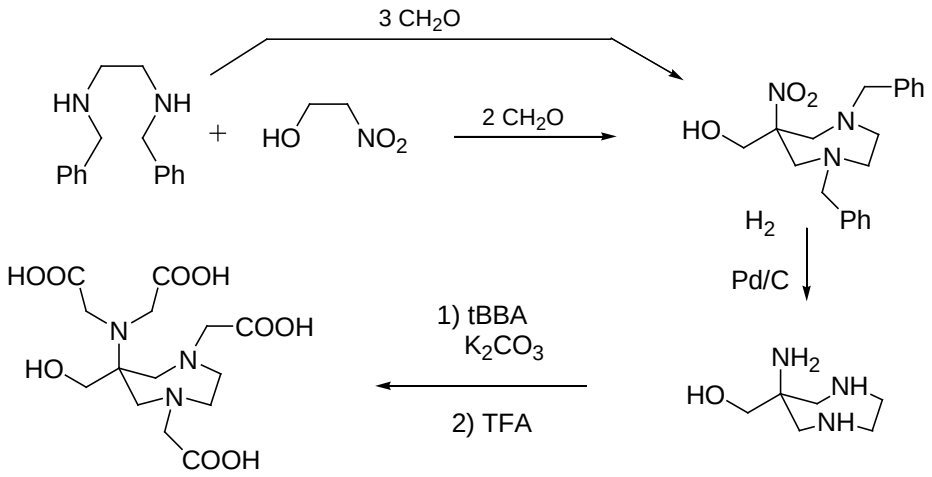

Scheme 2

The hydroxyl group was also used to introduce a carboxylic group by reaction with succinic anhydride; alternatively the protected ligand was reacted with thionyl chloride to convert the hydroxymethyl group into a 6-chloromethyl derivate. In a third strategy, this compound was reacted with 4-nitrophenyl isocyanate and after that treated with thiophosgene to give a isothiocyanate derivate (Scheme 3).

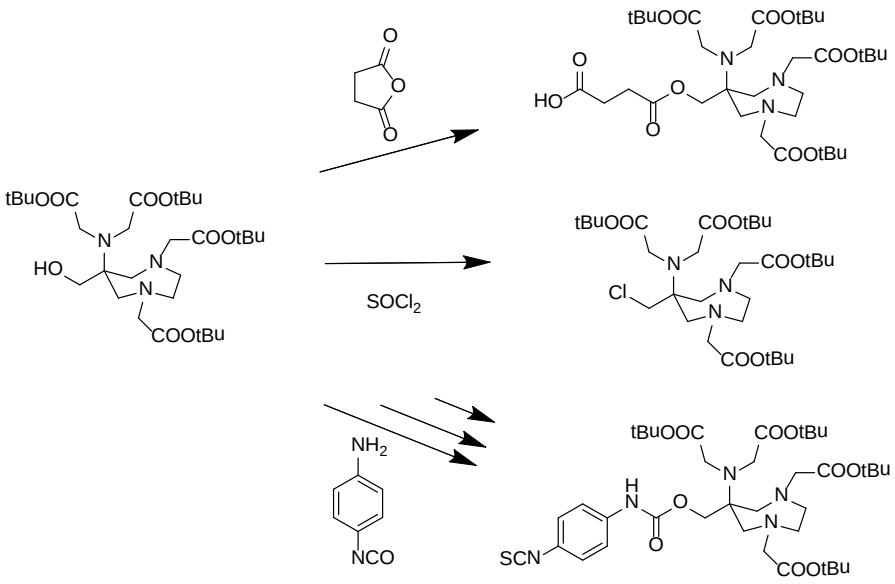

Scheme 3

These compounds were used to prepare lipid-based paramagnetic particles used for the cell labelling or conjugated with small biomolecules. In addition the isothyocianate derivate has been employed to synthesise multimeric/dendrimeric MRI contrast agents[21,22,23,24].

Other similar hydroxyl derivates were synthesized with a higher number of carbon atoms in the spacer [25], however the synthetic route is parallel to that shown in Scheme 2.

It has been reported another BFCA AAZTA-like with an amine moiety as reactive group, bounded to the ring with a little spacer of three carbon atoms (Scheme 4) [26]. This synthetic approach is recalls the strategy used for the previously reported derivatives, the key step being the double nitro-Mannich reaction with 3-nitropropanamine, previously protected as *N*-Boc.

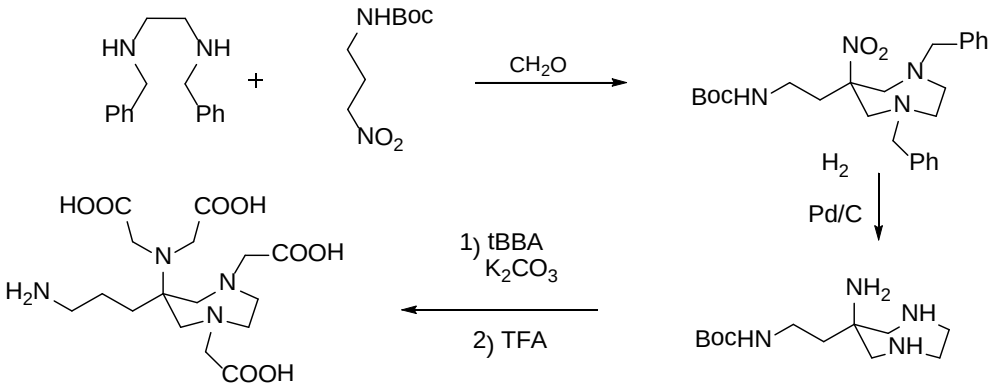

Scheme 4

A further modification of AAZTA skeleton was made using 6-nitrohexanoic acid for the condensation reaction, obtaining a derivate with a free carboxylic acid moiety[27] (Scheme 5) This derivative was subsequently conjugated with dextran and used for neuroanatomical connectivity studies.

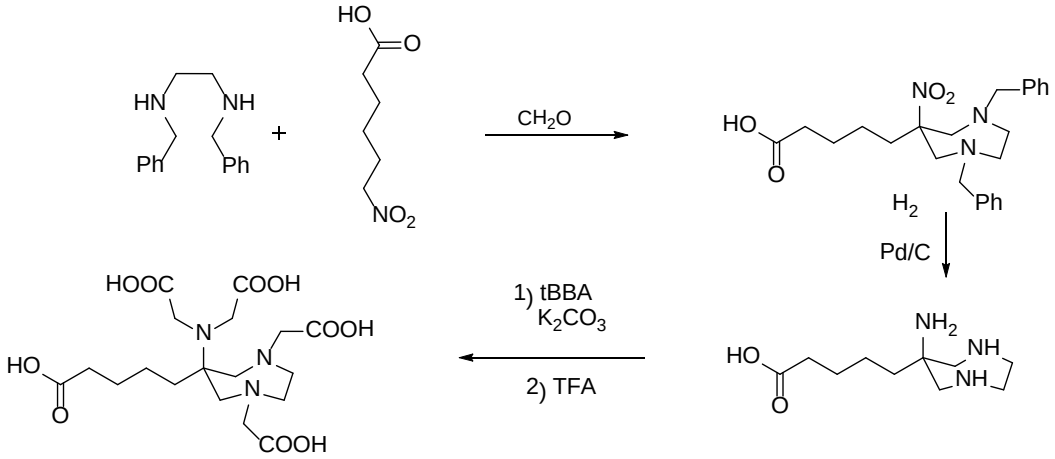

Scheme 5

All these AAZTA-like BFCAs share the common synthetic pathway, relying on the double nitro-Mannich reaction of *N,N'*-dibenzylethylenediamine, paraformaldheyde and a suitable nitroalkane in order to build a 7-membered ring. As a matter of fact, these agents are substituted on position 6 of the

perhydrodiazepine ring with aliphatic spacer chains of different lengths characterized by functional reactive groups located at the end and devised to be conjugated.

Different AAZTA-based BFCAs were obtained by selective alkylation at one of the secondary amine groups with tert-buthyl α-bromoester carryng a protected functional group at ω; alkylation of the remaining amine groups with *t*BBA (= *tert*-butyl bromoacetate) followed by deprotection of the reactive functional group gave corresponding AAZTA[28] as shown in scheme 6.

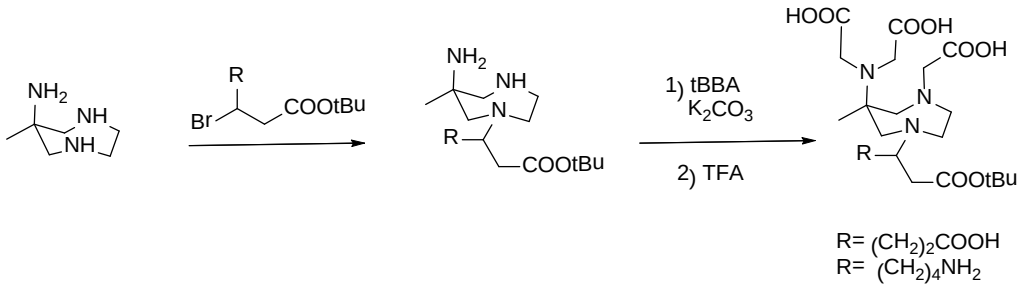

Scheme 6

1.2.3 DO_3A (1,4,7,10-tetraazacyclododecane-1,4,7-triacetic acid)

DO_3A is a heptadentate ligand composed by four macrocyclic nitrogen atoms and three carboxylates. This chelator can be easily derivatized on the unique nitrogen on the macrocyclic ring, to obtain several other DO_3A-like BFCAs.

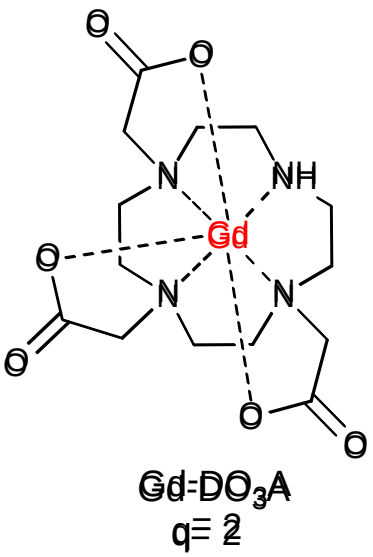

DO_3A form stable complexes with a large number of metal ion such as transition metal ions and lanthanides, leaving two coordinated sites free for the binding of water molecules and giving neutral complexes with low osmolality.[29] In the case of

lanthanides complexes and especially for the Gd^{3+} complex this means an improvement in the relaxivity value; nevertheless *in vivo* several bidentate anions such as carbonate or phosphate can displace the coordinated water molecules, quenching the relaxivity and preventing in this way its application as a MRI agent.[30,31,32.]

The synthesis of DO_3A can be performed in different ways, firstly by direct alkylation of cyclen with bromoacetic acid in DMF or DMAc with subsequently purification, by ion exchange chromatography, from DOTA[33]. A recent improved method for synthesized DO_3A involves the alkylation of cyclen with *t*BBA in dimethyl acetamide with sodium acetate as a base. After 60 h of reaction at room temperature the tri-*t*-butyl ester was obtained after crystallization with a 65% yield as hydrobromide.[34] (Scheme 7)

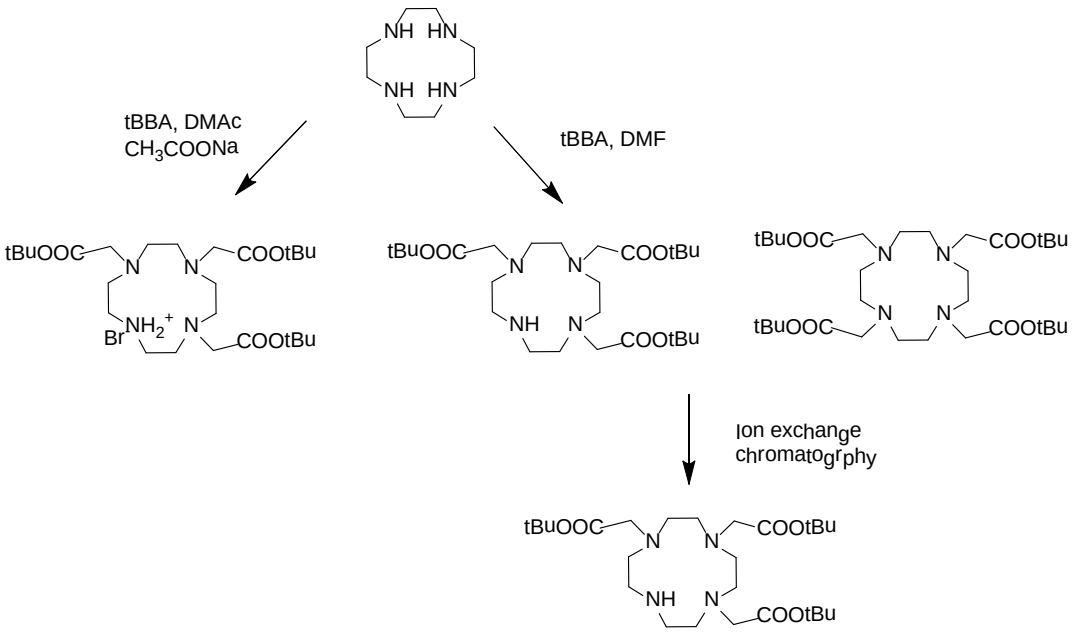

Scheme 7

Another synthetic pathway involves the trivalent protection of cyclen with dimethylformamide dimethylacetal to give a tricycloderivate, subsequently hydrolysed with 50% aqueous ethanol to mono-*N*-formylcyclen. Subsequently the product was alkylated with *t*BBA followed by the combined hydrolysis of *tert*-butyl esters and the formyl group with H_2SO_4 to give DO_3A in high yields.[35] (*Scheme 8*).

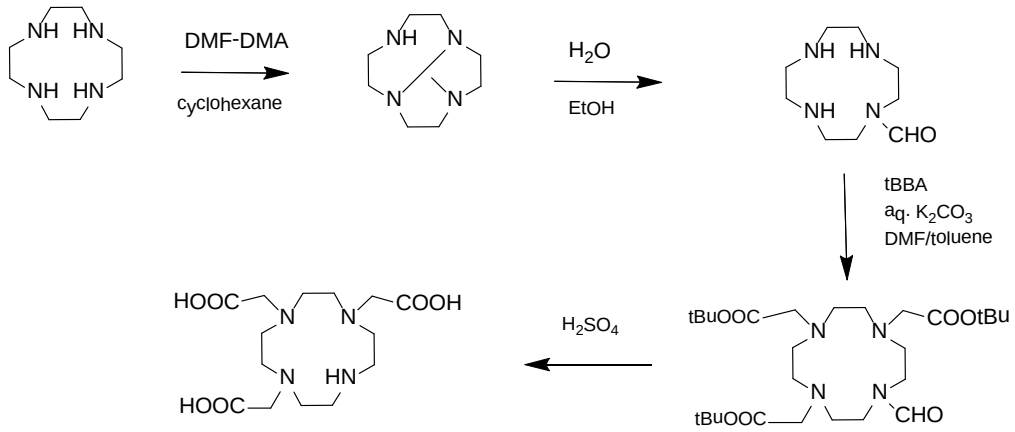

Scheme 8

By alkylation of the secondary amino group of DO_3A is possible to obtain a series of new BFCA-DO_3A like. A huge number of functional groups are introduced into the DO3A skeleton, with different kind of linkers, amino groups[36,37], isothiocyanate[38], thiol[39], bromo[40], vinylsulfone[41] and squarate ethylester[42] are selected examples (Scheme 9).

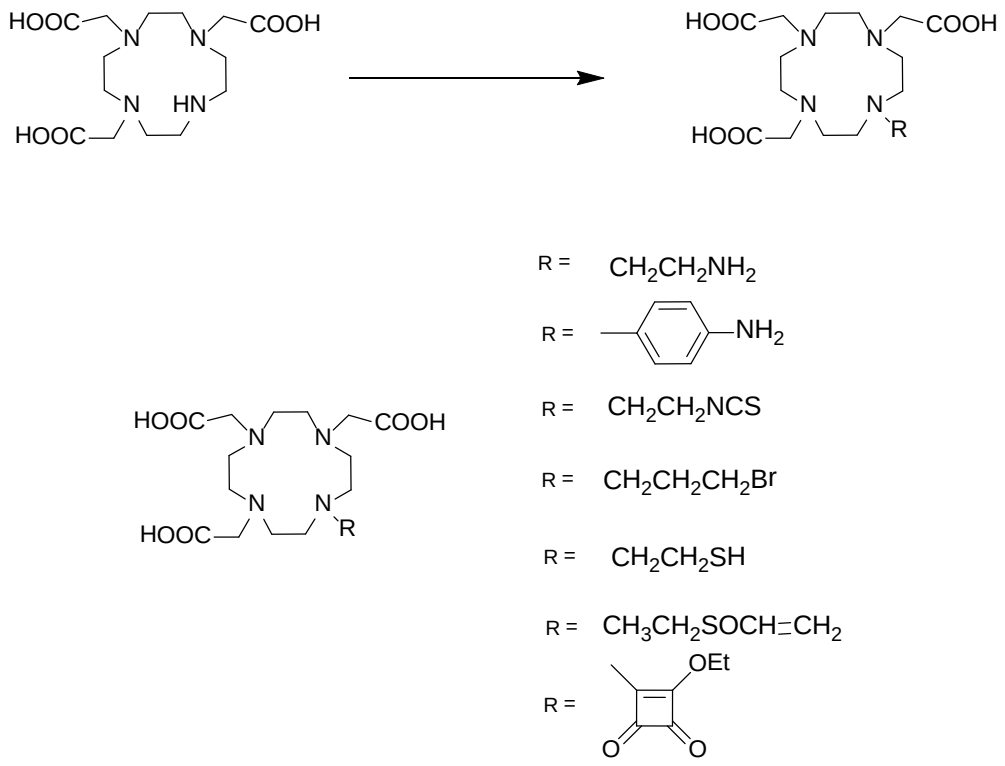

Scheme 9

All these compounds were used in a wide variety of applications, for examples the derivativee with amino moiety was conjugated to fluorescein isothyocianate in order to obtain a dual probe for MRI and Optical Imaging. The Sm(III) complex of the thiol derivative was employed in a biodistribution study, while the vinylsulfone moiety was conjugated to humanized antibodies for PET imaging. In another example the free amino group of DO_3A was functionalized with a squarate ester, the latter being reactive towards amines and used for the multisite labeling of poly-*L*-lysines and poly-*L*-ornithines.[43]

An interesting examples of DO_3A derivative was generated using propargyl bromide as alkylating agent (Scheme 10). This compound can be easily and rapidly conjugated to peptides by a Huisgen cycloaddition[44]. Copper(I) catalyzed cycloaddition of this compound with azides, produced an octadentate complex wherein a triazole nitrogen is involved in the coordination to the lanthanide.

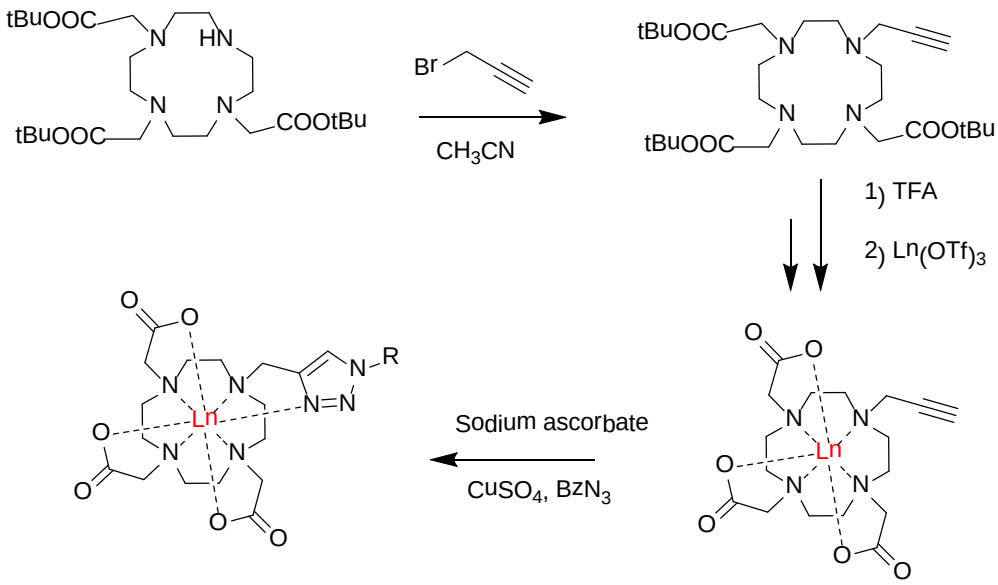

Scheme 10

The introduction of a methylphosphinic acid moiety on the DO_3A structure results in Gd(III) complexes that show a fast coordinated water exchange rate, which is close to optimal for low field application (0,5-1,5 T)[45]. The reason for such a fast exchange rate can be found in the steric constraint imposed by the bulky phosphinate group on the water coordination site and possibly in the structuring of the second hydration sphere brought about by the phosphinate moiety. To take advantage of this favorable water exchange property, two Bifunctional monophosphinate DO3A-Like were prepared, bearing either a free carboxyl group or an aromatic amine ready for conjugation[46] as shown in figure 12.

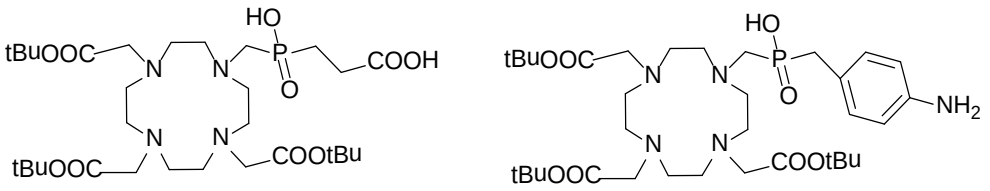

Figure 12

A DO_3A-like ligand with a 2-mehylpyridine-N-oxide coordinating unit formed a Gd(III) complex with a remarkably fast water exchange rate[47]. A derivative with a free carboxylic available for functionalization was conjugated to a calix[4]arene platform.[48] (Figure 13)

A different BFCA DO_3A-like was obtained introducing an acylhydrazine moiety as shown in figure 13 and subsequently used to prepare acid labile conjugates with doxorubicin, an anthracycline anticancer drug[49].

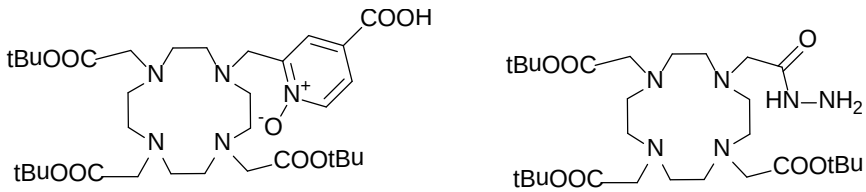

Figure 13

An interesting example of DO_3A BFCA with a aniline as a functional group was reported[50]. This compound was also conjugated with a galactopyranosyl moiety, as a substrate of β-galactosidase, an expression-product of the report gene *Lac*-Z commonly co-administrated intracellulary with the subject-gene of gene-therapy studies. The synthetic pathway of this compound (scheme 11) is composed by three different alkylation steps with (*R,S*)-2-bromo-4-(4-nitrophenyl)butanoate, bromoethyl-β-*D*-galactopyranoside tetraacetate and *t*BBA. Consecutive carboxyl and hydroxyl group deprotections and catalytic hydrogenation of functional group gave a corrisponding BFCA DO_3A-like.

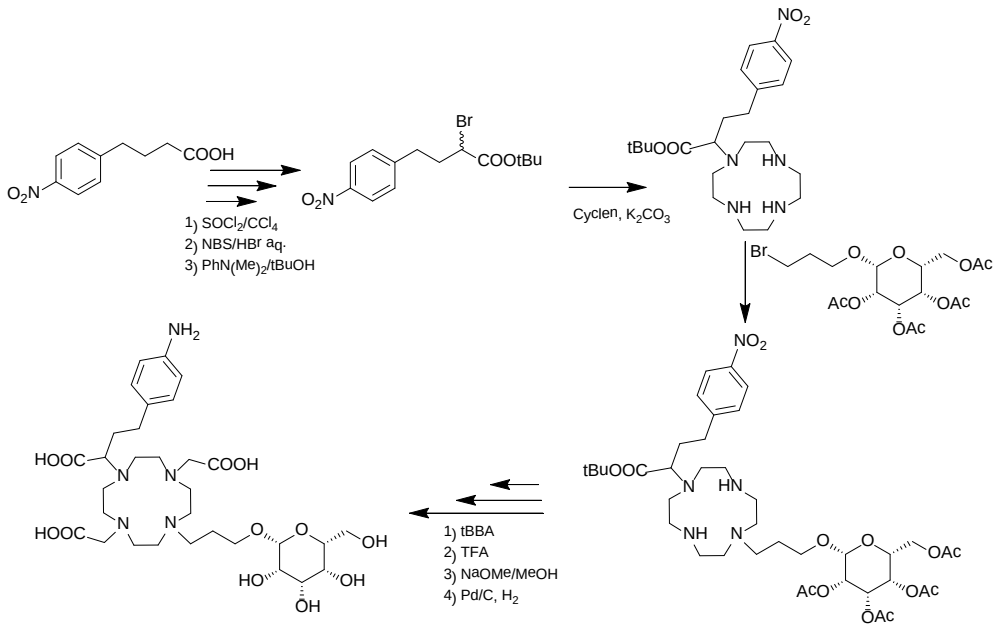

Scheme 11

1.2.4 DOTA Monoamide

This class of chelating agents requires a separate systematic treatment. In fact, for the synthesis of DOTA monoamide BFCAs is possible to start from DOTA, for example activating one of the carboxyl groups as N-hydroxysuccinimide ester, or from DO_3A by an alkylation of the secondary free amino group, or from cyclen by monoalkylation with a suitable N-substituted 2-haloacetamide as reported in Scheme 12. These approaches differ in the starting material, the number of steps, yields and ease of purification. The differences between these DOTA monoamide derivatives are related to the functional groups used to conjugated the probe to the vector of interest and to the linkers of various length, rigidity or hydrophylicity used to space the metal chelate from the biomolecule. The distance between the DOTA coordination cage and the vector may strongly affect both the conjugation reaction and the interaction of the bioconjugate interaction. Indeed, the DOTA

monoamide cage, which is often bulkier than the vector itself, may hinder the interaction considerably.

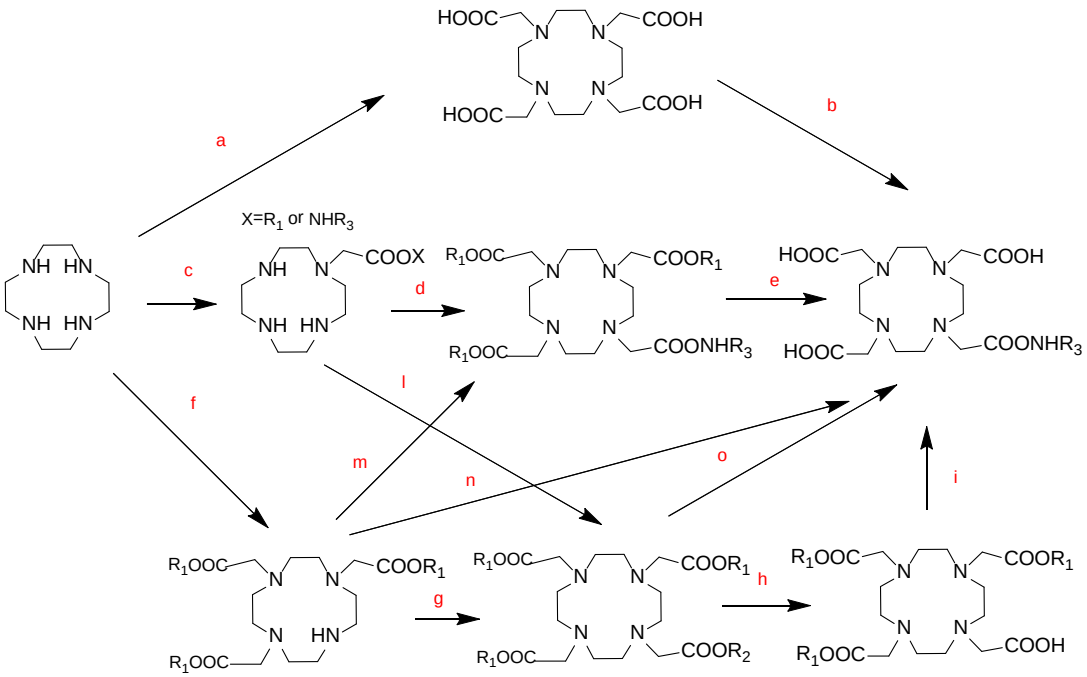

Scheme 12: Schematic representation of the various strategies used to prepare DOTA monoamides. a-b = via DOTA, c-d-e/c-l-o = via cyclen, f-g-h-i/f-m-e/f-n/f-g-o = via DO_3A

The major part of DOTA monoamides are synthesized starting from DO_3A by alkylation on free secondary amino group. One strategy (path f,g,h,i) involves the use of one different protecting groups on the acetic pendant arms, as benzyl esters[51] or ethyl esters[52,53] (Scheme 13) and after selective removal of the protecting group, it is possible to obtain a free carboxylic moiety able to be conjugated with an amine to give a monoamide derivatives in high yield.

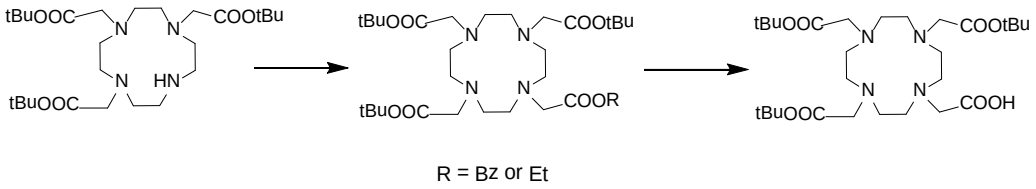

Scheme 13

Alkylation of DO3A *t*-butyl ester was also used to prepare BFCAs DOTA monoamides with different functional groups as amino, maleimido, hydroxyl and formyl[54] as shown in *Scheme 14*. The synthesis of all the adducts share the same basic strategy. DO3A *t*-butyl ester was alkylated with a tailored bromoacetamide bearing either a protected amine or alcohol group. After deprotection of the side arm the amino derivates were converted to the maleimido derivate by reaction with 7-exooxohimic anhydride under microwave irradiation. The alcohol derivates were converted into the corresponding aldehyde by Swern oxidation.

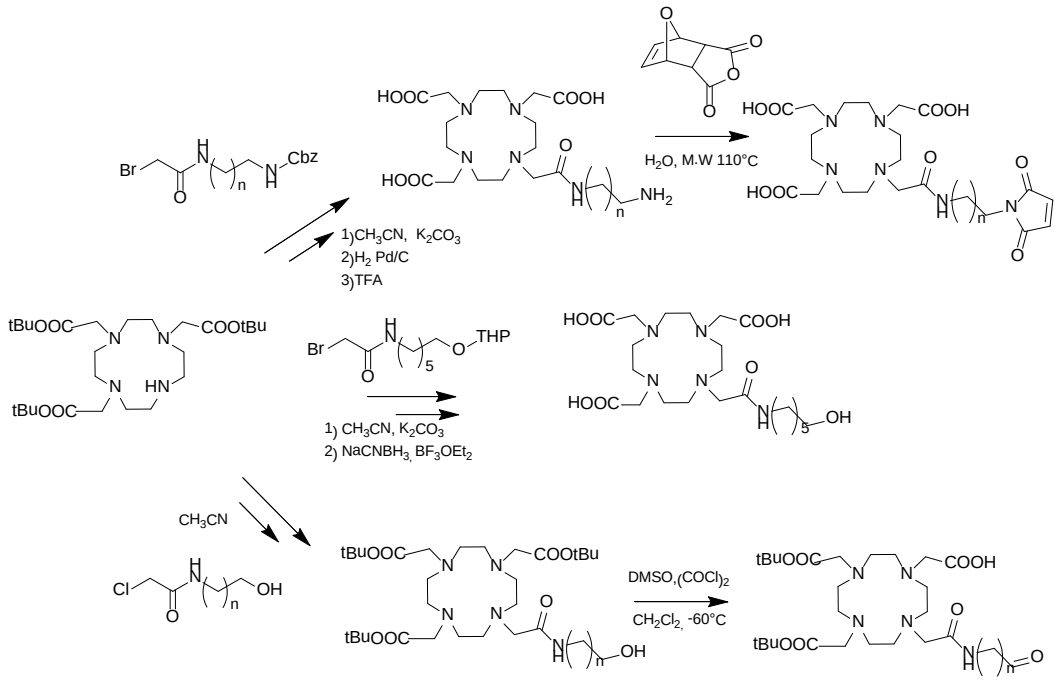

Scheme 14

Variants with a free aromatic amine and with a thiol reactive methanethiosulfate group were prepared (Figure 14) [55,56].

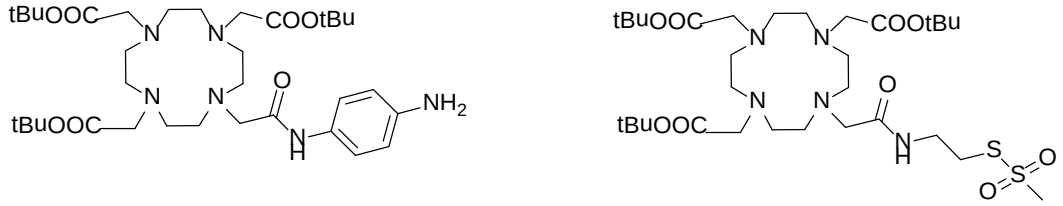

Figure 14

Functionalization of DO3A *t*-butyl ester has been exploited introducing a spacer carrying a free terminal carboxylic group (Figure 15) which, after transformation into NHS ester, was coupled to glutamine. The resulting complex was tested "*in vitro*" on different tumor cell lines and "*in vivo*" on cancer prone transgenic mice to study cellular uptake through the aminoacid transporting system[57].

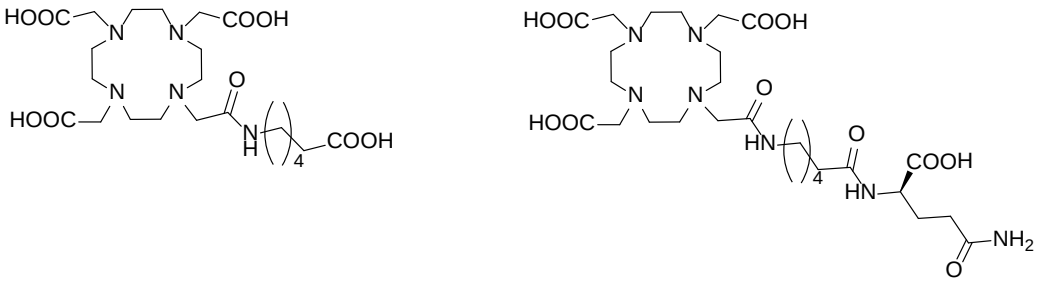

Figure 15

Final interesting examples showed that increasing the length of the carboxyamide arm of Gd-DOTA monoamide from two to three carbons atom results in gadolinium complexes with a water exchange rate almost two orders of magnitude faster than the parent DOTA monoamide[58] (Figure 16).

A DOTA monoamide with a terminal alkyne functionality, designed for Cu(I) mediated azide-alkyne cycloaddition has been prepared by alkylating DO3A *t*-butyl ester with *N*-(2-propynyl)-2-chloro- or 2-bromo-acetamide[59,60] (Figure 16).

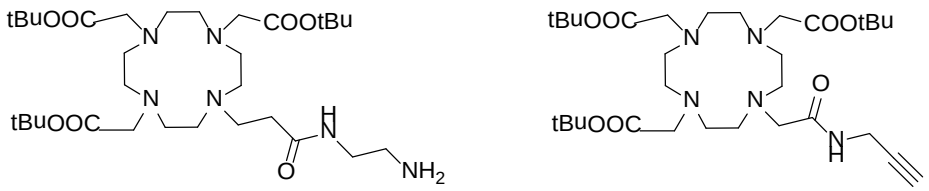

Figure 16

1.2.5 HP-DO$_3$A (10-(2-hydroxypropyl)-1,4,7,10 tetraaza-cyclododecane-1,4,7-triacetic acid)

HP-DO$_3$A is an octadentate ligand composed by four macrocyclic nitrogen atoms, three carboxymethyl side arms and a hydroxypropyl moiety. Gd-HPDO$_3$A (Prohance®, Bracco Imaging) is a non specific contrast agent for MRI, commercially available and widely employed in the clinical practice. This neutral complex shows an high thermodinamic stability (Log K_F= 23.8) and kinetic inertness that ensures no significant release of Gd^{3+} ions in *vivo*. The relaxivity value of this complex is 3.7 $mM^{-1}s^{-1}$ in water at 40°C, in line with other macrocyclic Gd complexes as shown in Table 3.[61,62]

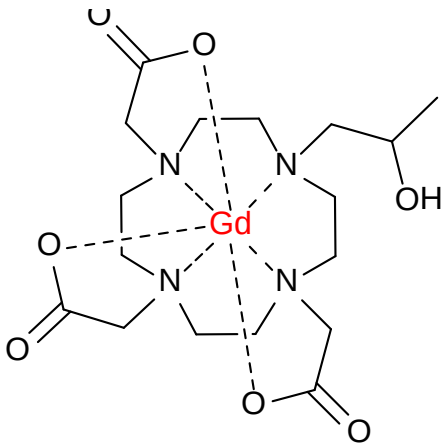

Gd-HPDO$_3$A
q= 1
r_1= 3.7 $mM^{-1}s^{-1}$

Complex	q	τ_r (ps)	r_1 $mM^{-1}s^{-1}$
Gd-$HPDO_3A$	1.3 ±0.1	57	3.7 ±0.1
Gd-$DOTA^-$	1.1±0.1	63	3.5 ±0.1
Gd-$DTPA^{2-}$	1.1±0.1	55	3.8 ±0.1
Gd-DTPA-BMA	1.1±0.1	53	3.8 ±0.1

Table 3: Comparison among some different clinically used Gd(III)-complexes.

The synthesis of HP-DO_3A, reported in Scheme 15, involves the reaction of cyclen with dimethylformamide dimethylacetal to give the tricycloderivative which was hydrolysed with 50% aqueous ethanol to mono-*N*-formylcyclen. Subsequently the product was alkylated with cloroacetic acid and without any purification steps the basic hydrolysis of the formyl group and the reaction with propylene oxide gave HP-DO_3A.

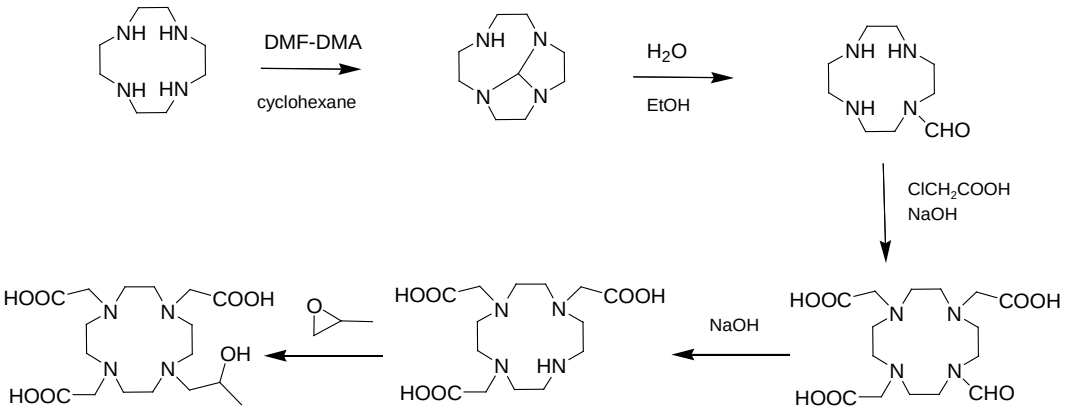

Scheme 15

In literature there are only few examples of BFCAs based on HP-DO_3A structure. In a first report, two compounds with a free carboxylic group were synthesized, in order to be conjugated to amino groups of biomolecules. Two

different linkers were used to connect the coordinating cage and the functional group, in one case a diethylene glycol unit and in the other an aromatic moiety as shown in Scheme 16. These compounds were conjugated to peptide such as bombesin and oxytocin[63].

In the first synthetic route the hydrophilic diethylene glycol spacer, protected as a benzyl ester, was prepared by a Williamson reaction using bromoacetic acid. The oxidation of terminal alkene gave the corresponded epoxide. $(tBu)_3$-DO_3A was alkylated with the epoxide and subsequently the hydrogenolysis of benzyl ester gave the desired ligand.

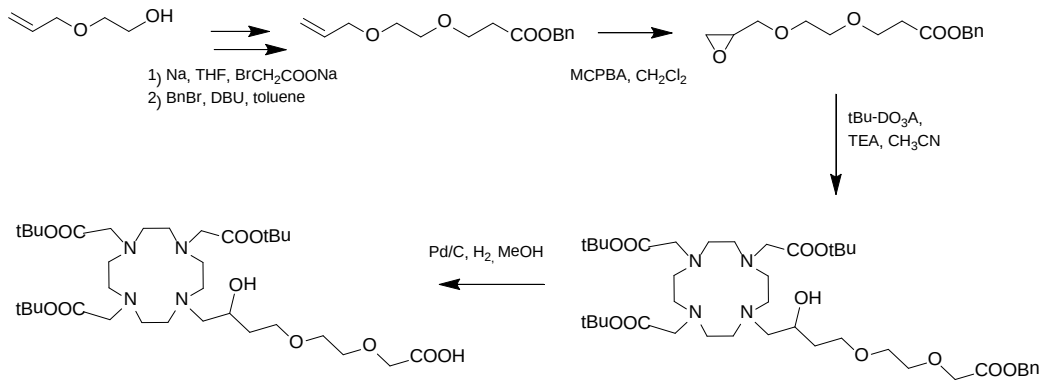

Scheme 16

A second HP-DO_3A-based BFCA containing an aromatic spacer, was synthesized in a three steps starting from epibromohydrin and benzyl 4-hydroxybenzoate. The resulting epoxide was reacted with $(tBu)_3$-DO_3A followed by the deprotection step to gave this BFCA HP-DO_3A like in a good yield (Scheme 17).

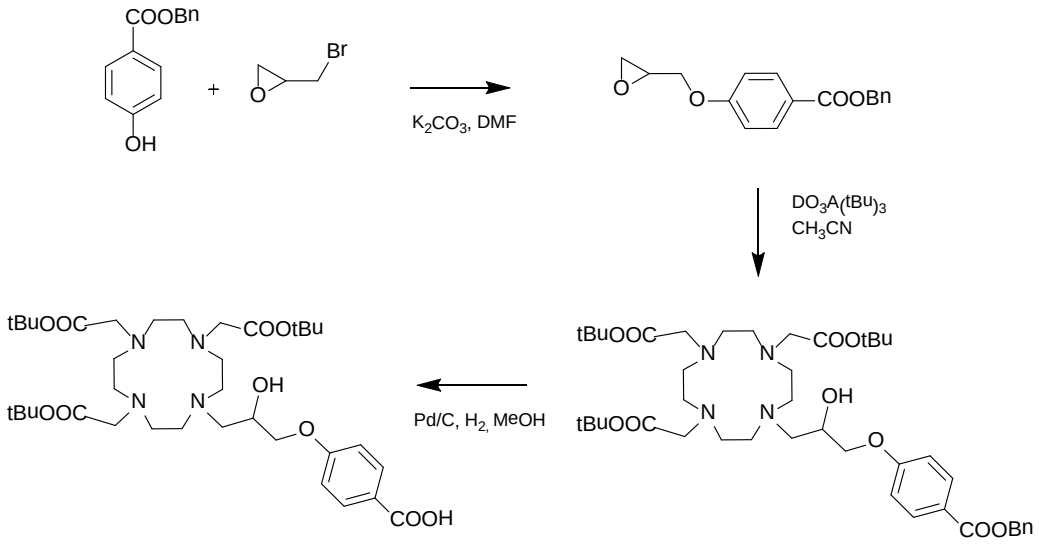

Scheme 17

The last reported HPDO$_3$A-based BFCA, endowed with a free amino moiety is shown in Scheme 18. This compound was synthesized by reaction of DO3A with *N*-Boc-1,2-epoxy-3-propylamine followed by removal of the Boc group and subsequent complexation with Gd(III)[64]. This compound was reacted with 2-iminothiolane in order to be conjugated with an activate phospholipid, and included into liposomes.

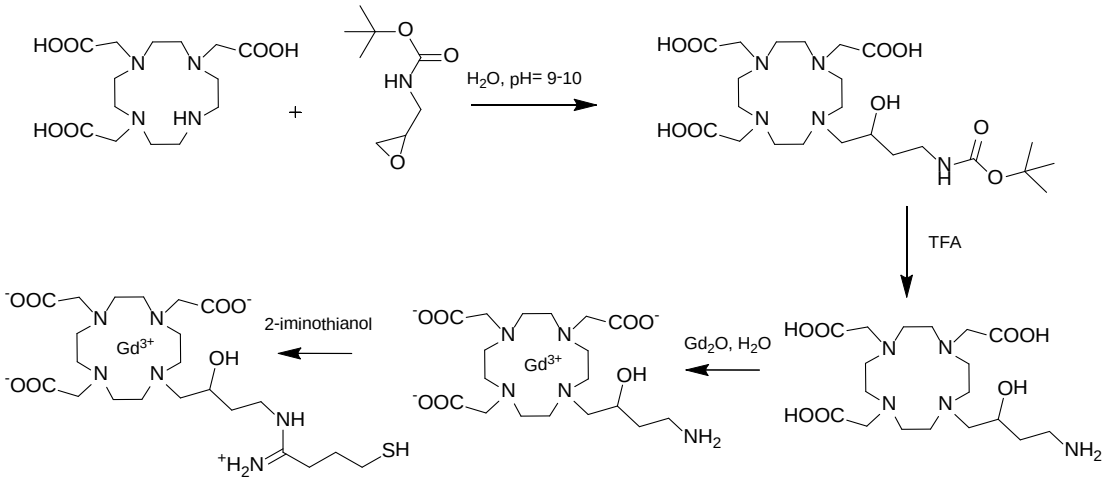
HOOC
COOH
HOOC
HN
+
O
HN
O
H2O, pH= 9-10
OH
TFA
Gd2O, H2O
Gd3+
2-iminothianol
NH
SH
NH2

Scheme 18

Reference:

1) J.P. Hornak, *The Basic of MRI*, USA **1996**.

2) R.B. Lauffer, *Chem. Rev.* **1987**, *87*, 901-927.

3) A. E. Merbach, E. Toth. *The Chemistry of Contrast Agents in Medical Magnetic Resonance Imaging*, John Wiley & Sons, LTD, Chichester, **2001**.

4) C.F.G.C. Geraldes and S. Laurent; *Contrast Media Mol. Imaging* **2009**, *4*, 1-23.

5) P. Caravan, J. J. Ellison, T. J. McMurry and R. B. Lauffer, *Chem. Rev.*, **1999**, *9*, 2293.

6) M. Botta; *Eur. J. Inorg. Chem.* **2000**, 399-407

7) E.J. Werner, A. Datta, C.J. Jocher and K.N. Raymond, *Angew. Chem. Int. Ed.* **2008**, *47*, 8568-8580.

8) P. Hermann, J. Kotek, V. Kubicek and Lukeš I., *Dalton Trans.* **2008**, 3027-3047.

9) J. Lee, J.E. Burdette, K.W. MacRenaris, D. Mustafi, T.K. Woodruff, T.J. Meade, *Chem. Biol.* **2007**, *14*, 824-834.

10) a) M.J. Allen, T.J. Meade, *J. Biol. Inorg. Chem.* **2003**, (*8)*, 746-750. b) M.J. Allen, K.W. MacRenaris, P.N. Venkatasubramanian, T.J. Meade, *Chem. Biol.* **2004**, (*11)*, 301-307. c) P.J. Endres, K.W. MacRenaris, S. Vogt, M.J. Allen, T.J. Meade, *Mol. Imaging* **2006**, *5*, 485-497.

11) R.B. Lauffer, D.J. Parmelee, S.U. Dunham, H.S. Ouellet, R.P. Dolan, S. Witte, T.J. McMurry, R.C. Walovitch, *Radiology* **1998**, *207*, 529-538.

12) E. Gianolio, G.B. Giovenzana, D. Longo, I. Longo, I. Menegotto and Silvio Aime. *Chem. Eur. J.* **2007**, *13*, 5785-5797.

13) S.W.J. Lamberts, W.H. Bakker, J.C. Reubi, E.D. Krenning, *N. Engl. J. Med.* **1990**, *32*, 1246-1249.

14) M. Steiner, D. Neri, *Clin. Cancer Res*, **2011**, *17*, 6406-6416.

15) H. Borghaei and R.J. Schilder. *Semin. Nucl. Med.* **2004**, *34(S1)*, 4-9.

16) L. Lattuada, A. Barge, G. Cravotto, G.B. Giovenzana and L. Tei, *Chem. Soc. Rev.* **2011**, *40*, 3019-3049.

17) L. Frullano and P. Caravan. *Curr. Org. Synth.* **2011**, *8*, 535-565.

18) S. Aime, L. Calabi, C. Cavallotti, *Inorg. Chem.* **2004**, *43*, 7588-7590.

19) Z. Baranyai, F. Uggeri, G.B. Giovenzana, A. Bényei, E. Brücher, and S, Aime. *Chem. Eur. J.* **2009**, *15*, 1696-1705.

20) G. Gugliotta, M. Botta, G.B. Giovenzana and L. Tei, *Bioorg. & Med. Chem. Lett.* **2009**, *19*, 3442-3444.

21) G. Gugliotta, M. Botta and L. Tei, *Org. Biomol. Chem.* **2010**, 1-6.

22) G. Gambino, J. Engelmann, L. Tei, M. Botta, N.K. Logothetis, I. Mamedov, *Biomaterials* **2013**, *34*, 7135-7142.

23) G. Gambino, S. De Pinto, L. Tei, C. Cassino, F. Arena, E. Gianolio, M. Botta; *J. Biol. Inorg. Chem.* **2013**

24) R. S. Sengar, A. Nigam, S. J. Geib and E. C. Wiener, *Polyhedron*, **2009**, *28*, 1525.

25) E. Gianolio, G. B. Giovenzana, A. Ciampa, S. Lanzardo, D. Imperio and S. Aime, *ChemMedChem*, **2008**, *3*, 60-62.

26) S. Aime, M. Galli, L. Lattuada, M. Morosini, F. Uggeri and R. Kondareddiar, PCT Int. Appl. WO 2006/002873.

27) I. Mamedov, J. Engelmann, O. Eschenko, M. Beyerlein and N. K. Logothetis *Chem. Commun.*, **2012**, *48*, 2755–2757

28) E. M. Elemento, D. Parker, S. Aime, E. Gianolio and L. Lattuada. *Org. Biomol. Chem.*, **2009**, *7*, 1120-1131.

29) Z. Cai and T. A. Kaden, *Helv. Chim. Acta*, **1994**, *77*, 383.

30) X. Zhang, C. A. Chang, H. G. Brittain, J. M. Garrison, J. Telser and M. F. Tweedle, Inorg. Chem., **1992**, *31*, 5597.

31) R. M. Supkowski and W. DeW. Horrocks Jr., *Inorg. Chem.*, **1999**, *38*, 5616.

32) J. I. Bruce, R. S. Dickins, L. J. Govenlock, T. Gunnlaugsson, S. Lopinski, M. P. Lowe, D. Parker, R. D. Peacock, J. J. B. Perry, S. Aime and M. Botta, *J. Am. Chem. Soc*., **2000**, *122*, 9674.

33) A. Riesen, T. A. Kaden, W. Ritter and H. R. Ma¨ cke, *J. Chem. Soc., Chem. Commun.*, **1989**, 460

34) D. A. Moore, *Org. Synth*., **2008**, *85*, 10-14.

35) D. D. Dischino, E. J. Delaney, J. E. Emswiler, G. T. Gaughan, J. S. Prasad, S. K. Srivastava and M. F. Tweedle, *Inorg. Chem*., **1991**, *30*, 1265-1269.

36) A. K. Mishra and J.F. Chatal, *New J. Chem.*, **2001**, *25*, 336.

37) A. K. Mishra, K. Draillard, A. Faivre-Chauvet, J. F. Gestin, C. Curtet and J.-F. Chatal, *Tetrahedron Lett.*, **1996**, *37*, 7515-7518.

38) A. Mishra, J. Pfeuffer, R. Mishra, J. Engelmann, A. K. Mishra, K. Ugurbil and N. K. Logothetis, *Bioconjugate Chem.*, **2006**, *17*, 773.

39) S. Lacerda, M. P. Campello, F. Marques, L. Gano, V. Kubıcek, P. Fouskova, *Dalton Trans*., **2009**, 4509-4518.

40) S. J. Ratnakar and V. Alexander, *Eur. J. Inorg. Chem.*, **2005**, 3918.

41) L. Li, J. Bading, P. J. Yazaki, A. H. Ahuja, D. Crow, D. Colcher, L. E. Williams, J. Y. C. Wong, A. Raubitschek and J. E. Shively, *Bioconjugate Chem.*, **2008**, 19, 89.

42) S. Aime, M. Botta, S. Geninatti Crich, G.B. Giovenzana, G. Palmisano and M. Sisti, *Bioconjugate Chem.*, **1999**, *10*, 192.

43) M. Jauregui, W. S. Perry, C. Allain, L. R. Vidler, M. C. Willis, A. M. Kenwright, J. S. Snaith, G. J. Stasiuk, M. P. Lowe, S. Faulkner. *Dalton Trans.* **2009,** 32, 6283-6285.

44) P. Lebduskova, P. Hermann, L. Helm, E. Toth, J. Kotek, K. Binnemans, J. Rudovsky, I. Lukes, A.E. Merbach. *Dalton Trans.* **2007,** *4*, 493-501.

45) P. Rezanka, V. Kubicek, P. Hermann, I. Lukes. *Synthesis* **2008,** *9*, 1431-1435.

46) J. Rudovsky, J. Kotek, P. Hermann, I. Lukes, V. Mainero, S. Aime. *Organic & Biomolecular Chemistry* **2005**, *3*, 112-117.

47) M. Polasek, M. Sedinova, J. Kotek, L. Vander Elst, R. N. Muller, P. Hermann, I. Lukes. *Inorg. Chem.* **2009**, *48*, 455-465.

48) D. T. Schuehle, M. Polasek, I. Lukes, T. Chauvin, E. Toth, J. Schatz, U. Hanefeld, M.C.A. Stuart, J. A. Peters. *Dalton Trans.* **2010**, *39*, 185-191.

49) L. Frullano, B. Tejerina, T. J. Meade. *Inorg. Chem.* **2006**, *45*, 8489-8491.

50) J. N. Wardle, A. H. Herlihy, P.-W. So, J. D. Bell and S. W. A. Bligh, *Bioorganic & Medicinal Chemistry* **2007** *15* 4714–4721.

51) R. J. Aarons, J. K. Notta, M. M. Meloni, J. Feng, R. Vidyasagar, J. Narvainen, S. Allan, N. Spencer, R. A. Kauppinen, J. S. Snaith, S.A Faulkner. *Chem. Commun.* **2006,** *8*, 909-911.

52) C. Li, P. T. Jr. Winnard, T. Takagi, D, Artemov, Z. M. Bhujwalla. *J. Am. Chem. Soc.* **2006,** *47*, 15072-15073.

53) C. Li, P. Winnard, Z. M. Bhujwalla. *Tetrahedron Lett.* **2009,** *24*, 2929-2931.

54) A. Barge, L. Tei, D. Upadhyaya, F. Fedeli, L. Beltrami, R. Stefania, S. Aime, G. Cravotto. *Org. Biomol. Chem.* **2008,** *7*, 1176-1184.

55) L. S. Natrajan, A. J. L. Villaraza, A. M. Kenwright, S. Faulkner. *Chem. Commun.* **2009,** *40*, 6020-6022.

56) D. Thonon, V. Jacques, J. F. Desreux. *Contrast Media Mol Imag.* **2007,** *1*, 24-34.

57) S. Geninatti Crich, C. Cabella, A. Barge, S. Belfiore, C. Ghirelli, L. Lattuada, S. Lanzardo, A. Mortillaro, L. Tei, M. Visigalli, G. Forni, S. Aime, *J. Med. Chem.* **2006,** *16*, 4926-4936.

58) L. Tei, G. Gugliotta, Z. Baranyai, M. Botta, M. *Dalton Trans.* **2009,** *44*, 9712-9714.

59) D. E. Jr. Prasuhn, R. M. Yeh, A. Obenaus, M. Manchester, M. G. Finn, *Chem. Commun.* **2007,** *12*, 1269-1271

60) R. F. H. Viguier, A. N. Hulme. *J. Am. Chem. Soc.* **2006,** *35*, 11370-11371.

61) M. F. Tweedle, *Eur. Radiol.*, **1997**, *7* (Suppl. 5), S225.

62) K. Kumar, C. A. Chang, L. C. Francesconi, D. D. Dischino, M. F. Malley, J. Z. Gougoutas and M. F. Tweedle. *Inorg. Chem.*, **1994**, *33*, 3567.

63) A. Barge, E, Cappelletti, G. Cravotto, A. Ferrigato, L. Lattuada, F. Marinoni and L. Tei. *Org. Biomol. Chem.*, **2009**, *7*, 3810-3816.

64) C. Gløgard, G. Stensrud and S. Aime. *Magn. Reson. Chem.*, **2003**, *41*, 585-588.

2. Outline of the thesis

The PhD research activity was devoted to develop new efficient preparative accesses to Bifunctional Chelating Agents (BFCAs) and to explore their potential application, with a specific focus on diagnostic imaging applications.

BFCAs embody a metal chelating unit and a reactive functional group. The reactive functional group is used to conjugate the chelating unit to a task-specific molecule, the latter being represented by small organic molecules, biomolecules, macromolecules. The corresponding conjugate retains the metal-chelating ability and allows to use the corresponding metal complex in the devised task. BFCAs are usually prepared through lenghty multistep synthetic sequences: elaborated protection-deprotection strategies are needed in order to manage the large number of functional groups present in this family of molecules. As a result, few BFCAs are commercially available and only in limited amounts and at relatively expensive prices.

The research activity of this PhD was focused on the development of novel BFCAs for lanthanide ions. Lanthanide (Ln^{3+}) metal complexes are widely employed in several diagnostic and therapeutic applications, ranging from the clinically used Gd^{3+}-based MRI contrast agents, to Eu^{3+}-complexes for fluorescent optical imaging, to $^{166}Ho^{3+}$-chelates for SPECT imaging. The importance of the conjugation of these complexes with biomolecules can be easily exemplified by Lutathera®, a clinically approved $^{177}Lu^{3+}$-macrocyclic complex covalently bound to a somatostatin analog (Octreotide®), and used in the treatment of metastatic gastro-entero-pancreatic neuroendocrine tumors.

In the research period, two different activities were carried out and may be summarized as follows:

1) Design and development of original BFCAs for lanthanide metal ions.

In this section, three original BFCAs were designed and synthesized. The BFCAs are derived from ligands commonly employed for the coordination of lanthanide metal ions, namely AAZTA (6-Amino-6-methylperhydro-1,4-diazepine-*N*,*N'*,*N"*,*N"*-tetracetic acid), HP-DO3A (10-(2-hydroxypropyl)-1,4,7,10 tetraaza-cyclododecane-1,4,7-triacetic acid) and DOTAMA (1,4,7,10-tetraazacyclododecane-1,4,7-triacetic acid).

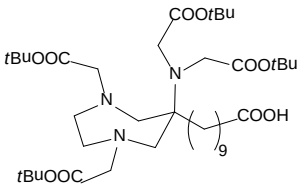

AAZTA-BFCA

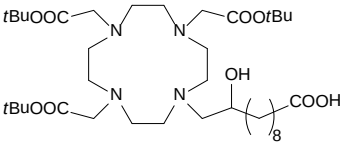

HP-DO$_3$A-BFCA

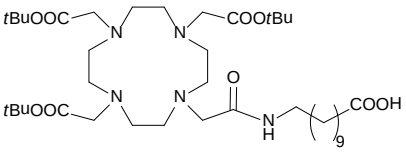

DOTAMA-BFCA

The three cited ligands are formally modified by the introduction of a aliphatic side chain bearing a ω-carboxylic acid, the latter representing the reactive functional groups of the resulting BFCAs.

The syntheses of these BFCAs rely on a common key step involving the selective hydrolysis of a methyl ester in the presence of several *t*-butyl esters. Hydrolytic enzymes were found to be most efficient for this transformation.

2) Conjugation of a novel BFCA to a task-specific molecule and evaluation of the conjugated Gd^{3+}-complexes as MRI contrast agent.

The AAZTA-derived BFCA developed in the previous activity was directly employed for the preparation of a conjugate, where the chelating agent is linked with a task-specific molecule in order to prepare a Gd^{3+}-complex for MRI applications.

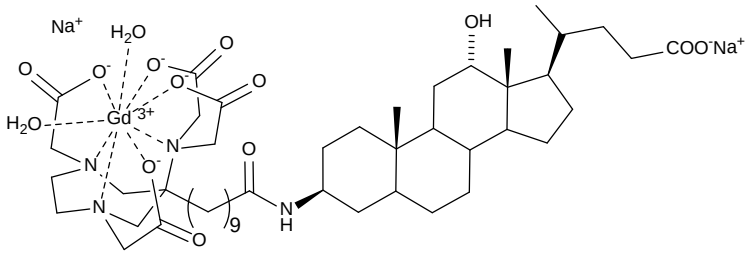

Gd(CN-AAZTA-MADEC)

The reactive functional group of the AAZTA-derived BFCA was used to link a cholic acid derivative, the latter showing a strong affinity with serum albumin. The resulting conjugated ligand was employed for the preparation of a Gd^{3+}-complex with improved diagnostic properties. Indeed, the reversible binding of this conjugate with serum albumin extend the plasmatic half-life of the MRI contrast agent, leading to better images of blood vessels and allowing the accurate determination of vascular parameters.

3. Enzymatic Approach to Bifunctional Chelating Agents

Paolo Minazzi[a,b], Luciano Lattuada*[c], Ivan G. Menegotto[b], Giovanni B. Giovenzana*[a,b].

Submission in progress to *Org. Biomol. Chem.*

Summary

Bifunctional chelating agents (BFCAs) combine the complexing properties of a multidentate ligand with the presence of a free reactive functional group, mainly devoted to conjugation purposes. BFCAs are generally prepared through multi-step syntheses and with extensive application of protection-deprotection strategies, due to the large number of functional groups involved. Hydrolytic enzymes, with their exquisite chemoselectivity, provived the best results in the preparation of three different BFCAs based on well known ligand platforms.

Introduction

Metal complexes are widely used in diagnostic and therapeutic applications. Paramagnetic complexes of Gd(III) are routinely used in clinical MRI,[1] while chelates of radioactive metal ions represent the active imaging agents in PET and SPECT,[2] or therapeutic agent in radiotherapy.[3] In addition, different luminescent complexes are employed in Optical Imaging.[4] The thermodynamic and kinetic stabilities of metal complexes in biological conditions is challenged through a careful design/choice of the ligand structure, satisfying the metal requirements for a stable coordination. In addition, the structure of metal complexes needs to be modified for different application-related purposes such as: i) introduction of lipophilic/ hydrophilic residue to modulate solubility properties and/or to promote the inclusion in different formulations ii) targeting to a specific biologic target through conjugation to specific vectors (small molecules, proteins or peptides,

antibodies ecc.)

BiFuctional Chelating Agents (BFCA) combine the complexing properties of a multidentate ligand with the presence of a free reactive functional group, devoted to conjugation or tailoring purposes. Several BFCAs are commercially available, although their number is still limited if the wide variety of metal ions to be used is taken into account. BFCAs are generally prepared through multi-step synthesis and with extensive application to protection-deprotection strategies, due to the large number of fuctional groups involved.[5,6]

In this article we describe the preparation of three selected BFCAs (Scheme 1) through a chemoenzymatic approach. The exquisite chemoselectivity of hydrolytic enzymes is engaged to handle the significant number of functional groups of selected polyaminopolycarboxylic ligands. The choice of the ligand platforms falls on three chelating agents usually employed for lanthanide ions, mainly because Ln^{III} ions are extensively used in different imaging/therapeutic techniques and due to our experience in the development of ligand platforms for Ln^{III} ions.[7,8] All BFCAs share a remote carboxylic acid group, protected as a methyl ester during the synthesis and selectively removed by chemical or enzymatic hydrolysis.

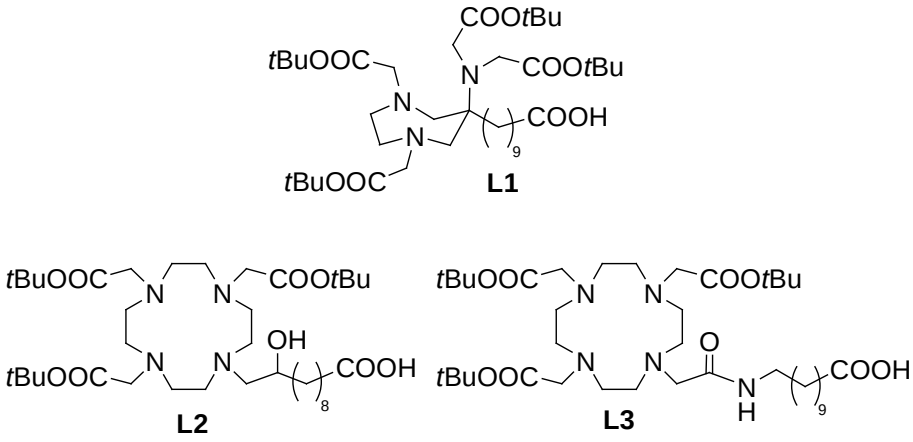

Scheme 1. BFCAs prepared in this work.

The first BFCA (**L1**) is a derivative of the heptadentate ligand AAZTA (6-Amino-6-methylperhydro-1,4-diazepine-*N,N',N",N"*-tetraacetic acid).[9] Starting from the first report of the formation of a promising Gd(III)-complex for MRI application, AAZTA rapidly gained popularity, with several derivatives reported to date and continuous efforts devoted to the development of bifunctional derivatives.[10-13]

The second BFCA (**L2**) is a derivative of the macrocyclic ligand HP-DO3A, best known for its Gd-complex actually employed in clinical MRI as contrast agent under the brand name ProHance and used with other lanthanide ions for the development of CEST-MRI imaging procedures.[14] The same macrocyclic 12-membered ring is at the base of the third BFCA (**L3**), built on the base structure of DOTA-monoamides (DOTA = 1,4,7,10-tetraazacyclododecane-1,4,7,10-tetraacetic acid), the latter widely represented in several of the above cited applications.

Results and discussion

Synthesis of protected BFCA's agent

Bifunctional derivatives of AAZTA usually bear the reactive functional groups on the carbon atom carrying the primary amine group (position 6 of the 6-aminoperhydro-1,4-diazepine ring). This is due either to an easier synthetic access, as in the original synthesis this carbon atom derives from a suitable nitroalkane, or to stereochemical and steric considerations, as substituents placed in this position: i) retain the symmetry plane of the ligands, ii) circumvent the generation of stereocenters as would happen in any other ring or pendant arm position, iii) avoid any steric influence on the metal coordination sphere.

The first BFCA **L1** was obtained introducing on the AAZTA skeleton a C_9-alkyl spacer with a terminal carboxylic acid functional group.

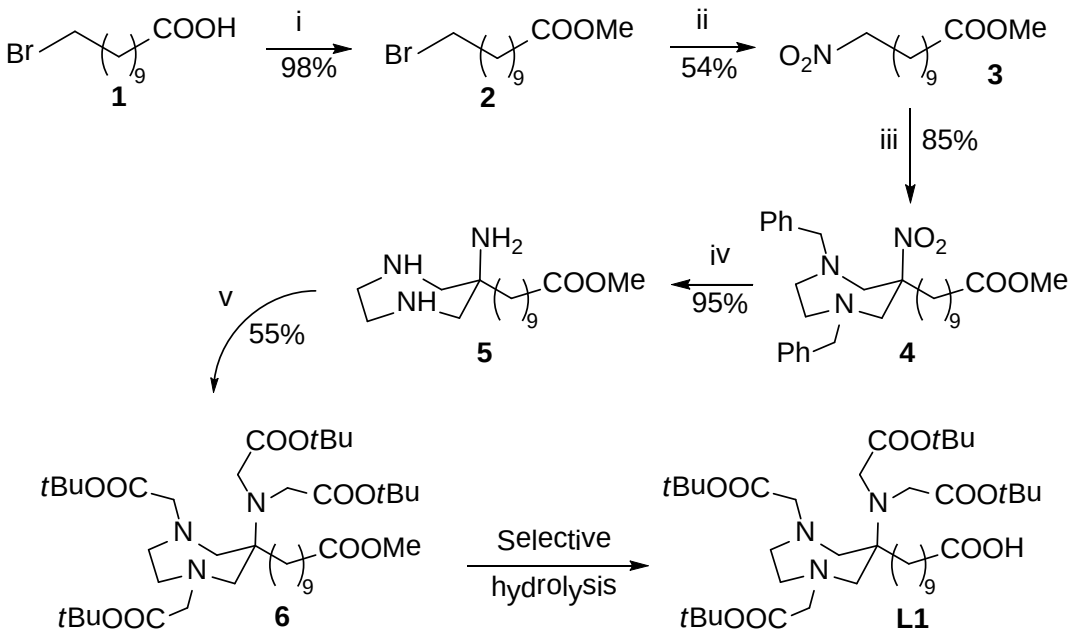

Scheme 2 Synthesis of **L1**. Reagents and conditions: (i) $SOCl_2$, MeOH, r.t.; (ii) $NaNO_2$, Urea, DMAc, 50°C, 24h; (iii) *N*,*N*-Dibenzylethylenediamine diacetate, $(CH_2O)_n$, PhMe/EtOH, Rfx; (iv) $HCOONH_4$, Pd/C 10%, MeOH, Rfx; (v) $BrCH_2COOtBu$, K_2CO_3, CH_3CN.

The preparation of **L1** is depicted in Scheme 2 and starts from ω-bromoundecanoic acid **1**. The carboxylic group is protected as methyl ester **2**, then the halogen atom is substituted with a nitro group through a S_N2 reaction with sodium nitrite in *N*,*N*-dimethylacetamide in the presence of urea. The ω-nitroester **3** is used in the ring formation step, taking place through a double nitro-Mannich reaction with *N*,*N'*-dibenzylethylenediamine and paraformaldehyde. Catalytic transfer hydrogenation with ammonium formate and Pd/C allowed the combined removal of the benzyl groups located on the endocyclic nitrogen atoms and the reduction of the nitro group, leading to the triaminoester **5**. The amine groups were exhaustively alkylated with *tert*-butyl bromoacetate in acetonitrile in the presence of finely

powdered potassium carbonate, giving after chromatographic purification the mixed ester **6**, the latter representing the direct precursor of the BFCA **L1**.

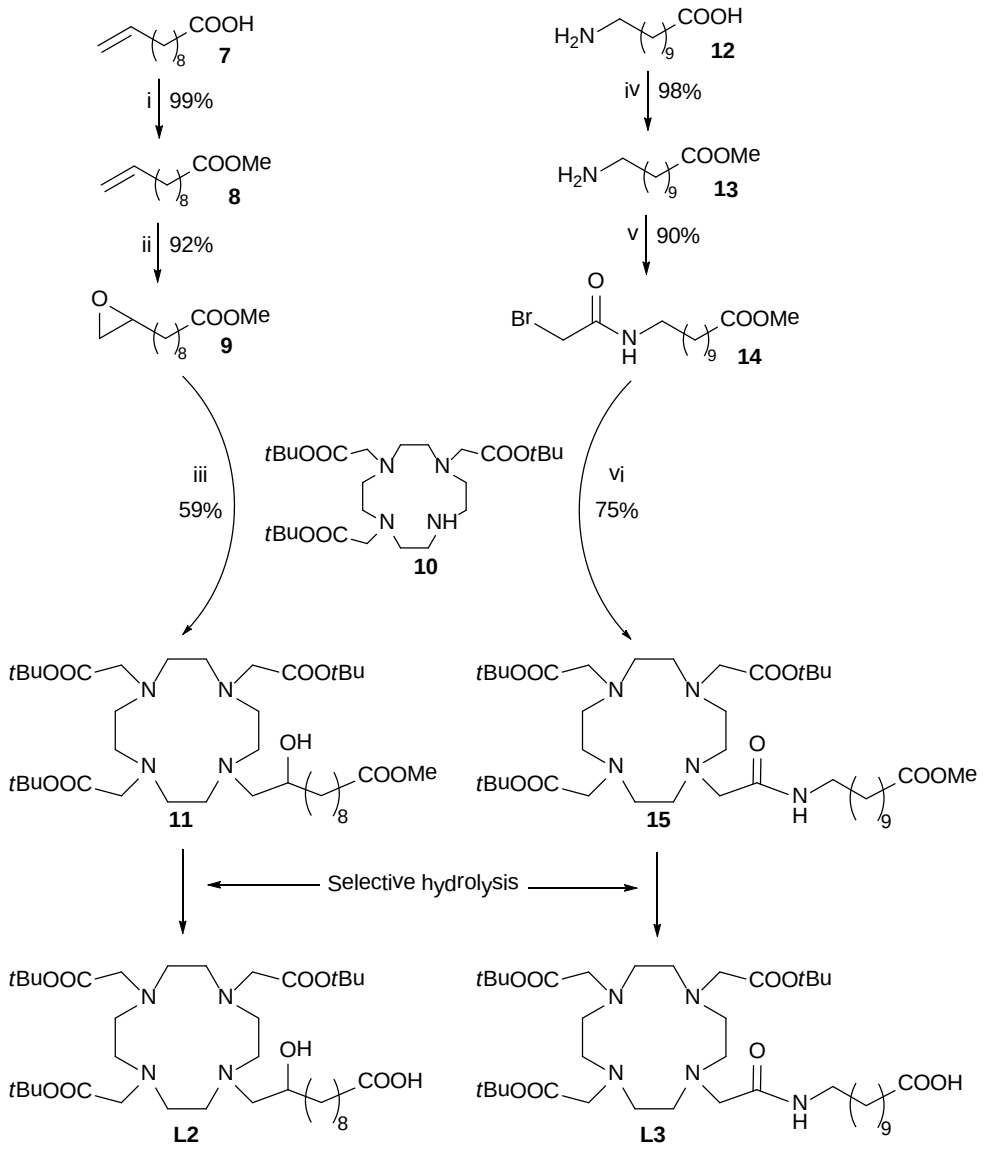

Scheme 3 Synthesis of **L2** and **L3**. Reagents and conditions; (i) $SOCl_2$, MeOH; (ii) MCPBA, CH_2Cl_2; (iii) $BrCH_2COBr$, K_2CO_3, CH_2Cl_2/H_2O; (iv) DMAc, TEA; (v) CH_3CN, TEA.

The syntheses of the macrocyclic BFCAs is reported in Scheme 3; their preparation relies on a common synthetic precursor, *i.e.*: DO3A-tBu$_3$ (1,4,7,10-tetraazacyclododecane-1,4,7-triacetate tri-*t*-butyl ester), either commercially available or conveniently prepared through literature procedure[15] and differing only in the preparation and installation of the side arms.
The preparation of the HP-DO3A-derived BFCA **L2** requires the alkylation of the secondary amine group of DO3A-tBu$_3$ with the epoxyester **9**, obtained in two steps from 10-undecenoic acid, to give the mixed ester precursor **11**.
The side arm of the DOTAMA (DOTA MonoAmide) BFCA **L3** was prepared by esterification of 11-aminoundecanoic acid followed by *N*-bromoacetylation in Schotten-Baumann conditions to give the alkylating intermediate **14**. Reaction of the latter with DO3A-tBu$_3$ in acetonitrile in the presence of potassium carbonate provided the mixed ester precursor **15**.

The first step in each compounds were the protection of carboxylic acid moieties by methyl ester group **8-11**. Compound **8** was treated with MCPBA to give the corrispondig epoxide **9**, alkylation of DO$_3$A was carried out using triethylamine as a base to obtain the compound **15**. Compound **12** was prepared by the alkylation with bromoacethybromide and the final alkylation of DO$_3$A with compound **12**, was carried out following the procedure of compound **15**, to afford the compound **16**.

Selective hydrolysis

The protected BFCAs described in the previous section share the presence of carboxylic groups protected with different ester moieties, namely *t*-butyl ester on the carboxylic groups involved in metal coordination and methyl ester on the carboxylic acid intended for conjugation purposes.
In principle, methyl ester can be selectively cleaved in the presence of *t*-butyl esters

by a judicious choice of hydrolytic conditions. Nevertheless, a similar example of a mixed ester of DOTA[16] highlighted the difficulties in finding conditions that avoid side-reactions as hydrolysis of *t*-butyl esters and transesterification (when alcohols are used as (co)solvents) on these specific substrates.

Compounds **6**,**15**,**16** are then subjected to an extensive screening aimed at individuating optimal experimental conditions leading to the BFCAs **L1-L3** in preparatively useful yields. In this work "classical" chemical hydrolysis was complemented and compared with enzymatic methods. The exquisite chemoselectivity of hydrolytic enzymes can be useful to obtain the desired selectivity in the removal of the methyl ester groups.[17] To the best of our knowledge, only one report of the use of hydrolytic enzymes on ethyl esters of chelating agents esters can be found in the literature,[18] but the extreme similarity of the homogenously esterified carboxyl group led either to incomplete reactions or to poor yields with macrocyclic substrates. Our substrates offer better conditions for the operativity of enzymes, presenting a single methyl ester located at the end of an aliphatic chain, strongly resembling the chemical environment of fatty acid esters.

The screening of "chemical" hydrolysis includes two different hydroxides (LiOH, NaOH), an alkaline carbonate and an alkaline bicarbonate, sharing the same mixed solvent system 2-propanol/water 1:1. The screening of enzymes involves three lipases, *i.e.:* PPL, CCL and an immobilized CAL (Lipase B Candida Antarctica on immobead 150, recombinant from *Aspergillus oryzae*), all of them run in a mixed solvent system MTBE/phosphate buffer (KH_2PO_4/K_2HPO_4, 1M, pH 7.5). The corresponding results are summarized in Table 1.

	6 → L1		15 → L2		16 → L3	
	Time (h)	**Yield (%)[a]**	**Time (h)**	**Yield (%)[a]**	**Time (h)**	**Yield (%)[a]**
NaOH	4	91*	4	92*	6	89*
LiOH	4	90*	8	90*	6	88*
K_2CO_3	>48	0	>48	0	>48	0
$NaHCO_3$	>48	0	>48	0	>48	0
PPL	36	97	36	98	48	94
CCL	>48	0	48	87	48	63
CAL	4	99	4	99	5	98

[a] Isolated yields, corrected by ^{1}H-NMR with internal standard (diphenylmethane).

Table 1: Reaction times yields and conversion of different ligands. (*ligand found as a complex).

The results of Table 1 show that potassium carbonate and sodium bicarbonate are completely ineffective with all substrates even after 48h. Better results are obtained with alkaline hydroxides, with nearly complete conversion after 4-8h, depending on the substrate, with the AAZTA precursor reacting generally faster than the macrocyclic derivatives. It is noteworthy that in these runs, the products of the hydrolysis are unavoidably plagued by the presence of variable amounts of the alkaline cation, strongly retained in the macrocyclic cavity, a phenomenon well known for DO3A and DOTA derivatives.[19] Small amount of byproducts arising from the unwanted hydrolysis of *t*-butyl groups, can be detected in the crude reaction mixture, too.

The use of enzyme leads to different results. PPL provided clean reactions with all three substrates, reaching completion after 36-48h and with nearly quantitative yields. Lower performances were shown with CCL, where good results were obtained with substrate **15** after 48 h, while an incomplete conversion was obtained

with the cognate ester **16** and no reaction at all was observed with the AAZTA derivative **6**.

Gratifyingly and quite unexpectedly, the best results are obtained with supported CAL: conversion was complete in 4-5 h with the three BFCA precursors, and nearly quantitative yields are obtained from a simpler workup. No evidence of the hydrolysis byproducts observed with NaOH and LiOH can be found in the reaction mixtures, leading on easy workup, even more facilitated by the heterogeneous nature of the catalyst, and finally to higher isolated yields.

According to all these considerations, supported CAL in phosphate buffer/MTBE proved to be the best combination for the selective removal of methyl esters of mixed ester precursors of AAZTA-, HP-DO3A and DOTAMA-based BFCA. The latter are currently in use for the preparation of conjugates, to be reported elsewhere.

Conclusions

The preparation of BFCAs usually requires multi-step synthetic approaches and complex protection-deprotection strategies. In this work, the synthesis of three different BFCAs, based on the AAZTA, HP-DO3A and DOTAMA ligands is reported. The efficiency and selectivity of enzymes (lipases) are successfully employed for the multigram preparation of these BFCAs, with the key step represented by the selective removal of a methyl ester group in the presence of multiple *t*-butyl ester groups. The enzymatic protocol is preferred to chemical hydrolysis, where alkaline hydroxides can reach comparable hydrolytic activities but with the drawback represented by the formation of unwanted byproducts. Supported CAL proved to be the most active enzyme with respect to these specific substrates.

Experimental section

General remark

All chemicals reagents are obtained from Aldrich or Alfa-Aesar and used without further purification. ^{1}H-NMR and ^{13}C-NMR spectra are registered on a Jeol Eclipse ECP300 spectrometer at 300 MHz and 75.4 MHz, respectively. Mass spectra are performed on a ThermoFinningan LCQ-Deca XP-PLUS, operating in ESI-MS mode.

Synthetic procedures

Methyl 11-Bromoundecanoate (2). 11-Bromoundecanoic acid (1, 38.0 g, 0.14 mol) is dissolved in 200 mL of methanol and thionyl chloride (16 mL, 0.21 mol) is slowly dropped into the reaction mixture, kept in a ice bath. After the addition the resulting solution is refluxed for 2 hours, then cooled and a solution of potassium carbonate 20% is added until pH>9. The methanol is removed under vacuum and the aqueous suspension extracted twice with dichloromethane. The organic extracts are dried over Na_2SO_4, filtered and evaporated yielding 2 as a light brown oil. (38.20 g, 98%). ^{1}H NMR (300 MHz, $CDCl_3$) δ (ppm): 1.26 (s, 10H, CH_2), 1.39 (bquint, J = 6.9 Hz, 2H, CH_2), 1.58 (bquint, J = 7.0 Hz, 2H, CH_2), 1.82 (quint, J = 6.9 Hz, 2H, CH_2), 2.27 (t, J = 7.5 Hz, 2H, CH_2), 3.37 (t, J = 6.9 Hz, 2H, CH_2), 3.63 (s, 3H, CH_3). ^{13}C {1H} NMR (75.4 MHz, $CDCl_3$) δ (ppm): 24.9 (*C*H_2), 28.1 (*C*H_2), 28.7 (*C*H_2), 29.1 (*C*H_2), 29.2 (*C*H_2), 29.3 (*C*H_2), 29.4 (*C*H_2), 32.8, (*C*H_2), 33.9 (*C*H_2), 34.1 (*C*H_2), 51.4 (*C*H_3), 174.2 (*C*). MS (ESI+) calculated for: $[C_{12}H_{23}BrO_2+H]^+$ 279.09-281.09, found 279.16-281.15.

Methyl 11-Nitroundecanoate (3). Methyl ester **2** (38.17 g, 0,14 mol) is dissolved in 50 mL of *N*,*N*-dimethylacetamide and to this solution pholoroglucinol (22.05 g, 0.14 mol) and sodium nitrite (18.88 g, 0.27 mol) are sequentially added. The reaction mixture is heated at 50 °C for 24 hours. The mixture is then cooled and

extracted 3 times with petroleum ether and the upper phase collected and evaporated under vacuum. The crude product is purified by silica gel column chromatography (95/5 petroleum ether/ethyl acetate) to obtain **3** as a light yellow oil (18.1 g, 54%).^{1}H NMR (300 MHz, $CDCl_3$) δ (ppm): 1.27-1.32 (m, 12H, CH_2), 1.60 (bquint, J = 7.2 Hz, 2H, CH_2), 1.99 (quint, J = 7.2 Hz, 2H, CH_2), 2.29 (t, J = 7.5 Hz, 2H, CH_2), 3.68 (s, 3H, CH_3), 4.36 (t, 2H, CH_2). ^{13}C {1H} NMR (75 MHz, $CDCl_3$) δ (ppm): 24.9 (*C*H_2), 26.2 (*C*H_2), 27.4 (*C*H_2), 28.8 (*C*H_2), 29.1 (*C*H_2), 29.2 (*C*H_2), 29.3 (*C*H_2), 34,1 (*C*H_2), 51.4 (*C*H_3), 75.8 (*C*H_2), 51.4 (*C*H_2), 174.3 (*C*). MS (ESI+) calculated for : $[C_{12}H_{23}NO_4+H]^+$ 246.32, found 246.12.

Compound 4. A mixture of the nitroester **3** (18.0 g, 0.07 mol) and *N*,*N*-dibenzylethylendiamine diacetate (31.7 g, 0.09 mol) in 1/1 toluene/ethanol (300 mL) is brought to reflux with magnetic stirring until a clear solution was obtained. Paraformaldeyde (8.4 g, 0.28 mol) is then added in a single portion and heating was continued for additional 5 hours. The solvent is removed under vacuum and the residue purified by silica gel column chromatography (95/5 petroleum ether/ethyl acetate) to obtain compound **4** as a yellow light oil (30.2 g, 85%). ^{1}H NMR (300 MHz, $CDCl_3$) δ (ppm): 0.69-1.32 (m, 14H, CH_2), 1.60 (bquint, J = 7.2 Hz, 2H, CH_2), 1.59 (bquint, 2H, CH_2), 2.29 (t, J = 7.5 Hz, 2H, CH_2), 2.51-2.65 (m, 4H, (CH_2), 2.95 (d, J = 14.1 Hz, 2H, CH_2), 3.50 (d, J = 14.1 Hz, 2H, CH_2), 3.57 (d, J = 12.9 Hz, 2H, CH_2), 3.66 (s, 3H, CH_3) 3.72 (d, J = 13.1 Hz, 2H, CH_2), 7.19-7.37 (m, 10H, Ar*H*). ^{13}C {1H} NMR (75 MHz, $CDCl_3$) δ (ppm): 23.1, 25.0, 29.2, 29.3, 29.33 29.34 (*C*H_2), 34.17 (*C*H_2), 37.1 (*C*H_2), 51.4 (*C*H_3), 58.8 (*C*H_2), 61.9 (*C*H_2), 64.1 (*C*H_2), 95.2 (*C*), 127.3, 128.3, 129.2, 139.3 (*C*H), 174.4 (*C*). MS (ESI+) calculated for: $[C_{30}H_{43}N_3O_4+H]^+$ 510.33, found 510.15.

Compound 5. Compound **4** (30.0 g, 0.059 mol) is dissolved in methanol (150 mL), and 10% Pd/C (3.0 g) is added under N_2 atmosphere. Ammonium formate (36.1 g, 0.60 mol) is added in small portion, and the reaction heated to 60°C for 2h. The catalyst is removed by filtration through Celite® and the solvent removed under

reduced pressure. The crude product is redissolved in dichloromethane and repeatedly washed with a 1M NaOH solution and (25 mL x 4). The organic phase is dried over Na_2SO_4, and evaporated to obtain the triaminoester **5** as a light yellow oil (17.05 g, 95%). ^{1}H NMR (300 MHz, $CDCl_3$) δ (ppm): 1.23 (bs, 14H, CH_2), 1.57 (bt, J = 6.7 Hz, 2H, CH_2), 2.56 (t, J = 7.5 Hz, 2H, CH_2), 2.70 (m, 4H, CH_2), 2.75-3.01 (m, 4H, CH_2), 3.62 (s, 3H, CH_3). ^{13}C {1H} NMR (75 MHz, $CDCl_3$) δ (ppm): 24,9 29.1, 29.2, 29.35, 29.36 30.3 (*C*H_2), 34.0 (*C*H_2), 39.4 (*C*H_2), 51.0 (*C*H_2), 51.4 (*C*H_3), 56.4 (*C*), 59.6 (*C*H_2), 174.3 (*C*). MS (ESI+) calculated for : **[**$C_{16}H_{33}N_3O_2$+H]$^+$ 300.17, found 300.5.

Compound 6. In a mixture of the triamine **5** (17.0 g, 0.056 mol) and potassium carbonate (46.45 g, 0.34 mol) in acetonitrile, *t*-butyl bromoacetate (41 mL, 0.28 mol) is added dropwise. The reaction is stirred at room temperature overnight. The inorganic salts are removed by filtration on a Buchner funnel and the solvent removed under reduced pressure. The crude product is purified by silica gel column chromatography to obtain the mixed ester **6** as a light yellow oil. (23.4 g, 55%). ^{1}H NMR (300 MHz, $CDCl_3$) δ (ppm): 1.22-1.30 (m, 14H, CH_2), 1.426 (s, 18H, (CH_3), 1.432 (s, 18H, (CH_3) 1.60 (m, 2H, CH_2), 2.28 (t, J = 7.5 Hz, 2H, CH_2), 2.62 (d, 2H, J = 14.4 Hz, (CH_2), 2.621-2.68 (m, 2H, CH_2), 2.72-2.80 (m, 2H, CH_2), 2.98 (d, 2H, J = 14.1 Hz, (CH_2), 3.22 (bs, 4H, CH_2), 3.62 (bs, 4H, CH_2), 3.65 (s, 3H, CH_3). ^{13}C {1H} NMR (75 MHz, $CDCl_3$) δ (ppm): 22.1 (*C*H_2), 25.0, (*C*H_2), 28.2 (*C*H_3) 28.3 (*C*H_3), 29.2, 29.3, 29.6, 30.5 (*C*H_2), 34.14 (*C*H_2), 37.6 (*C*H_2), 51.4 (*C*H_3), 51.9 (*C*H_2), 59.4 (*C*H_2), 62.6 (*C*H_2), 63.1 (*C*), (*C*H_2), 65.4 (*C*H_2), 80.2, (*C*), 80.7 (*C*), 170.9 (*C*), 172.9 (*C*), 174.3 (*C*). MS (ESI+) calculated for : **[**$C_{40}H_{73}N_3O_{10}$+H]$^+$ 756.32, found 756.5.

Methyl 10-Undecenoate (8). 10-Undecenoic acid (16.0 g, 0.087 mol) is suspended in methanol (50 mL) and thionyl chloride (8.9 mL, 0.12 mol) is added dropwise (external ice bath for cooling is required to maintain T<10°C). The resulting solution is stirred at room temperature for 12 hours. A solution of aq. 20%

potassium carbonate is added until pH>9, then methanol is evaporated under vacuum and the crude product extracted thrice with ethyl acetate (3x25mL). The combined organic extracts are dried over Na_2SO_4, filtered and evaporated yielding compound **8** as a light brown oil. (17.2 g, 99%).^{1}H NMR (300 MHz, $CDCl_3$) δ (ppm): 1.22-1.41 (m, 10H, C*H*$_2$), 1.61 (quint, J = 7.0 Hz, 2H, C*H*$_2$), 2.05 (quart, J = 6.7 Hz, 2H, C*H*$_2$), 2.29 (t, J = 7.5 Hz, 2H, C*H*$_2$), 3.65 (s, 3H, C*H*$_3$), 4.90-5.01 (m, 2H, C*H*$_2$), 5.79 (ddt, , J_1 = 6.9 Hz, , J_2 = 9.9 Hz, , J_3 = 17.1 Hz, 1H, C*H*). ^{13}C {1H} NMR (75 MHz, $CDCl_3$) δ (ppm): 24.9, 28.1, 29.1, 29.17, 29.2, 29.4, 33.8, 34.1 (*C*H$_2$), 51.4 (*C*H$_3$), 114.2 (*C*H$_2$), 139.2 (*C*H), 174.2 (*C*). MS (ESI+) calculated for : $[C_{12}H_{22}O_2+H]^+$ 199.16, found 199.30.

Compound 9. Methyl 10-undecenoate **8** (2.0 g, 0.010 mol) is dissolved in 20 mL of CH_2Cl_2 and 3-chloroperbenzoic acid (70%, 2.45 g, 0.010 mol) is added. The reaction is stirred at room temperature for for 3 hours. A white solid forms and is removed by filtration on a Buchner funnel. The filtrate is thoroughly washed with a 5% aq. NaOH solution. The organic phase is dried over Na_2SO_4, filtered and evaporated to obtain **9** as a colourless oil. (2.11 g, 92%). ^{1}H NMR (300 MHz, $CDCl_3$) δ (ppm): 1.22-1.62 (m, 16H, C*H*$_2$), 2.28 (t, J = 7.5 Hz, 2H, C*H*$_2$), 2.44 (dd, J_1 = 5.1 Hz, J_2 = 2.6 Hz, 1H, C*H*$_2$), 2.44 (dd, J_1 = 5.0 Hz, J_2 = 3.9 Hz, 1H, C*H*$_2$), 2.87 (m, 1H, C*H*), 3.64 (s, 3H, C*H*$_3$). ^{13}C {1H} NMR (75 MHz, $CDCl_3$) δ (ppm): 24.97, 25.9, 29.2, 29.4, 29.5, 32.5, 34.1 (*C*H$_2$), 47.13 (*C*H$_2$) 51.5 (*C*H$_3$), 52.39 (*C*H) 174.3 (*C*). MS (ESI+) calculated for: $[C_{12}H_{22}O_3+H]^+$ 214.1, found 214.06.

Compound 11. Triester **10** (1.0 g, 0.0019 mol) and the epoxyester **9** (447 mg, 0.0021 mol) are dissolved in *N*,*N*-dimethylacetamide (5.0 mL) and the solution is refluxed for 36 hours. The reaction mixture is diluted with CH_2Cl_2 (20 mL), washed with H_2O (4 x 20 mL) and brine (3 x20 mL), dried (Na_2SO_4), filtered and evaporated under vacuum. The crude product is purified by silica gel column chromatography (eluent CH_2Cl_2/MeOH/NH_3 95/5/0.5) to obtain the mixed ester 15 as a light brown oil. (820 mg, 59%). ^{1}H NMR (300 MHz, $CDCl_3$) δ (ppm): 1.25-

1.34 (m, 12H, C*H*$_2$), 1.43 (s, 18H, (C*H*$_3$), 1.44 (s, 9H, C*H*$_3$), 1.59 (quint. J= 7.1 Hz, 2H, CH$_2$), 2.04-3.49 (br, 26 H, C*H*$_2$), 2.27 (t, J = 7.5 Hz, 2H, C*H*$_2$), 3.64 (s, 3H, C*H*$_3$). ^{13}C {1H} NMR (75 MHz, CDCl$_3$) δ (ppm): 24.9 (CH$_2$) 25.8 (CH$_2$), 27.9 (CH$_3$), 28.2 (CH$_3$), 29.1, 29.4, 29.8 34.1, 34.8 (*C*H$_2$), 51.4 (*C*H$_3$) 51.8 (*C*H$_2$), 52.1 (*C*H$_2$), 52.3 (*C*H$_2$), 53.7 (*C*H$_2$), 55.9 (*C*H$_2$), 56.8 (*C*H$_2$), 61.5 (*C*H$_2$), 68.1 (*C*H), 80.7 (*C*), 80.8 (*C*), 170.9 (*C*), 171.1 (*C*), 174.1 (*C*). MS (ESI+) calculated for : [C$_{38}$H$_{72}$N$_4$O$_9$+Na]$^+$ 751.52, found 751.01.

Methyl 11-Aminoundecanoate (13). 11-Aminoundecanoic acid (5.0 g, 0.025 mol) is suspended in methanol (25 mL) and then thionyl chloride (3.6 mL, 0.05 mol) is added dropwise (external ice bath for cooling is required to maintain T<10°C). The mixture is stirred at room temperature for 12 hours. A solution of aq. 20% potassium carbonate is added until pH>9, then methanol is evaporated under vacuum and the crude product is extracted with ethyl acetate (3x25mL), the organic phase dried (Na$_2$SO$_4$) and filtered. Removal of the solvent yielded the ester **11** as a light brown oil. (5.3 g, 98%). ^{1}H NMR (300 MHz, CDCl$_3$) δ (ppm): 1.21-1.38 (m, 12H, C*H*$_2$), 1.55 (bquint, J = 7.02 Hz, 2H, C*H*$_2$), 1.68 (bquint, J = 7.1 Hz, 2H, C*H*$_2$), 2.26 (t, J = 7.5 Hz, 2H, C*H*$_2$), 2.9 (quart, J = 6.6 Hz, 2H, C*H*$_2$), 3.63 (s, 3H, C*H*)$_3$ 7.25 (bs, 2H, N*H*$_2$). ^{13}C {1H} NMR (75 MHz, CDCl$_3$) δ (ppm): 24.9, 26.6, 28.2, 29.1, 29.2, 29.25, 29.4, 34.1, 40.2 (*C*H$_2$), 51.5 (*C*H$_3$), 174.4 (*C*). MS (ESI+) calculated for : [C$_{12}$H$_{25}$NO$_2$+H]$^+$ 216.19, found 216.10.

Compound 14. Ester **13** (5.2 g, 0.024 mol) is added to a biphasic mixture of CH$_2$Cl$_2$ (25 mL) and an aqueous solution containing potassium carbonate (13.2 g, 0.096 mol, in 25 mL). Bromoacetyl bromide (3.1 mL, 0.036 mol) is added dropwise into the vigorously stirred biphasic mixture and the reaction run for 2 hours. The two phases are separated and the organic layer washed with water (3x25mL) and brine (25 mL). The solvent is evaporated under reduced pressure to obtain the amidoester **12** as a light brown waxy solid. (7.3 g, 90%). ^{1}H NMR (300 MHz, CDCl$_3$) δ (ppm): 1.18-1.36 (m, 12H, C*H*$_2$), 1.52 (bquint, J = 7.02 Hz, 2H,

C*H*$_2$), 1.60 (bquint, J = 7.3 Hz, 2H, C*H*$_2$), 2.29 (t, J = 7.4 Hz, 2H, C*H*$_2$), 3.27 (quart, J = 6.6 Hz, 2H, C*H*$_2$), 3.65 (s, 3H, C*H*$_3$), 3.88 (s, 2H, C*H*$_2$) 6.51 (bs, 1H, N*H*). ^{13}C {1H} NMR (75 MHz, $CDCl_3$) δ (ppm): 24.9, 26.8, 29.1, 29.2, 29.27, 29.3, 34.1, 40.3 (*C*H$_2$), 51.4 (*C*H$_3$), 165.5.2 (*C*), 174.4 (*C*). MS (ESI+) calculated for : $[C_{14}H_{26}BrNO_3+H]^+$ 336.11-338.11, found 336.02-338.03.

Compound 15. The triester **10** (2.0 g, 3.8 mmol) and the bromoacetamide **14** (1.43 g, 4.3 mmol) are dissolved in acetonitrile (25 mL) and to the resulting mixture triethylamine (749 µL, 5.7 mmol) is added. The mixture is refluxed for 36 hours. The solvent was removed under vacuum and the oily residue taken up in dichloromethane (25 mL), washed with H_2O (4x20 mL) and brine (3x20 mL), dried (Na_2SO_4), filtered and evaporated under vacuum**.** The crude product was purified by silica gel column chromatography (eluent CH_2Cl_2/MeOH/NH_3 95/5/0.5) to obtain the BFCA precursor **16** as a light brown oil. (2.2, 75%). ^{1}H NMR (300 MHz, $CDCl_3$) δ (ppm): 1.11-1.27 (m, 16H, C*H*$_2$), 1.33 (s, 9H, (C*H*$_3$), 1.34 (s, 18H, C*H*$_3$), 1.46 (quint. J= 7.2 Hz, 2H, CH_2) 2.18 (t, J = 7.5 Hz, 2H, C*H*$_2$), 2.40-3.34 (br, 24H, C*H*$_2$), 3.54 (s, 3H, C*H*$_3$) 8.67 (m, 1H, N*H*). ^{13}C {1H} NMR (75 MHz, $CDCl_3$) δ (ppm): 24.9 (CH_2) 25.8 (CH_2), 27.9 (CH_3), 28.0 (CH_3), 28.1, 28.2 29.2 29.5, 39.4 (*C*H$_2$), 50.6 (*C*H$_3$) 52.6 (*C*H$_2$), 53.28 (*C*H$_2$), 53.3 (*C*H$_2$), 55.7 (*C*H$_2$), 55.8 (*C*H$_2$), 56.6 (*C*H$_2$), 81.7 (*C*), 81.8 (*C*), 169.8 (*C*), 170.0 (*C*), 171.4 (*C*) 172.4 (*C*). MS (ESI+) calculated for : **[**$C_{40}H_{75}N_5O_9$+Na]$^+$ 792.56, found 792.05.

General procedure for chemical hydrolyses. Methyl ester (**6**, **15**, **16**, 200 mg) is dissolved in a 2-propanol/water (1:1, 10.0 mL). The alkaline bicarbonate/carbonate/hydroxide (1.5 eq) is added in a single portion and the reaction stirred at room temperature for the reported time (Table 4). 2-Propanol is then evaporated under reduced pressure and the aqueous phase is washed with CH_2Cl_2 (3x5 mL). The organic solvent is dried (Na_2SO_4), filtered and evaporated under vacuum to give the corresponding BFCA.

General procedure for enzymatic hydrolyses. Methyl ester (**6**, **15**, **16**, 200 mg) is added to a suspension of lipase (60 mg,) in a mixture of 2.0 mL of phosphate buffer (1M, pH 7.5) and 8 mL of methyl *t*-butyl ether. The reaction mixture is stirred at room temperature for the reported time (Table 4). The lipase is removed by filtration on a Celite®, the filtrate concentrated and the aqueous phase extracted with CH_2Cl_2 (3x5 mL). The organic solvent is dried (Na_2SO_4), filtered and evaporated under vacuum to give the corresponding BFCA.

Ligand 1. ^{1}H NMR (300 MHz, $CDCl_3$) δ (ppm): 1.22-1.30 (m, 14H, C*H*$_2$), 1.41 (s, 18H, (C*H*$_3$), 1.42 (s, 18H, (C*H*$_3$) 1.60 (m, 2H, C*H*$_2$), 2.31 (t, J = 7.5 Hz, 2H, C*H*$_2$), 2.62 (d, 2H, J = 14.1 Hz, (C*H*$_2$), 2.62-2.68 (m, 2H, C*H*$_2$), 2.72-2.80 (m, 2H, C*H*$_2$), 2.98 (d, 2H, J = 14.4 Hz, (C*H*$_2$), 3.22 (bs, 4H, C*H*$_2$), 3.61 (bs, 4H, C*H*$_2$). ^{13}C {1H} NMR (75 MHz, $CDCl_3$) δ (ppm): 22.0 (*C*H$_2$), 24.7, (*C*H$_2$), 28.2 (*C*H$_3$) 28.3 (*C*H$_3$), 29.0, 29.2, 29.4, 30.4 (*C*H$_2$), 34.1 (*C*H$_2$), 37.6 (*C*H$_2$), 51.9 (*C*H$_2$), 59.3 (*C*H$_2$), 62.5 (*C*H$_2$), 63.0 (*C*), (*C*H$_2$), 65.4 (*C*H$_2$), 80.3, (*C*), 80.8 (*C*), 170.9 (*C*), 173.0 (*C*), 179.0 (*C*). MS (ESI+) calculated for : **[**$C_{39}H_{71}N_3O_{10}$+H]$^+$ 742.51, found 742.78.

Ligand 2. ^{1}H NMR (300 MHz, $CDCl_3$) δ (ppm): 1.18-1.31 (m, 14H, C*H*$_2$), 1.40 (s, 9H, (C*H*$_3$), 1.41 (s, 18H, (C*H*$_3$), 1.55 (quint. J= 7.1 Hz, 2H, CH_2) 2.21 (t, J = 7.35 Hz, 2H, C*H*$_2$), 2.67-2.80 (m, 10H, C*H*$_2$), 2.88 (m, 8H, C*H*$_2$), 3.01-3.15 (m, 1H, C*H*), 3.25 (s, 4H C*H*$_2$), 3.29-3.37 (m, 2H C*H*$_2$). ^{13}C {1H} NMR (75 MHz, $CDCl_3$) δ (ppm): 25.3(CH_2) 25.7 (CH_2), 27.9 (CH_3), 28.2 (CH_3), 29.1, 29.2, 29.8 34.9, 36.4 (*C*H$_2$), 49.6 (*C*H$_2$), 51.2 (*C*H$_2$), 52.8 (*C*H$_2$), 53.1 (*C*H$_2$), 56.1 (*C*H$_2$), 56.5 (*C*H$_2$), 59.7 (*C*H$_2$), 65.8 (*C*H), 81.2 (*C*), 81.4 (*C*), 170.6 (*C*), 170.8 (*C*), 178.7 (*C*). MS (ESI+) calculated for : [$C_{37}H_{70}N_4O_9$+Na]$^+$ 737.53, found 737.70.

Ligand 3. ^{1}H NMR (300 MHz, $CDCl_3$) δ (ppm): 1.18-1.35 (m, 16H, C*H*$_2$), 1.44 (s, 9H, (C*H*$_3$), 145 (s, 18H, C*H*$_3$), 1.6 (quint. J= 7.2 Hz, 2H, CH_2) 2.18 (t, J = 7.5 Hz, 2H, C*H*$_2$), 2.75-2.88 (br, 18H, C*H*$_2$), 3.20-3.31 (m, 6H, C*H*$_2$). ^{13}C {1H} NMR (75 MHz, $CDCl_3$) δ (ppm): 25.2 (CH_2) 26.9 (CH_2), 28.0 (CH_3), 28.2 (CH_3), 29.1,

29.2 29.3 29.6, 28.7, 34.9, 39.5 (*C*H_2), 50.6 (*C*H_3) 52.6 (*C*H_2), 53.28 (*C*H_2), 53.3 (*C*H_2), 55.7 (*C*H_2), 55.8 (*C*H_2), 56.6 (*C*H_2), 80.7 (*C*), 81.8 (*C*), 169.9 (*C*), 170.0 (*C*), 170.4 (*C*) 177.3 (*C*). MS (ESI+) calculated for : **[**$C_{39}H_{73}N_5O_9$+Na]$^+$ 778.54, found 778.60.

Notes and references

[a] *Dipartimento di Scienze del Farmaco, Università degli Studi del Piemonte Orientale "A. Avogadro", Largo Donegani 2/3, 28100 Novara, Italy. Fax: ++39-(0)321-375621; Tel:++ 39-(0)321-375846; E-mail:giovenzana@pharm.unipmn.it*
[b] *CAGE Chemicals srl, Via Bovio 6, 28100 Novara, Italy*
[c] *Bracco Imaging SpA, Bracco Research Centre, Via Ribes 5, 10010 Colleretto Giacosa (TO), Italy*

[1] a) R. B. Lauffer, *Chem. Rev.* **1987**, *87*, 901-927; b) P. Caravan, J. J. Ellison, T. J. McMurry, R. B. Lauffer, *Chem. Rev.* **1999**, *99*, 2293-2352; c) P. Herrmann, J. Kotek, V. Kubíček, I. Lukeš, *Dalton Trans*. **2008**, 3027-3047.

[2] a) S.M. Ametamey, M. Honer, P.A. Schubiger, *Chem. Rev.*, **2008**, *108*, 1501-1516. b) H. Herzog, F. Rösch, *Pharm. Unserer Zeit*, **2005**, *34*, 468-473.

[3] a) E.W. Price, C. Orvig, *Chem. Soc. Rev.* **2014**, *43*, 260-290. b) W.A. Volkert, T.J. Hoffman, *Chem. Rev*. **1999**, *99*, 2269-2292.

[4] V. Ntziachristos, *Ann. Rev. Biomed. Eng*., **2006**, *8*, 1-33.

[5] L. Lattuada, A. Barge, G. Cravotto, G.B. Giovenzana, L. Tei, *Chem. Soc. Rev.*, **2011**, *40*, 3019-3049.

[6] L. Frullano, P. Caravan, *Curr. Org. Synth.*, **2011**, *8*, 535-565.

[7] Z. Baranyai, F. Uggeri, G.B. Giovenzana, A. Bényei, E. Brücher, S. Aime, *Chem. Eur. J*. **2009**, *15*(7), 1696-1705.

[8] Z. Baranyai, M. Botta, M. Fekete, G.B. Giovenzana, R. Negri, L. Tei, *Chem. Eur. J*. **2012**, *18*, 7680-7685.

[9] S. Aime, L. Calabi, C. Cavallotti, E. Gianolio, G.B. Giovenzana, P. Losi, A. Maiocchi, G. Palmisano, M. Sisti, *Inorg. Chem.*, **2004**, *43*, 7588-7590.

[10] I. Mamedov, J. Engelmann, O. Eschenko, M. Beyerlein, N.K. Logothetis, *Chem. Commun.*, **2012**, *48*, 2755-2757.

[11] G. Gugliotta, M. Botta, G.B. Giovenzana, L. Tei, Bioorg. *Med. Chem. Lett*., **2009**, *19*, 3442-3444.

[12] R.S. Sengar, A. Nigam, S.J. Geib, E.C. Wiener, *Polyhedron*, **2009**, *28*, 1525-1531.

[13] R. Artali, G. Bombieri, G.B. Giovenzana, M. Galli, L. Lattuada, F. Meneghetti, *Inorg. Chim. Acta*, **2013**, *407*, 306-312.

[14] D. Delli Castelli, E. Terreno, S. Aime, *Angew. Chem. Int. Ed.*, **2011**, *50*, 1798-1800.

[15] D. A. Moore, *Org. Synth.* **2008**, *85*, 10-14.

[16] C. Li, P. Winnard Jr., Z.M. Bhujwalla, *Tetrahedron Lett.*, **2009**, *50*, 2929-2931.

[17] G.M. Whitesides, C.H. Wong, *Enzymes in Synthetic Organic Chemistry, Pergamon, Oxford*, **1994**.

[18] E. Burks, N. Koshti, H. Jacobs, A. Gopalan, *Synlett*, **1998**, 1285-1287.

[19] K. Kumar, C.A. Chang, L.C. Francesconi, D.D. Dischino, M.F. Malley, J.Z. Gougoutas, M.F.Tweedle, *Inorg. Chem.* **1994**, *33*, 3567-3575.

4. Gd(CN-AAZTA-MADEC), an excellent agent for DCE-MRI studies on mice on 1T scanners

F. Arena, D. L. Longo, L. Consolino, E. Gianolio, P. Minazzi, G. B. Giovenzana and S. Aime.

Submitting to *Molecular Imaging and Biology*

Introduction

The advent of MI era has witnessed the introduction of MRI scanners operating at lower magnetic field strength than the complex (and expensive) systems that are found in the specialized MRS/MRI labs dedicated to "*in vivo* "studies. The need for seeing MRI as one of the complementary imaging techniques for multi-model studies has stimulated manufactory companies to consider the possibility of offering scanners based on permanent- or electro-magnets and characterized by a user-friendly, imaging acquisition made. It is expected that the availability of this new generation of MRI scanners[1] will be a key-components together with compact PET/SPECT and Optical Imaging instruments of the "*in vivo*" Molecular Imaging Lab that will support many biology departments based on mice studies.

In this context it appears quite reasonable that MRI scanners will be exploited also in the Dynamic Contrast Enhancement (DCE)[2,3] modality as the last 25 years of MRI clinic studies has clearly demonstrated the important results may be obtained by the use of paramagnetic Gd-complexes. It is well established that the efficiency of a Gd(III) complex to enhance the relaxation rate of water proton depends on the structure of the complex, on the strength of the applied magnetic field and on the interactions the complex may present with molecular components of its microenvironment[4].

Two key applications of Gd-based contrast agents appears of general applicability in the MRI study of mice models namely the visualization of the blood vessel network[5] and the assessment of vascular permeability in the tumor regions[6,7]. The best results for both applications have been obtained by using a Gd(III) complex able to reversibly bind to Serum Albumin. The formation of supramolecular adducts between the paramagnetic complex and the serum protein has beneficial effects both on the attainable relaxation enhancement (particularly high at 0.5-1.5 T)[8] and on the "*in vivo*" distribution properties.

This work compares the efficiency of three Gd-albumin binding contrast agents (two well established and one 'ad hoc' synthetized) as blood pool agents and as vascular permeability agent reporters on a MRI scanner operating at 1T.

Methods

Chemistry: Commercially available reagents and solvents were purchased from Sigma-Aldrich or Alfa-Aesar and used without further purification. **B22956/1**[9] was obtained by Bracco Imaging spa. Reactions were monitored by TLC on Merck 60F254 (0.25 mm) plates. Spot detection was carried out by staining with an alkaline $KMnO_4$ solution or with the Dragendorff reagent. NMR spectra were recorded at 298K on a Jeol Eclipse ECP300 spectrometer operating at 7.05 T; chemical shifts (d) are given in ppm, coupling constants (J) in Hz. ESI mass spectra were recorded on ThermoFinnigan LCQ Deca XP-Plus and melting points (uncorrected) with a Stuart Scientific SMP3 apparatus.

Conjugate 3-*t*Bu$_4$-Me: Compound **1** (14.0 g, 18.9 mmol) and methyl 3-aminodeoxycholate (**2**, 8.50 g, 21.0 mmol) were dissolved in dichloromethane (100 mL). *N*,*N*'-Dicyclohexylcarbodiimide (4.9 g, 23.7 mmol) and 4-dimethylaminopyridine (0.46 g, 3.8 mmol) were added to the solution and sttirred at room temperature overnight. The white solid precipitate was removed by

filtration on a Buchner funnel and the filtrate evaporated under reduce pressure. The residue was submitted to chromatographic purification, obtaining the desired product as a white solid (13.6 g, 64%). M.p. 70°C. 1H NMR ($CDCl_3$, 300 MHz): δ = 5.73 (d, J = 7.4 Hz, 1H), 4.11 (m, 1H), 3.92 (m, 1H), 3.60 (s, 3H), 3.57 (s, 4H), 3.17 (s, 4H), 2.93 (d, J = 14.1 Hz, 2H), 2.76-2.54 (m, 4H), 2.58 (d, J = 14.1 Hz, 2H), 2.36-0.95 (m, 43H), 1.385 (s, 18H), 1.382 (s, 18H), 0.91 (d, J = 6.4 Hz, 3H), 0.90 (s, 3H), 0.62 (s, 3H); 13C NMR ($CDCl_3$, 75.4 MHz): δ = 174.7 [C], 172.9 [2xC], 172.3 [C], 170.9 [2xC], 80.7 [2xC], 80.2 [2xC], 73.0 [CH], 65.4 [CH_2], 63.1 [C], 62.6 [CH_2], 59.3 [CH_2], 52.0 [CH_2], 51.5 [CH_3], 48.9 [CH], 48.3 [CH], 47.3 [CH], 46.5 [C], 45.1 [CH_2], 38.1 [CH], 37.6 [CH_2], 37.1 [CH_2], 35.9 [CH], 35.1 [CH], 34.7 [CH_2], 34.0 [CH_2], 33.0 [CH], 31.2 [CH_2], 31.1 [CH_2], 31.0 [CH_2], 30.6 [CH_2], 30.5 [CH_2], 29.7 [CH_2], 29.6 [CH_2], 29.4 [CH_2], 29.3 [CH_2], 29.0 [CH_2], 28.3 [6xCH_3], 28.2 [6xCH_3], 27.5 [CH_2], 26.7 [CH_2], 25.9 [2xCH_2], 25.7 [CH_2], 25.0 [CH_2], 24.8 [CH_2], 23.9 [CH/CH_3], 23.7 [CH_2], 22.1 [CH_2], 17.4 [CH_3], 12.8 [CH_2]; MS (ESI+): m/z calcd for $C_{64}H_{113}N_4O_{12}$ $[M+H]^+$: 1129.84; found: 1129.93.

Compound 3: Compound **3-*t*Bu4-Me** (13.5 g, 12.0 mmol) was dissolved in a mixture of 2-propanol (100 mL) and a solution of sodium hydroxide (1.23 g) in deionized water (370 mL). The reaction mixture was stirred at room temperature for 48h, then evaporated under reduce pressure. The residue was redissolved in dichloromethane (20 mL) and trifluoroacetic acid (25 mL) was added, stirring the resulting mixture at room temperature overnight. Volatiles were evaporated and the residue triturated and washed with acetone (50 mL), obtaining ligand **L1** (10.5 g, 98%). Mp 210-212.5 °C. 1H NMR (DMSO-d_6, 300 MHz): δ = 7.35 (d, J = 6.7 Hz, 1H), 3.97 (m, 1H), 3.80 (m, 1H), 3.63 (s, 4H), 3.53 (s, 4H), 3.11-2.93 (m, 4H), 3.03 (d, J = 14.7 Hz, 2H), 2.98 (d, J = 14.7 Hz, 2H), 2.29-0.87 (m, H), 2.10 (t, J = 7.2 Hz, 2H), 0.94 (d, J = 6.4 Hz, 3H), 0.91 (s, 3H), 0.63 (s, 3H). 13C NMR (DMSO-d_6, 75.4 MHz): δ = 175.2 [C], 175.1 [2xC], 172.3 [C], 171.0 [2xC], 71.9 [CH], 63.1

[C], 61.9 [CH_2], 59.8 [CH_2], 55.7 [CH_2], 52.3 [CH_2], 48.3 [CH], 48.1 [CH], 47.0 [CH], 46.8 [C/CH_2], 45.1 [CH], 37.2 [CH], 36.3 [C/CH_2], 36.2 [CH], 36.0 [CH], 35.4 [CH], 34.8 [CH_2], 33.8 [CH_2], 33.1 [CH], 31.6 [CH_2], 31.4 [CH_2], 31.13 [CH_2], 31.06 [CH_2], 30.3 [C/CH_2], 29.5 [CH_2], 29.4 [2xCH_2], 29.3 [CH_2], 29.2 [CH_2], 27.6 [CH_2], 27.1 [CH_2], 26.3 [CH_2], 26.0 [CH_2], 25.9 [CH_2], 25.1 [CH_2], 24.9 [CH_2], 24.0 [CH_2], 23.8 [CH_3], 23.0 [CH_2], 17.6 [CH_3], 13.0 [CH_3]; MS (ESI): m/z calcd for $C_{47}H_{77}N_4O_{12}$ $[M\text{-}H^+]^-$: 889.55; found: 889.65.

Gd-(3): compound **3** (9.0 mmol) was suspended in deionized water (30 mL) and freshly prepared $Gd(OH)_3$ (9.0 mmol) was added. The opalescent suspension was stirred at 80°C until complete solution was obtained (~32h), periodically checking the presence of free Gd(III) with Xylenol Orange. The solution was then filtered on 0.25 μm filters and evaporated under reduced pressure. The crude product was redissolved in deionized water (10 mL) and precipitated with acetone (50 mL) (3 times), then the solid was dried under vacuum to constant weight to obtain **Gd-L1** as a white powder (7.0 g).

Water proton relaxivity measurements: The longitudinal water proton relaxation rates were measured by using a Stelar Spinmaster (Mede, Pavia, Italy) spectrometer operating at 0.47 T by the standard inversion-recovery technique (16 experiments, 2 scans). A typical 90° pulse width was 3.5 ms and the reproducibility of the T_1 data was ±0.5%. The temperature was controlled with a Stelar VTC-91 air-flow heater equipped with a copper/constantan thermocouple (uncertainty ±0.1°C). The proton $1/T_1$ NMRD profiles were measured over a continuum of magnetic field strength from 0.00024 to 0.47 T (corresponding to a 0.01–20 MHz proton Larmor frequency) on a Stelar field-cycling relaxometer. The relaxometer operates under complete computer control with an absolute uncertainty in $1/T_1$ of ±1%. Data points from 0.47 (20 MHz) to 1.7 T (70 MHz) were collected on a Stelar Spinmaster spectrometer operating at variable fields.

^{17}O measurement: Variable-temperature ^{17}O NMR measurements were recorded with a Bruker Avance 14T spectrometer equipped with a 5 mm probe using a D_2O external lock. Experimental settings were as follows: spectral width 9000 Hz, 90° pulse width (14 μs), acquisition time 10 ms, 1024 scans and no sample spinning. Solutions containing 2.6% of the ^{17}O isotope (Yeda, Israel) were used. The observed transverse relaxation rates (R^0_{2obs}) were calculated from the signal width at half-height ($\Delta\nu 1/2$):

$$R^0_{2obs}=\pi\Delta\nu 1/2$$

Binding to HSA: Binding parameters (the affinity constant K_A, the number of equivalent and independent binding sites n and the relaxivity of supramolecular adduct r_1^b were determined using the proton relaxation enhancement (PRE) method. The method is based on the titration of a fixed concentration of Gd-complex with increasing concentrations of macromolecule that results in an increase of relaxation rate. The fitting of the obtained curve afford the value of K_A and r_1^b.

Pharmacokinetic Study: Plasma pharmacokinetics were assessed on male Balb/C mice (18-20 g; Charles River Laboratories, Calco, Italy). The animals were cared for under an approved protocol and the guidelines of our University Animal Care and Use Committee. A group of three mice were used for each contrast agent. The mice were anesthetized with an intraperitoneal injection of a mixture of ketamine (Bedford, OH, 90 mg/kg) and xylazine (St. Joseph, MO, 10 mg/kg). A heparinized catheter was inserted into the tail vein for administration of the contrast agent and blood sampling. The contrast agent was injected at a dose of 0.05 mmol Gd/kg body weight (b.w.). Blood samples (50-100 μL) were collected from the catheter before injection and at 5, 30,60, 120, 360 min after injection for a total of six time points. The blood samples were centrifuged at 10,000 rpm at 4°C for 10 min to

obtain plasma. The plasma was diluted with sterile water (Baxter) and the Gd content was determined by ICP-OES. A two-compartment pharmacokinetic model was used to analyze the data and calculate the pharmacokinetic parameters such as distribution and elimination half-lives ($T_{d1/2}$, $T_{e1/2}$) from the percentages of the initial blood concentration C_0 with GraphPad Prism software (GraphPad, San Diego, CA, USA).

Magnetic Resonance Angiography: A group of three male BALB/c mice weighing approximately 20 grams were used in contrast enhanced MR blood pool imaging for each agent. Mice were anesthetized by injecting a mixture of tiletamine/zolazepam (Zoletil 100; Virbac, Milan, Italy) 20 mg/kg and xylazine (Rompun; Bayer, Milan, Italy) 5 mg/kg and placed supine in a solenoid Tx/Rx coil with an inner diameter of 3.5 cm. The contrast agents were injected via a tail vein at a dose of 0.05 mmol Gd/kg.

MR images were acquired before and at 2, 5, 15, 30, 45 and 60 min post-injection of the contrast agents on a 1T MRI Bruker Icon^{TM} system (Bruker BioSpin MRI, Ettlingen, Germany). A 35 mm TX/RX mouse solenoid whole body coil was used for both RF excitation and for MR signal reception. A 3D GRE fast low angle shot (FLASH) pulse sequence (TR 10 ms; TE 4.1 ms; flip angle 40°; FOV 80x40x40 mm; MTX 192x156x156; NEX 2; temporal resolution 3 min 4 s per image) with an isotropic spatial resolution of 416 µm was used for image acquisition. Three dimensional maximum intensity projection (MIP) images were reconstructed using the ImageJ program (http://rsb.info.nih.gov/ij/) by subtracting pre-contrast to post-contrast images.

DCE-MRI in mice tumor model: The B16 human melanoma cancer cell line was cultured in DMEM medium with 2 mM L-glutamine and 10% FBS at 37°C in a humidified atmosphere of 5% CO_2. The cells were allowed to grow to about 90% confluence and then resuspended in DMEM medium. The cell number was

adjusted to 10^6 cells/ml containing approximately $2.0x10^5$cells in 0.2 ml, were implanted subcutaneously in the flanks of C57/Bl6 mice. Each implantation generated a tumor. Tumor size reached 0.5–1.0 cm in diameter 10-20 days after cell implantation.

Magnetic resonance images were acquired on anesthetized mice with an Aspect M2 MRI System (Aspect Magnet Technologies Ltd., Netanya, Israel) working at 1 Tesla. Mice were anesthetized by injecting a mixture of tiletamine/zolazepam (Zoletil 100; Virbac, Milan, Italy) 20 mg/kg and xylazine (Rompun; Bayer, Milan, Italy) 5 mg/kg and placed supine in a solenoid Tx/Rx coil with an inner diameter of 3.5 cm. Breath rate was monitored throughout in vivo MRI experiments using a respiratory probe (SAII Instruments, Stony Brook, NY - USA). A phantom filled with diluted ProHance® (Bracco Imaging SpA, Milan, Italy) was included in the field of view (FOV), close to each animal, to allow correction for changes in the instrument performance. After the scout image acquisition, a T_2-weighted (T_{2w}) anatomical image was acquired with a Fast Spin Echo sequence (TR 2500 s; TE 41 ms; number of slices 10; slice thickness 1.5 mm; FOV 40 mm; matrix 128 × 128; four averages; acquisition time 2 m 40 s).

DCE–MRI was performed using an axial 2D T_{1w} spoiled gradient echo sequence (TR 40 ms; TE 1.8 ms; flip angle 60°; number of slices 10; slice thickness 1.5 mm; FOV 40 mm; matrix 128 × 128; one acquisition; temporal resolution 58 s per image) with dynamic series was acquired with three initial pre-contrast T1w images and 47 dynamic post-contrast images for a total examination time of 50 min. The contrast agents were injected intravenously at a dose of 0.05 and 0.025 mmol Gd/kg. Three mice were used in each experimental group for each dose and for each blood-pool contrast agents.

MR images were evaluated using in-house written software developed in Matlab (MathWorks, Natick, MA) and signal intensities (SI) of tumor, muscle and artery was measured in source images by drawing corresponding ROIs to evaluate SI enhancement following contrast agent injection. Studies were approved by the local

ethics committee of our University and carried out in accordance with the EU guidelines. All animals were maintained under specific pathogen-free conditions inside the animal facility and received standard rodent chow and had free access to tap water.

Results and Discussion

Figure 1 reports the chemical structure of the three Gd(III) agents used in this work, namely MS-325 (Vasovist® or Ablavar®)[11] (**1**), B22956/1(**2**)[10] and Gd(CN-AAZTA-MADEC) (**3**). The synthesis and the characterization of (**1**) and (**2**) were already reported. The third paramagnetic complex Gd-(**3**) is an original derivative of the ligand AAZTA (=1,4-bis(carboxymethyl)-6-[bis(carboxymethyl)]-amino-6-methyl-1,4-diazepane)[12] recently reported to show a good compromise between a higher metal hydration and a good thermodynamic and an excellent kinetic stability with lanthanides metal ions.[13] The AAZTA ligand is formed by seven-member ring with two endocyclic and one exocyclic nitrogen atoms and four carboxymethyl side arms, representing an novel intermediate family between the open chain DTPA and the macrocyclic DOTA ligand. Gd-(AAZTA) shows a relaxivity value 65-70% higher than the congeners Gd-DTPA and Gd-DOTA, chiefly ascribed to the presence of the two rapidly exchanging coordinated water molecules (q = 2). Lipophilic derivatives of Gd-AAZTA where used to form non-covalent conjugates with serum albumin (HSA),[14] reaching remarkably high relaxivity values, and with lipoproteins (HDL),[15] (LDL),[16] taking advantages of their uptake for tumor cells visualization. In Gd-(**3**) the Gd-AAZTA substructure is linked to the aminodeoxycholic residue through an amide bond but with a longer spacer, represented by a C9 aliphatic chain. Gd(CN-AAZTA-MADEC) has been properly designed for the attainment of high relaxation enhancement at magnetic field around 1T.

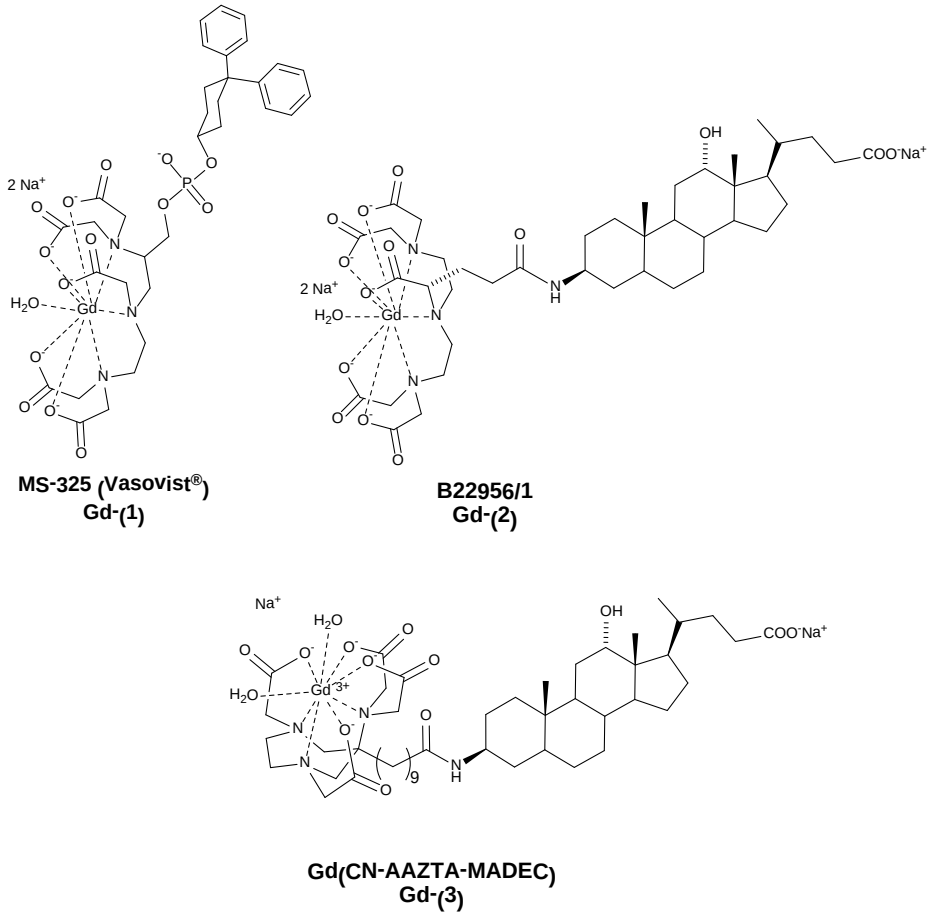

MS-325 (Vasovist®)
Gd-(1)

B22956/1
Gd-(2)

Gd(CN-AAZTA-MADEC)
Gd-(3)

Figure 1

Synthesis: The synthesis of Gd-**L1** is reported in Scheme 1 and starts from the protected bifunctional derivative **1**,[17] recently prepared through a chemo-enzymatic approach, and from the methyl ester of 3-aminodeoxycholic acid, the latter prepared from deoxycholic acid according to a procedure reported by Anelli *et al.*[18]

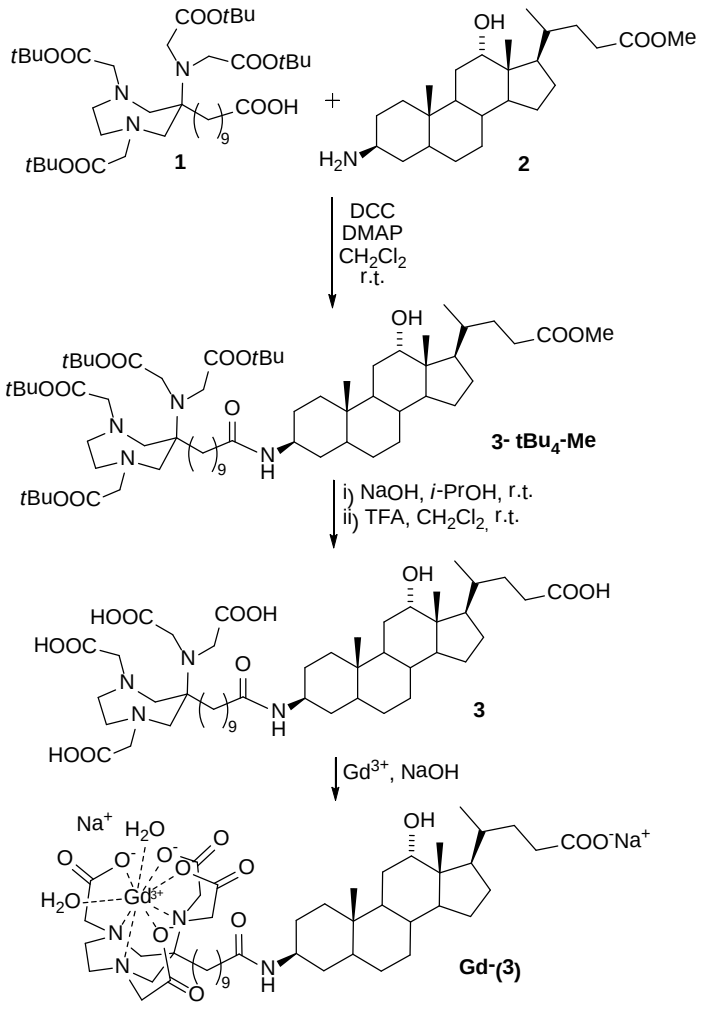

Scheme 1. Synthesis of Gd-**L1**.

Standard amide coupling between **1** and **2** using DCC/DMAP in dichloromethane yields the protected conjugate **3-*t*Bu$_4$-Me**; removal of the methyl ester and *t*-butyl ester groups is best obtained by a sequential combination of a mild alkaline hydrolysis (to avoid fission of the amide bond) followed by trifluoroacetic acid in dichloromethane, both performed at room temperature. The ligand **L1** obtained is then reacted with freshly prepared $Gd(OH)_3$ to give the desired chelate Gd-**L1**.

Relaxometric characterization of Gd complex: The complexation of the Gd^{III} ion to the ligand CN-AAZTA-MADEC (**3**) was carried out by adding a stoichiometric amount of $GdCl_3$ to the aqueous solution of the ligand at pH 7 and at room temperature. The presence of the aliphatic chain between the heptadentate ligand AAZTA and the deoxycholic acid moiety affects the relaxation enhancement properties of the Gd-(**3**). The presence of the aliphatic chain induces the formation of self assembled aggregates above the millimolar concentration (**Figure 2**).

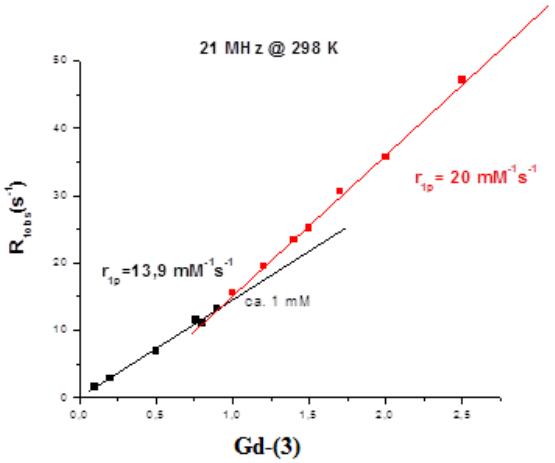

Figure 2: Plot of variation of the observed longitudinal proton relaxation rate as a function of concentration of Gd-(**3**) at 21 MHz and 25 °C.

The critical micellar concentration (cmc) of the system was conveniently determined by measuring the ^1H relaxation rate as a function of the Gd^{III} complex concentration. In general, titration of a ligand solution with Gd^{III} ions leads to the formation of a paramagnetic complex; and a straight line for the relaxivity versus Gd^{III} complex concentration plot is obtained [Eq.(1)], whose angular coefficient corresponds to the relaxivity (r_{1p}) of the complex, where R_{1w} is the diamagnetic contribution of pure water (0.38 s^{-1}).

$$R_{1obs} = [\text{Gd-L}]\, r_{1p} + R_{1w} \qquad (1)$$

In the case of Gd-(**3**) the sharp variation of the linear slope is observed when the system passes from monomeric state to micellar or self assembling systems. From the data reported in Figure 2, a cmc value of 1 mM was determined.

At 20 MHz and 298K, the relaxivity of the Gd-(**3**) below the cmc is 13.9 $mM^{-1}s^{-1}$, whereas the relaxivity of the self assembled structure above the cmc is 20 $mM^{-1}s^{-1}$. The relaxivity of the non assembled form is about 35% higher than that of Gd-(**2**), as a consequence of the increasing in the molecular weight for the introduction of the relatively long aliphatic chain, as well as the introduction of the heptadentate ligand AAZTA with an inner-sphere water coordination number of 2.

From the analysis of the temperature dependence of the transverse relaxation rate of the metal-bound ^{17}O water resonance (Figure 3) we obtained a τ_M values of 100 ns, a value that is similar than that reported for the parental complex Gd-AAZTA (90 ns)[12] and for known Gd-(**2**) (120 ns), in the optimal range for the attainment of the high relaxivity in the presence of long molecular reorientational times.[19]

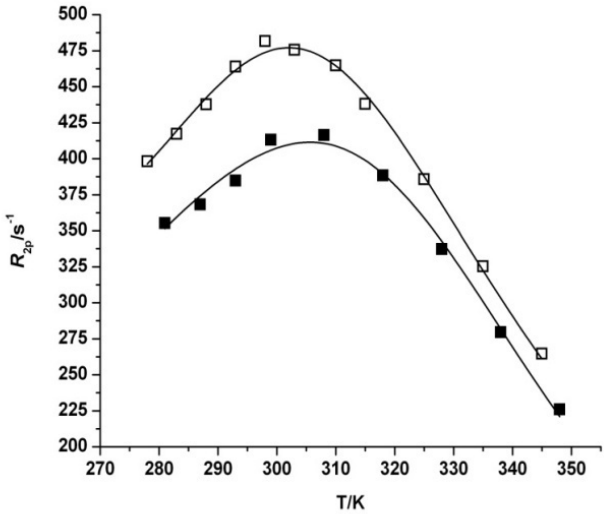

Figure 3: Temperature dependence of the transverse ^{17}O water relaxation rate (R_{2p}) for 8.8 mM solution of Gd-AAZTA (□) and Gd-(**3**) (■) at 15 T and neutral pH

The effect of the aggregation may be evaluated by analyzing the profile of the relaxivity data as a function of the applied field strength. The resulting plot of $r_1$versus the Proton Larmor Frequency, named NMRD profile, for monomeric and aggregated systems measured at 298K and neutral pH is reported in Figure 4. Experimental data points were fitted on the basis of the Solomon-Bløмbergen-Morgan[20] (for the inner sphere contribution) and Freed[21] (for the outer sphere contribution) theories. Some fitting parameters were fixed to reasonable values: q and τ_M to the values obtained by ^{17}O-NMR R_{2p} analysis, $r_{Gd\text{-}H}$ (distance for the inner-sphere water molecules) to 3.14 Å, d (distance of minimum approach between solvent and solute molecules) to 3.8 Å, and D (water diffusion constant) to $2.2\cdot10^{-5}$ cm^2s^{-1}. The obtained values for τ_R, Δ^2 [square of the mean transient zero-field splitting(ZFS) energy], τ_V (correlation time for the collision- related modulation of the ZFS Hamiltonian) are reported in **Table 1** and compared to those reported for the analogous Gd-AAZTA complex and to those of Gd-(**2**). The introduction of the deoxycholic acid moiety in the DTPA derivative and in the heptacoordinated Gd-AAZTA derivative increases the molecular weight of the two systems, leading to a doubling of the reorientational correlation time value (τ_R). The aggregation of the complex additionally contributes to give a system with a slower molecular tumbling relative to the monomeric complex. The τ_R value reflects the increase in the size of the system due to the aggregation that involves the presence of 4-5 second sphere water molecules as a contribution to the NMRD profile of the Gd-(**3**) aggregate.

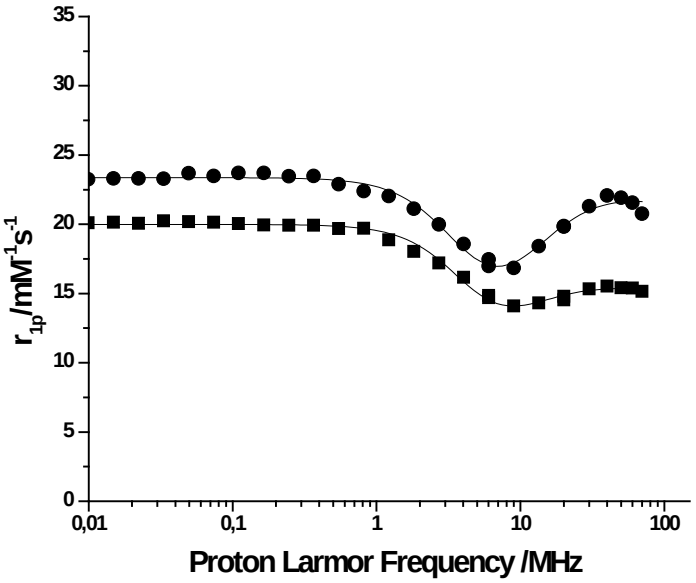

Figure 4: $1/T_1$ NMRD profile of 1 mM solution of Gd-(**3**), aggregated (●) and monomer (■) measured at 25°C. The solid curves through the data points were calculated using the parameters reported in Table 1.

Contrast Agent	r_{1p} (20 MHz) [$mM^{-1}S^{-1}$]	Δ^2 [S^{-1}]	T_V [ps]	T_R [ps]	T_M [ns]	q
Gd-(3) monomer	13.9	$3x10^{19}$	27	200	100	2
Gd-(3) aggregates	20	$3.2x10^{19}$	27	300	100	2+5 2^{nd} sph.
Gd-AAZTA	7.1	$2.4x10^{19}$	31	70	90	2
Gd-(2)	8.6	$1.9x10^{19}$	41	173	120	1

Table 1. Principal relaxometric parameters for the Gd-(**3**)-containing systems and related complexes, determined by NMRD and 17O-R_{2p}-VT analysis.

Binding to HSA: In consideration of the possible use as an angiographic MRI system, the interaction with the human serum albumin (HSA) was investigated in detail for Gd-(**3**). The binding of Gd-(**3**) to HSA was conveniently assessed by measuring the water proton relaxation rates of solutions containing the paramagnetic complex and by increasing concentrations of the serum protein (PRE method).[22] With the estimation of the binding strength (nK_A, where n is the number of binding sites) these measurement also provide a direct assessment of the relaxivity of the macromolecular adduct (r_1^b). Analysis of the relaxometric data obtained at 0.47T from the titration of a 60 μM aqueous solution of the Gd^{III} complex with HSA at pH 7.4 and 298 K (Figure 5) allowed to determine the nK_A and r_1^b values reported in **Table 2**. The binding affinity with HSA increase significantly, nK_A value is one order of magnitude higher comparing with the Gd-(**2**) adduct and the relaxivity of the noncovalently bound complex (r_1^b) is 38.7 $mM^{-1}s^{-1}$, close to the value obtained in the literature for Gd-(**1**).[23]

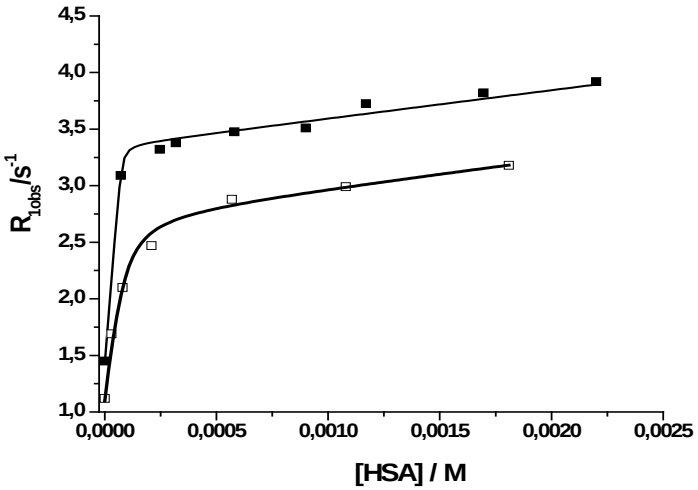

Figure 5: Plot of variation of observed longitudinal water proton relaxation rate of a 60 μM solution of Gd-(**3**) (■) and Gd-(**2**) (□) measured at 0.47 T and 25°C.

Contrast Agent	nK_A [10^4 M^{-1}]	r_1^b [mM^{-1} s^{-1}]
Gd-(3)	88.53±5.6	38.7±0.27
Gd-(2)	4.78±1.77	27.7±0.68

Table 2. Binding parameters for Gd-(**3**) and Gd-(**2**) systems, determined using the PRE method at 25°C in phosphate buffer solutions.

The NMRD profile of Gd-(**3**)-HSA adduct was recorded in the range of 0.01-70 MHz at 289K in phosphate buffer (**Figure 6**) to analyze the relaxometric parameters of the supramolecular adduct. The profile of the HSA adduct shows high relaxivity values at all fields, with a marked peak centered at 30 MHz, typical of slowly tumbling systems, and suggest that, upon binding to the protein, Gd-(**3**) maintains both the two inner sphere water molecules.

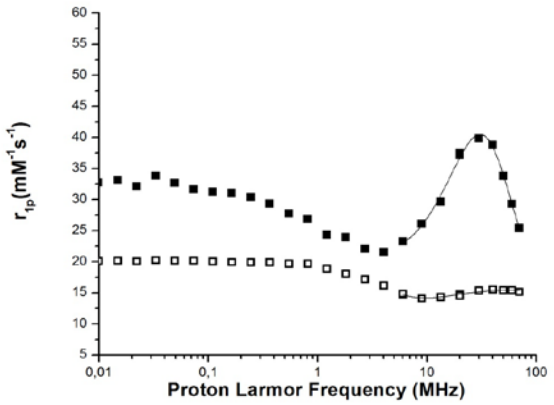

Figure 6:1/T_1 NMRD profile of 1 mM solution of Gd-(**3**) bound to HSA (■), Gd-(**2**) bound to HSA (□) and Gd-(**1**) bound to HSA (▼) measured at 25°C.

The data were fitted to the Lipari-Szabo model-free approach that takes into account the presence of an internal rotation, characterized by a correlation τ_{RL}, superimposed on a global motion described in term of the correlation time τ_{RG}.[24] The results are collected in **Table 3**and the fitting reveals a long global (whole adduct) rotational correlation time (τ_{RG}= 10 ns) and a short local rotational time (τ_{RL}=460 ps).

Contrast Agent	r_{1p} (20 MHz) [$mM^{-1}S^{-1}$]	Δ^2 [S^{-1}]	T_V [ps]	T_R [ps]		T_M [ns]	q
Gd-(3)	13.9	$3x10^{19}$	27	200		100	2
Gd-(3) + HSA	38.7	$1.55x10^{19}$	15.4	T_{RL}/[ps] 460	T_{RG}/[ps] 10000	440	2
Gd-(1) +HSA	40.2	$2.4x10^{19}$	44	650	10000	183	1

Table 3. Principal relaxometric parameters derived from the fitting of ^{1}H-NMRD and $^{17}OR_{2p}$ profiles of Gd-(**3**) with/without HSA and comparison with Gd-(**1**).

The order factor value S^2 obtained from the fitting was founded to be 0.6, corresponding to a significantly flexible movements of Gd-(**3**) at the binding site. Surprisingly, the possible reduction in the exchange of the inner-sphere water molecules of Gd-(**3**) upon interaction with HSA,[25] as already observed for the analysis of a similar Gd-AAZTA-bile acid conjugate,[26] was not found for Gd-(**3**). The hydration number q = 2 was maintained, although the relaxivity values of the complex bound to HSA is far away from the maximum values predicted by theory. The principal reason could be correlated to the reasonable degree of local flexibility of this Gd-complex to the binding site, explaining the shorter τ_{RL} .The presence of a different rotational dynamics of the complex during the interaction with the protein plays against the achievement of relaxivity value suitable for a systems with two inner sphere water molecules. To confirm the conservation of the

hydration number (q=2) of the complex following the interaction with HSA, the measurement of the ^{17}O-VT R_{2p} profile was performed. In order to ensure the complete formation of the HSA-Gd-(**3**) adduct, the profile was measured in a sample containing 3 mM Gd-(**3**) and 3 mM HSA. The analysis of the data reported in Figure 7, showed the high ^{17}O NMR R_{2p} values measured, along all the temperature range, for the HSA-bound complex compared to the free one. This observation confirms the possible conservation of two waters molecule in the inner-sphere even though the fitting of the ^{17}O NMR data requires the presence of two species. A possible reason could be due to the coexistence of two difference structural isomers of the Gd-complex in solution, as can be seen from the ^{17}O analysis. Despite the evidence of two isoforms of Gd-(**3**) in solution upon interaction with HSA, the hydration number *q*=2 was confirmed by the fitting the ^{17}O NMR data.

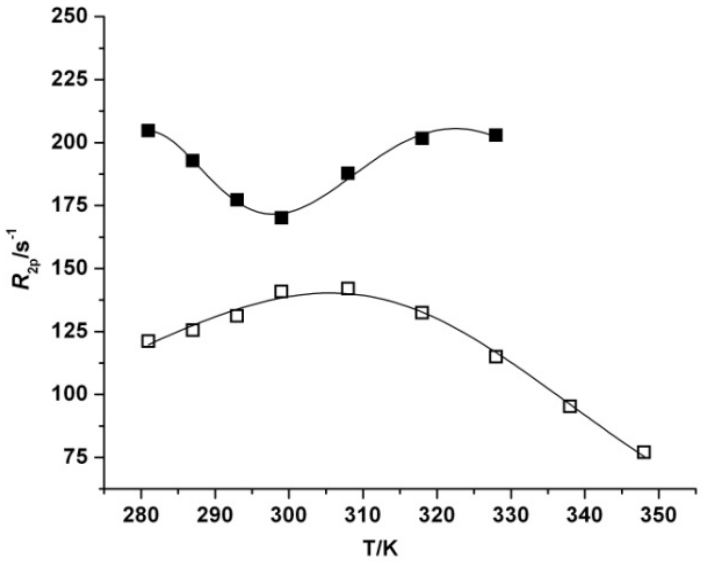

Figure 7: Temperature dependence of the transverse ^{17}O water relaxation rate (R_{2p}) of free (□) and HSA-bound (■) Gd-(**3**). ([Gd-(**3**)] = 3.0 mM, [HSA] = 3.0 mM, 14

T). The curve through the data for HSA-bound Gd-complex was calculated for a model considering the presence in solution of two isomers.

The long aliphatic chain likely allows the Gd-chelate to go away from potentially coordinating residues of the HSA protein, avoiding any interference with the exchange of the coordinated water molecule(s). The long aliphatic chain could be also responsible for the precise integration of the bile acid residue within the HSA binding site, defining the higher intensity in the binding affinity observed for this novel Gd-AAZTA-derivative.

HSA binding sites: HSA has multiple binding sites, differing in their polarity as well as in the binding affinities towards hydrophilic and hydrophobic molecules. To shed more light on the binding interaction of Gd-(**3**) with HSA, binding assays with specific molecules like warfarin (site I) and ibuprofen (site II) are needed, as exemplified by the work of Sudlow et al.[27] In a typical competition assay, a solution containing a Gd(III)-complex and HSA in a specified ratio undergoes a T_1 measurement (performed at 20 MHz and 298K) in the presence of increasing amounts of a molecule competing for a specific site. A decrease of the R_{1obs} is a direct indication of the competition between the chelate and the added substrate. However, drug binding site I is as very large binding domain, with three distinct subdomains, which can accommodate simultaneously small-to-medium size molecules. This means that when probing the drug binding site I with warfarin, there is the possibility that it can still accommodate the Gd-complex molecule, without displacement of warfarin. For this reason, iodipamide, a larger molecule, was chosen to probe the interaction of the Gd-complex with the binding site I. The results of these experiments are reported in Figure 8.

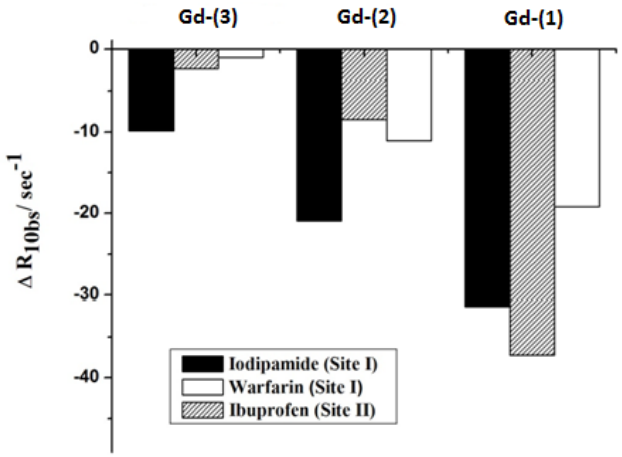

Figure 8: Variation of proton relaxation rates of aqueous solutions of 0.5 mM HSA and 0.05 mM of Gd-(**3**), Gd-(**2**) and Gd-(**1**) as a consequence of the competition for the binding to the protein upon addition of the substrate Iodipamide and Warfarin for the Site I and Ibuprofen for Site II ([Competitors]= 5 mM) .

In Figure 8 the results for the competition-binding assay between Gd-(**3**) and two classical HSA binding substrates is reported and compared with the competition of Gd-(**2**) and Gd-(**1**). Only in the case of Iodipamide (typical Sudlow's site I ligand) a slight decrease in the R_{10bs} is observed for Gd-(**3**), whereas no competition effect is obtained in the case of Ibuprofen (typical Sudlow's site II ligand). A completely different behavior was observed in the case of Gd-(**2**) and Gd-(**1**). The general behavior of Gd-(**2**) is comparable with Gd-(**3**), with preferential interaction in the site II in which we can found a smaller variation in the T_1 measures. The difference in the decrease of R_{10bs} between Gd-(**2**) and Gd-(**3**) could be allocated in the difference in the binding affinity to HSA. Concerning Gd-(**1**), the favourite binding site was found to be site II, although the competition with Iodipamide shows some evidences of displacement, not shown in the previous work from Caravan[11] when using the smaller molecule warfarin. It is likely that Gd-(**1**) binds primarily to site II followed by site I.

Comparison of NMRD profiles of Gd-(3), Gd-(2) and Gd-(1) in human and mouse serum

As previously noted by Caravan et al,[28] the binding and relaxometric properties of Gd-based "blood pool" agents may significantly change upon going from human to mouse serum albumin. Moreover human and mouse may differ in their composition and affect substantially the behavior of the paramagnetic complex in the two media. As these agents are intended for use in mouse models, a direct comparison of the NMRD profiles of the three complexes in human and mouse serum is required. (Fig 9 and Table 4)

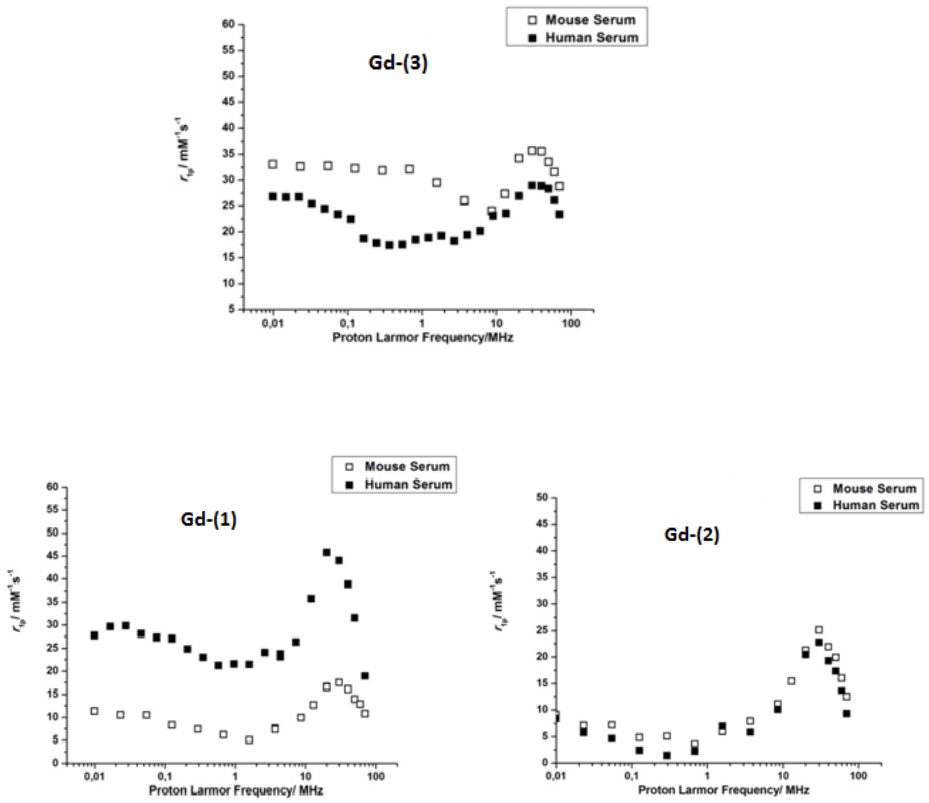

Figure 9: NMRD profile of Gd-(**3**), Gd-(**2**) and Gd-(**1**) in mouse (open square) and human serum (closed square) at 37°C.

Contrast Agent	Mouse Serum	Human Serum
	$R_{1p}/mM^{-1}s^{-1}$	
Gd-(3)	35.5	28.2
Gd-(2)	22	20
Gd-(1)	16.0	38.9

Table 4: Relaxivities of Gd-(**3**), Gd-(**2**) and Gd-(**1**) measured at 1T and 37°C in mouse and human serum.

The important evidence from the data reported could be summarized in the unrivaled behavior of Gd-(**3**) in both mouse and human serum, not observed with Gd-(**1**) or Gd-(**2**). Gd-(**1**) shows a drastic difference in the bound relaxivities, as already reported by Caravan et al.,[28] while for Gd-(**2**) the values are very similar but significantly lower than those of Gd-(**3**). The relaxivity of the non-covalently bound complex with Gd-(**3**) presents high values with respect to the other two complexes and allows this Gd-AAZTA derivative to represent the optimal Gd-based blood pool agent for preclinical studies in both mouse models and in human.

Pharmacokinetic Studies: The average plasma Gd concentrations calculated as percentage of the initial dose (C_0) after a single bolus injection through the tail vein at a dose of 0.05 mmolGd/kg, reveals a prolonged blood residence of Gd-(**3**) as compared to Gd-(**2**) and Gd-(**1**), over the entire period of the experiment (Figure 10). The average plasma Gd concentration of Gd-(**3**) at 5 min post-injection was 37.3% of the initial dose, while that of Gd-(**2**) and Gd-(**1**) was 29.9% and 24.2%, respectively. The blood concentration gradually decreased for all agents and at 6 h post-injection the plasma Gd concentration was less than 1%. The prolonged blood circulation time could possibly be explained by the higher binding affinity constant to HSA that in turn results in a reduced amount of the free from that is excreted by kidneys. In addition, Gd-(**3**) shows a reduced liver uptake, in comparison to Gd-(**2**),

and a reduced renal filtration, as compared to Gd-(**1**), resulting in higher blood concentration values at all the investigated time points. The Gd plasma concentration profiles of the agents were analyzed with a two-compartment pharmacokinetic model. The mean values of half-life associated with the elimination phase, $t_{1/2\beta}$, was longer for Gd-(**3**) (24.6 min) than for Gd-(**1**) (19.9 min), and for Gd-(**2**) (18.2 min). The elimination half-lives of Gd-(**2**) and Gd-(**1**) were comparable to previous values obtained in rats.[11,29,30] Considering that elimination half-lives in humans are six to nine fold longer than in mice, these results indicated that the order of magnitude of difference in the affinity constant of Gd-(**3**)-HSA may allow really steady-state MRI angiographic acquisitions.

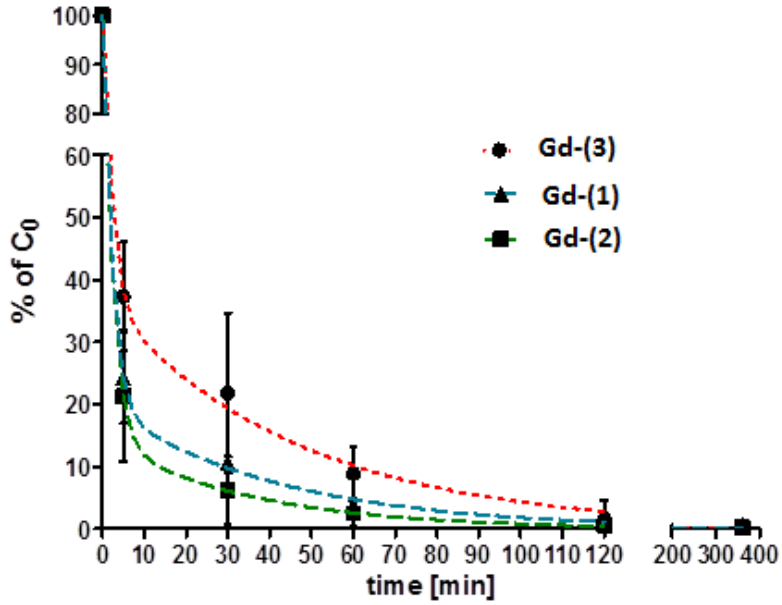

Figure 10: Plasma level decay as % of the initial dose (C_0) after single intravenous injection of Gd-(**3**) (circles), Gd-(**1**) (triangles) and Gd-(**2**) (squares) at a dose of 0.05 mmolGd/kg. Variability associated to each time/concentration point, expressed as standard deviations, ranged between 3 and 15%.

Magnetic Resonance Angiography: Figure 11 shows the three-dimensional maximum intensity projection (MIP) images of mice contrast enhanced by Gd-(**3**),

Gd-(**2**) and Gd-(**1**) at 2, 5, 15, 30 and 60 min post-injection of the contrast agents at a dose of 0.05 mmolGd/kg. The three investigated CAs showed different contrast enhancement properties, related to both duration and tissue localization. The Gd-(**3**) resulted in stronger and more prolonged contrast enhancement than Gd-(**2**) and Gd-(**1**) in the heart and blood vessels. The visualization of vessels was enhanced up to 30 min post-injection. Gd-(**1**) resulted in significant blood pool enhancement at 2 min post-injection, with the signal that gradually fading away due to the clearance of the agent from the blood, resulting in a strong enhancement inside the bladder gradually increasing over time. Gd-(**2**) exhibited longer vascular enhancement duration than Gd-(**1**), but lower then Gd-(**3**). Gd-(**2**) also resulted in significant enhancement in the liver and gallbladder.

The contrast enhancement pattern of the agents in the blood pool was consistent to the plasma pharmacokinetic results.

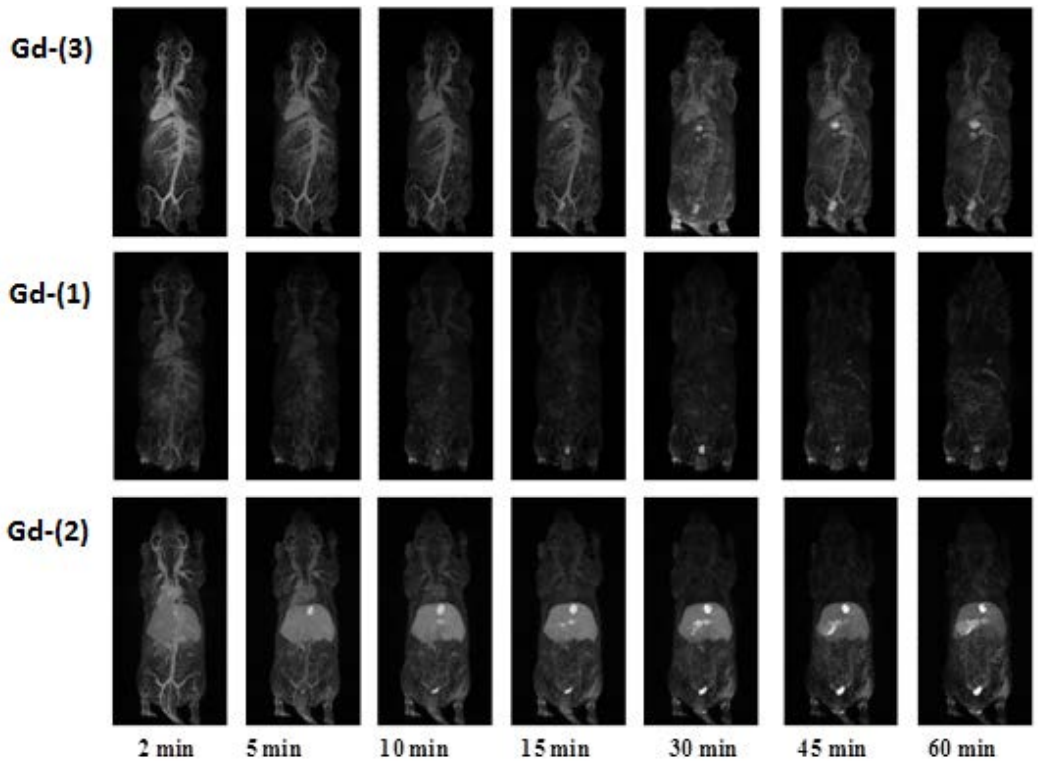

Figure 11: Whole body coronal maximum intensity projection (MIP) of the 3D FLASH images obtained from the mice after intravenous injection of Gd-(**3**) (top), Gd-(**1**) (middle) and Gd-(**2**) (bottom) at a dose of 0.05 mmolGd/kg. Post-contrast images at 2, 5, 10, 15, 30, 45 and 60 min are shown here after the subtraction of the corresponding pre-contrast images.

Figure 12 shows the normalized signal intensities in the heart, liver, urinary bladder and gallbladder relative to the signal intensity in muscle. The heart contrast enhancement was significant higher for Gd-(**3**) and Gd-(**2**) up to 30 min and 10 min, respectively.

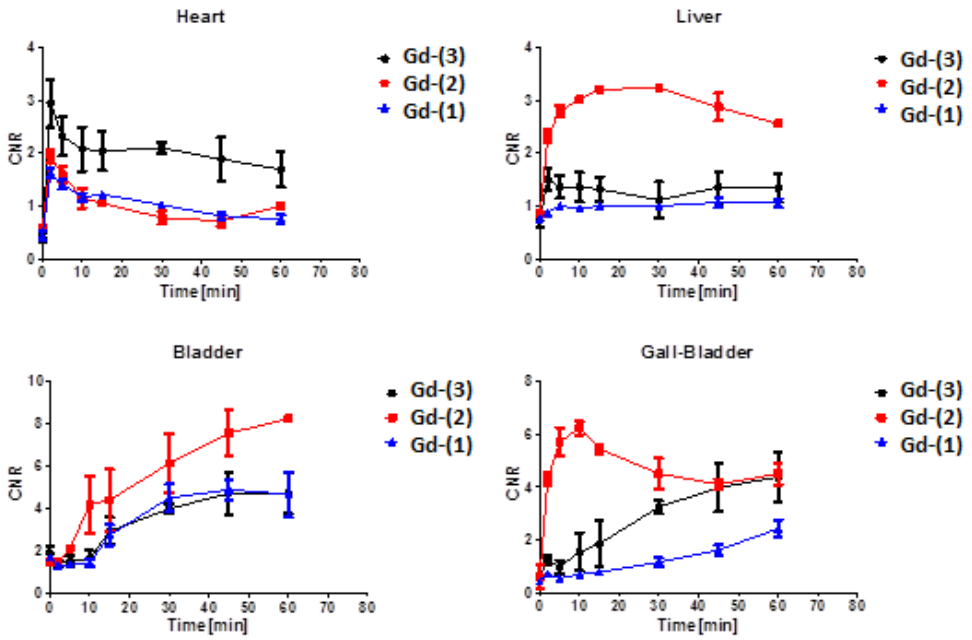

Figure 12: Normalized signal intensity in the heart (A), liver (B), gallbladder (C), urinary bladder (D) (SI of heart, liver, gallbladder, urinary bladder / SI of muscle) before and at various time points post-injection of Gd-(**3**) (circles), Gd-(**1**) (triangles) and Gd-(**2**) (squares) at a dose of 0.05 mmolGd/kg. Values are shown as mean ±SD (n=3) for each contrast agent.

Both Gd-(**3**) and Gd-(**2**) had a prolonged contrast enhancement in the blood pool as compared to the Gd-(**1**) CA. However, Gd-(**3**) resulted in clearer visualization of small blood vessels, providing effective contrast enhancement for more than 15 min. The effective enhancement window of Gd-(**3**) in humans may be longer than in mice because the blood circulation in human is much slower than in mice.

Vascular imaging requires both sufficient high relaxivity and long blood half life to obtain high contrast enhanced steady state images. To further investigates the marked vascular contrast enhancing properties between Gd-(**3**) and Gd-(**2**), despite their similar blood elimination kinetics, NMRD relaxivity studies with purified serum albumin from mouse and from human species were performed. Previous studies from Caravan et al. already showed species dependence on albumin binding.[31] This dependence may bias the conclusions when comparing the results obtained in vitro at 25°C when using human serum albumin for clinical diagnostic applications with the results obtained *in vivo* at 37°C from their preclinical use in rodents. Therefore a blood pool CA designed and optimized for humans, may show sub-optimal relaxivity properties when used in other species. This is the situation for Gd-(**1**), whose outstanding relaxivity of ca. 39 $mM^{-1}s^{-1}$ in human serum (at 40 MHz and 37°C) dramatically drops to 16 $mM^{-1}s^{-1}$ in mouse serum (Figure 9 and Table 4). Gd-(**2**) NMRD profiles were almost superimposable for both the two species, with r_{1p}^{bound} of 19 $mM^{-1}s^{-1}$ and 22$mM^{-1}s^{-1}$ for human and mouse serum, respectively. Therefore for this CA the interaction with the albumin from different species did not affect its relaxivity. On the other hand, the already high relaxivity shown by Gd-(**3**) in human serum (31 $mM^{-1}s^{-1}$) was even higher when added to the mouse serum (40 $mM^{-1}s^{-1}$). This marked species dependence of the investigated blood pool CAs explains the differences in contrast enhancement capabilities in the corresponding angiographic images. In fact, the longest elimination half-life, as well as the highest relaxivity showed by Gd-(**3**) in mouse serum resulted in the brightest and prolonged MIP angiographic images. Gd-(**1**), despite a slight shorter

elimination half-life in comparison to Madec, it is not suited for mice angiographic images due to the low efficiency in mice serum. Gd-(**2**), despite having high relaxivity in mouse serum, resulted in angiographic images that are not optimal, due to the relative fast elimination kinetic and to the high liver uptake.

Contrast Enhanced-MRI of tumor-bearing mice: All the CAs demonstrated to be able to induce a contrast enhancement inside tumors, exploiting the enhanced permeability retention effect, at the investigated doses of 0.05 mmolGd/kg. Figure 13 shows the dynamic signal intensity enhancement in mice bearing B16 human melanoma xenografts, calculated inside the tumor tissue. Significant contrast enhancement was observed, already at 10 min post-inejction, for Gd-(**3**), Gd-(**2**) and Gd-(**1**), of 79.8%, 55.0% and 58.0%, respectively. The contrast enhancement slowly reduced thereafter for Gd-(**2**), being 44.5% at 30 min and 41.7% at 45 min, while for Gd-(**3**) and Gd-(**1**) remained constant along time (91.7% and 98.7% for Gd-(**3**) and 67.5% and 68.2% for Gd-(**1**), at 30 and 50 min, respectively). The tumor contrast enhancement of Gd-(**3**) was higher than that of Gd-(**2**) and Gd-(**1**) during all the dynamic acquisition series. The slow reduction of the contrast enhancement shown by Gd-(**2**) may be likely due to the accumulation of the contrast agent in the liver and gallbladder, thus resulting in a lower blood pool concentration along time, as reported by the pharmacokinetic profile, which turns in a reduced extravasation to the tumor region. On the contrary, the prolonged vascular retention for Gd-(**3**), allows a continue accumulation of the macromolecular adduct inside the tumor, thus resulting in a sustained and elevated contrast enhancement. In addition, we investigated the use of Gd-(**3**) for DCE-MRI approaches by halving the dose. Interestingly, the obtained contrast enhancement in tumor region was comparable with the enhancement reached by the Gd-(**2**) and Gd-(**1**) at a double dosage (Fig. 13).

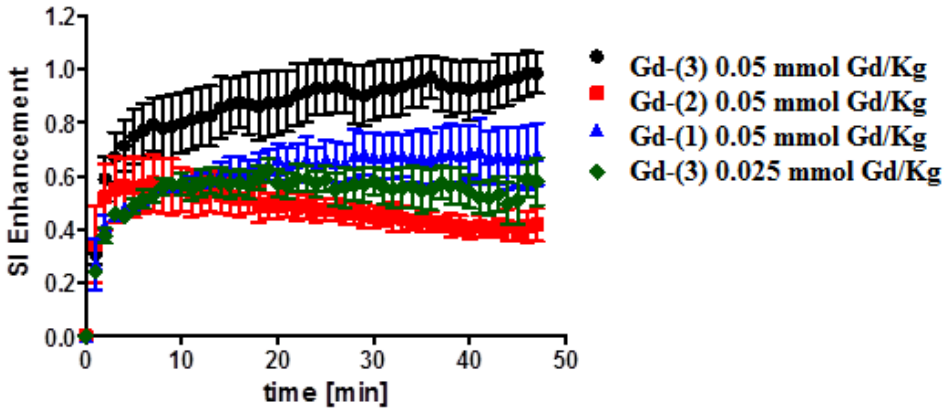

Figure 13: Signal intensity enhancement in tumor of mice before and at various time points post-injection of Gd-(**3**) (circles), Gd-(**1**) (triangles) and Gd-(**2**) (squares) at a dose of 0.05 mmolGd/kg and of Gd-(**3**) (diamond) at a dose of 0.025 mmolGd/kg. Values are shown as mean ±SD (n=3) for each contrast agent.

Conclusion

A novel Gd(III)-based MRI contrast agent (Gd(CN-AAZTA-MADEC) optimized for preclinical DCE imaging application on mice, was designed and prepared. The contrast agent combines the excellent coordination proprieties of the AAZTA chelating at substructure with the HAS-binding ability of a cholic acid residue.

The diagnostic potential of this novel CA was determined by comparison with two different CAs previously employed in DCE-MRI procedures.

Gd-(**3**) shows superior relaxometric proprierties due to the higher hydration of Gd in the AAZTA coordinating environment. Relaxivities values became even higher in the presence of serum albumin, especially with mouse serum albumin where the relaxivity is significantly higher than HSA. The strong association with MSA/HSA leads to improved pharmacokinetic profiles with relevant advantages for DCE-based imaging procedures.

On the basis of the comparison among similar Gd-complexes for DCE-MRI, the newly developed Gd-(**3**) was shown to be the best contrast agent for preclinical studies, in view of its optimal performances in mouse serum.

References

[1] N. Hayashi, Y. Watanabe, T. Masumoto, H. Mori, S. Aoki, K. Ohtomo, O. Okitsu, T. Takahashi, *Magn. Res. Med. Sciences*, **2004**, *3*, 27-38.

[2] A. Gossmann, Y. Okuhata, D. M. Shames, T. H. Helbich, T. P. Roberts, M. F. Wendland, S. Huber, R. C. Brasch, *Radiology*. **1999**, *213*, 265-272.

[3] a) P. Marzola, A. Degrassi, L. Calderan, P. Farace, E. Nicolato, C. Crescimanno,M. Sandri, A. Giusti, E. Pesenti, A. Terron, A. Sbarbati, F. Osculati, *Clin Cancer Res* **2005**, *11*, 5827-5832; b) J. P. O'Connor, A. Jackson, G. J. Parker, G. C. Jayson, *Br. J. Cancer.* **2007**, *96*, 189-195.

[4] P. Caravan, J. J. Ellison, T. J. McMurry, R. B. Lauffer, *Chem Rev* **1999**, *99*, 2293-2352.

[5] T. P. Roberts, K. Turetschek, A. Preda, V. Novikov, M. Moeglich, D. M. Shames, R. C. Brasch, H. J. Weinmann, *Acad Radiol* **2002**, *9 Suppl 2*, S511-513; K. Turetschek, A. Preda, V. Novikov, R. C. Brasch, H. J. Weinmann, P. Wunderbaldinger, T. P. Roberts, *J. Magn. Reson. Imaging* **2004**, *20*, 138-144.

[6] F. Kiessling, M. Jugold, E. C. Woenne, G. Brix, *Eur Radiol* **2007**, *17*, 2136-2148.

[7] R. J. Gillies, N. Raghunand, G. S. Karczmar, Z. M. Bhujwalla, *J. Magn. Reson. Imaging* **2002**, *16*, 430-450.

[8] S. Geninatti-Crich, I. Szabo, D. Alberti, D. Longo, S. Aime, *Contrast Media Mol Imaging* **2011**, *6*, 421-425.

[9] P. L. Anelli, M. Brocchetta, L. Lattuada, G. Manfredi, P. Morosini, M. Murru, D. Palano, M. Sipioni, M. Visigalli, *Org. Process Res. Dev* **2009**, *13*, 739-746.

[10] A. La Noce, S. Stoelben, K.Scheffler, J. Hennig, H. Maier Lenz, R. La Ferla, V. Lorusso, F. Maggioni, F. Cavagna, *Acad. Radiol.***2002**, *9*, S404–406.

[11] D. J. Parmelee, R. C. Walovitch, H. S. Ouellet, R. B. Lauffer, *Invest. Radiol.* **1997**, *32*, 741-747.

[12] S. Aime, L. Calabi, C. Cavallotti, E. Gianolio, G. B. Giovenzana, P. Losi, A. Maiocchi, G. Palmisano, M. Sisti, *Inorg. Chem* .**2004**, *43*, 7588-7590.

[13] Z. Baranyai, F. Uggeri, G. B. Giovenzana, A. Bényei, E. Brücher, S. Aime, *Chem. Eur. J.***2009**, *15*, 1696-1705.

[14] E.Gianolio, G. B. Giovenzana, D. Longo, I. Longo, I. Menegotto, *Chem. Eur. J.* **2007**, *13*, 5785-5797.

[15] K. C. Briley-Saebo, S. Geninatti, A. Barazza, D. Cormode, W. J. M. Mulder, W. Chen, G. B. Giovenzana, S. Aime, Z.A. Fayad, *J. Phys. Chem.* **2009**, *113*, 6283-6289.

[16] S. GeninattiCrich, S. Lanzardo, D. Alberti, S. Belfiore, A. Ciampa, G. B. Giovenzana, C. Lovazzano, R. Pagliarin, S. Aime, *Neoplasia* **2007**, *9*, 1046-1056.

[17] P. Minazzi, L. Lattuada, I. Menegotto, G. B. Giovenzana, *Org. Biomol. Chem*. submitted for publication.

[18] P. L. Anelli, L. Lattuada, F. Uggeri *Synth. Commun.* **1998**, *28*, 109-117.

[19] M. Woods, M. Botta, S. Avedano, J. Wang, A. D. Sherry, *Dalton Trans* **2005**, 3829-3837.

[20] a) N. Blombergen *J. Chem. Phys.* **1957** *27*, 572-573; b) I. Solomon. *Phys. Rev.* **1955**, *99*, 559-565.

[21] I. J. Freed. *J. Chem. Phys.* **1978**, *68*, 4043-4037

[22] a) M. Fasano, S. Curry, E. Terreno, M. Galliano, G. Fanali, P. Narciso, S. Notari, P. Ascenzi, *IUBMB Life* **2005**, *57*, 787-796; b) S. Aime, M. Botta, M. Fasano, S. G. Crich, E. Terreno, *Jo. B. Inorg. Chem.* **1996**, *1*, 312-319.

[23] S. Aime, M. Chiaussa, G. Digilio, E. Gianolio, E. Terreno, *J. Biol. Inorg. Chem.* **1999**, *4*, 766-774.

[24] G.Lipari and A. Szabo, *J. Am. Chem. Soc*. **1982**, *104*, 4546-4559

[25] S. Aime, E. Gianolio, D. Longo, R. Pagliarin, C. Lovazzano, M. Sisti, *Chem. BioChem* **2005**, *6*, 818-820.

[26] E. Gianolio, C. Cabella, S. Colombo Serra, G. Valbusa, F. Arena, A. Maiocchi, L. Miragoli, F. Tedoldi, F. Uggeri, M. Visigalli, P. Bardini, S. Aime, *J. Biol. Inorg. Chem.*, **2014** in press, doi: 10.1007/s00775-014-1111z.

[27] G. Sudlow, D.J. Birkett, D.N. Wade, *Mol. Pharmacol.*, **1975**, *11*, 824-832.

[28] H. B. Eldredge, M. Spiller, J. M. Chasse, M. T. Greenwood, P. Caravan, *Inves.t Radiol.* **2006**, *41*, 229-243.

[29] C. de Haen, P. L. Anelli, V. Lorusso, A. Morisetti, F. Maggioni, J. Zheng, F. Uggeri, F. M. Cavagna, *Invest. Radiol.* **2006**, *41*, 279-291.

[30] F. M. Cavagna, V. Lorusso, P. L. Anelli, F. Maggioni, C. de Haen, *Acad. Radiol.* **2002**, *9 Suppl 2*, S491-494.

[31] S. G. Zech, H. B. Eldredge, M. P. Lowe, P. Caravan, *Inorg. Chem.* **2007**, *46*, 3576-3584.

5. Conclusions

The research activity of the PhD has been focused on the development of novel Bifunctional Chelating Agents (BFCAs) and their applications in diagnostic imaging techniques.

In the PhD period, different activities were undertaken…

The first period of the PhD activity was dedicated to the design and the preparation of novel BFCAs. Chelating agents for lanthanide(III) ions were selected, because most diagnostic imaging techniques rely on the use of lanthanide(III) metal complexes as contrast agents or probes. Three well established ligand platforms were then chosen to prepare the corresponding BFCAs (*i.e.*: AAZTA, HP-DO3A and DOTAMA), and a synthetic strategy was devised in order to introduce a reactive functional group in a remote position of the chelating agent molecular backbone. To this purpose, an original chemoenzymatic approach was developed in order to manage the large number of functional groups associated with these polyaminopolycarboxyxlic molecules. The selectivity of hydrolytic enzymes was employed in the key step of the synthesis of the three BFCAs, leading to an efficient protocol used for their multi-gram scale preparation.

The second part of the PhD activity took advantage of the availability of the BFCAs developed in the first period to prepare some conjugate chelating agents, whose metal complexes could be used in targeted imaging applications. In detail, the reactive functional group of the AAZTA-derived BFCA developed in the first year was employed to form a covalent link with a task-specific molecule (a cholic acid derivative). The resulting conjugate was used to prepare a Gd(III)-complex evaluated as potential MRI contrast agent (CA) for DCE-MRI applications.

The relaxometric studies performed on this novel CA showed interesting results: its contrast efficiency is higher than that owned by similar CAs, either in water or in serum. Interestingly, the paramagnetic complex shows a relevant enhancement of its performances in mouse serum compared with human serum, due to a strong association with serum albumin. The pharmacokinetic of this novel CA is improved with respect to the compared CAs, and allows to obtain high quality images of blood vessels and to extract accurate structural and functional parameters. The species-specificity, combined with the fact that the best contrast efficiency is shown at low magnetic fields (0.5-1.5T) make this compound the best candidate for preclinical studies, where imaging of mice are routinely run on small and dedicated low-field MRI scanners.

List of Publications

- Caldarelli, P. Minazzi, P. Canonico, A. Genazzani, G. Giovenzana: ***N*-Arylbenzamides: extremely simple scaffolds for the development of novel estrogen receptor agonists**. *Journal of Enzyme Inhibition and Medicinal Chemistry*, **2013**, *28* (1), 148-152 DOI: 10.3109/14756366.2011.642374.

- P. Minazzi, G. B. Giovenzana, C. Cavallotti, I. Menegotto: "**Chemoenzymatic Approach to Bifunctional AAZTA-like Contrast Agents**", 8th International Conference on f-Elements (ICFE-2012), Udine, Italy, August 26-31, **2012** (Partecipazione e autore principale di Comunicazione Poster MED 11P).

- S. Geninatti Crich, D. Alberti, D. Burghelea, P. Minazzi, C. Cavallotti, G. Giovenzana, S. Aime: "**Calix[4]resorcinarenes based "theranostic" MRI agents**", World Molecular Imaging Congress 2012, Dublin, Ireland, Sept 5-8, **2012** (Coautore di Comunicazione Poster P197).

- P. Minazzi, L. Lattuada, I. Menegotto, G. Giovenzana. **Enzymatic approach to bifunctional chelating agents.** *Organic & Biomolecular Chemistry*, submission in progress.

- F. Arena, D. L. Longo, L. Consolino, E. Gianolio, P. Minazzi, G. B. Giovenzana and S. Aime. **Gd(CN-AAZTA-MADEC), an excellent agent for DCE-MRI studies on mice on 1T scanners** *Molecular Imaging and Biology*, submission in progress.